SILVER CLUSTERS ON SnO_2 THIN FILM SURFACES AND THEIR APPLICATION TO GAS SENSORS

by

Jianping Zhang

B.Sc. Zhongshan University, 1982

M. Sc. Simon Fraser University, 1989

THESIS SUBMITTED IN PARTIAL FULFILLMENT OF
THE REQUIREMENTS FOR THE DEGREE OF
DOCTOR OF PHILOSOPHY

in the Department
of
Physics

SIMON FRASER UNIVERSITY

February, 1995

APPROVAL

Name: Jianping Zhang

Degree: Doctor of Philosophy

Title of Thesis: Silver Clusters on SnO_2 Thin Film Surfaces and Their Application to Gas Sensors

Examining Committee: Dr. J. R. Dahn, Chairperson

Dr. K. Colbow
Senior Supervisor

Dr. R. F. Frindt

Dr. S. R. Morrison

Dr. M. Plischke
Internal Examiner

Dr. T. Tiedje
External Examiner
Dept. of Physics/Electrical Eng., UBC

Date Approved: March 1, 1995

PARTIAL COPYRIGHT LICENSE

I hereby grant to Simon Fraser University the right to lend my thesis, project or extended essay (the title of which is shown below) to users of the Simon Fraser University Library, and to make partial or single copies only for such users or in response to a request from the library of any other university, or other educational institution, on its own behalf or for one of its users. I further agree that permission for multiple copying of this work for scholarly purposes may be granted by me or the Dean of Graduate Studies. It is understood that copying or publication of this work for financial gain shall not be allowed without my written permission.

Title of Thesis/Project/Extended Essay

Silver Clusters on SnO_2 Thin Film Surfaces and Their Application to Gas Sensors.

Author: _____
(signature)

_____
(name)

3 March 1995
(date)

ABSTRACT

We observed for the first time fractal patterns of silver growth on tin oxide (SnO_2) films under appropriate operating conditions. The pattern growth processes and structures were studied by SEM, AES and XRD. It was found that the size of patterns varied from ten to hundreds of micrometers with a branch diameter of about 2 micrometers. The patterns were formed by Ag and AgCl with a thin layer of silver oxide on the surface.

The patterns obtained from our experimental method have both fractal and dense packed structures. The fractal dimension of the clusters was determined to be 1.69 ± 0.03, in excellent agreement with the theoretical value of 1.70 ± 0.02 predicted from the diffusion limited aggregation model (DLA). We also confirmed that the active zone of the cluster can be described by a Gaussian probability distribution function that is characterized by two parameters r_N and σ_N with two exponents, which were found to be $\upsilon = 0.607 \pm 0.013$ and $\upsilon' = 0.512 \pm 0.026$ for our clusters, in good agreement with theoretical values calculated from Monte Carlo simulation.

It was suggested that the pattern growth process in our experiment is basically an aggregation process which can be described theoretically by the DLA model where random walk trajectories are assumed. The pattern appearance and disappearance are believed to be associated with the decomposition of silver oxide and the oxidation of silver at around the decomposition temperature of 300 ^{0}C.

Another interesting subject (part II) in the thesis was to investigate the silver clusters acting as catalytic activators in SnO_2 gas sensors. Surface silver additives on SnO_2 thin film gas sensors effectively improved the sensor performance to H_2. The sensitivity was increased by at least a factor of 10 and the sensor recovery time decreased after the surface silver addition onto the SnO_2 surface. The sensitivity was found to be dependent on the operating temperature of the sensors and the amount of Ag additives that influences the cluster details. The experimental results showed that the best performance of sensors could be achieved by evaporating a Ag layer of 40 to 60 Å, and operating at temperatures around 300 ^{0}C. The effect of silver additives onto SnO_2 thin film gas sensors was studied and models for the promotional role of these additives are presented in the final chapter of the thesis.

Dedicated to my parents and my wife
for their continual support and encouragement

Acknowledgments

I wish to express my sincere appreciation to my senior supervisor, Dr. K. Colbow, for his encouragement and guidance through this research work, and for his patient reading and critical correcting of this manuscript. I would like to thank Dr. R. F. Frindt and Dr. S. R. Morrison for their time and valuable advice in the supervisors committee.

It is my pleasure to thank many people who have given various important assistances and advice during the course of this research work. These special thanks go to Dr. B. Heinrich, Dr. A. E. Curzon and Mr. K. Myrtle for their kind help in SEM and AES measurements, Dr. M. Plischke and Dr. Z. Rácz for their valuable advice and suggestions on fractal structures, Dr. J. R. Dahn for his important direction on the XRD data, Dr. B. K. Miremadi for his help and discussion in the testing of gas sensors and Dr. D. Liu for his assistance in some computer programs.

Finally, the Graduate Fellowship from SFU, the TA'ships from the Physics Department of SFU and support from the Linville-Wright Institute in Sensory Science are also very much appreciated.

TABLE OF CONTENTS

List of Tables

List of Figures

Figures **page**

Preface

Structure of Thesis

We observed fractal patterns of silver on SnO_2 film surfaces and found that silver clusters on the SnO_2 surface have useful application to gas sensors. The aim of this thesis is to study the structures and properties of these fractal patterns and to investigate the promotional role of silver additives to SnO_2 thin film gas sensors. In order to clearly identify these two different subjects, the thesis is divided into two parts.

Part I: Fractal Pattern Formation on SnO_2 films

In the first chapter of this part an introduction to fractal phenomena observed in various experiments and the theoretical studies of their structures and properties is presented. The following chapter describes the preparation of SnO_2 films, the experimental arrangement for pattern growth and the measurement techniques. Chapter 3 presents experimental observations on fractal patterns by microscopy, SEM, AES and XRD. The explanation of pattern formation is also included in this chapter. Chapter 4 is concerned with fractal dimension and the scaling of the active zone. Summary to part I is presented in chapter 5.

Part II: Ag-SnO_2 Thin Film Gas Sensors

In this part the effect of surface silver additives to SnO_2 thin film gas sensors was investigated. Chapter 6 presents a review of the necessary background to gas sensors. Chapter 7 describes the preparation of gas sensor elements and the experimental arrangement for conductance measurements. The experimental results on sensor performance are presented and discussed in the final chapter.

Part I

Silver Pattern Formation on SnO_2 Films

Chapter 1

Introduction to Fractals

Our interest in research on fractal structures arises from the observation of the formation of silver fractal patterns on tin oxide film surfaces by applying silver contacts on the film for conductivity measurements.

In the past decade, fractal pattern formations and their structures have been observed and studied both in the experimental and theoretical aspects. Examples for pattern growth processes include viscous fluids (Nittmann *et al* 1984, Daccord *et al* 1986a), chemical electrodeposition (Matsushita *et al* 1984, Sawada *et al* 1986, Argoul *et al* 1988, Fleury 1991), electrical breakdown (Niemeyer *et al* 1984) and dendritic solidification (Langer 1980, Radnoczi *et al* 1987). Several models, such as the Eden model (Eden 1961), diffusion limited aggregation (DLA) (Witten and Sander 1981,1983) and cluster-cluster aggregation (Meakin 1983a, Kolb *et al* 1983), have been suggested to explain and analyze these physical and chemical phenomena. Computer simulations, studies of the fractal dimension, and the geometry of clusters have been reported (Witten and Sander 1983, Vicsek 1989, Mandelbrot and Evertsz 1990, etc.). This chapter will give an introduction to the fractal phenomena observed in various experiments and the theoretical studies of their structures and properties.

1.1 Fractal phenomena

Fractal phenomena are exhibited in many fields of science and technology. Viscous fingering in the two-dimensional Hele-Shaw cell is a good example (Daccord *et al* 1986b). It takes place when a less viscous fluid is injected into a more viscous one under circumstance, leading to a fingered interface as shown in Fig. 1.1(a) (Daccord *et al* 1986b). Another much studied phenomenon is electrochemical metallic deposition (Matsushita *et al* 1985). In this typical experiment two electrodes, one may be zinc as anode and the other carbon as cathode, are immersed into an ionic solution and one observes a fractal structure made of metal atoms deposited on the cathode. Figure 1.1(b) shows a representative picture of zinc metal deposited on the cathode (Argoul *et al* 1988). Other related experiments are dielectric breakdown and solidification. Fractal dielectric breakdown occurs whenever the electric field is strong enough to generate a conducting phase within an insulator. Figure 1.1(c) shows a propagating discharge pattern obtained when a voltage pulse (30kV X 1ms) was applied at a starter kept in compressed SF_6 gas of pressure 0.3 MPa (Niemeyer *et al* 1984). Lightning in nature is the best known version of this phenomenon. The solidification as shown in Fig. 1.1(d) is a crystalline phase growing process in a pure undercooled liquid or in an isothermal liquid mixture leading to a complex geometrical pattern (Radnoczi *et al* 1987).

DLA-like patterns have also been observed in a variety of thin film systems, such as sputter-deposited thin films of $NbGe_2$ (Elam *et al* 1985), annealed amorphous $GeSe_2$ films (Radnoczi *et al* 1987) , ion irradiated Ni - Zr films

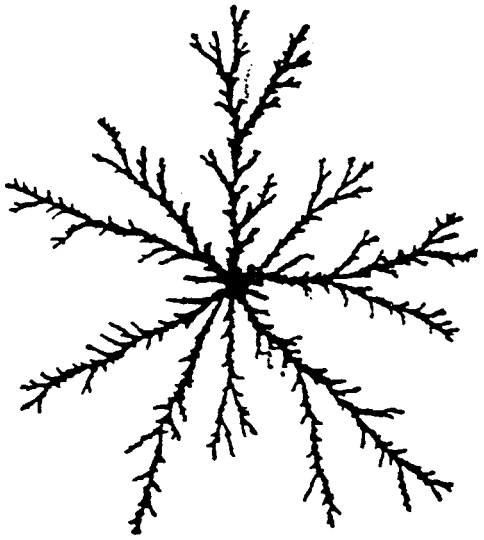

(a)

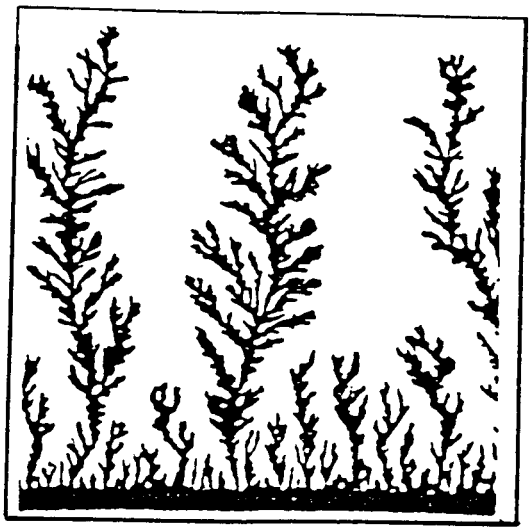

(b)

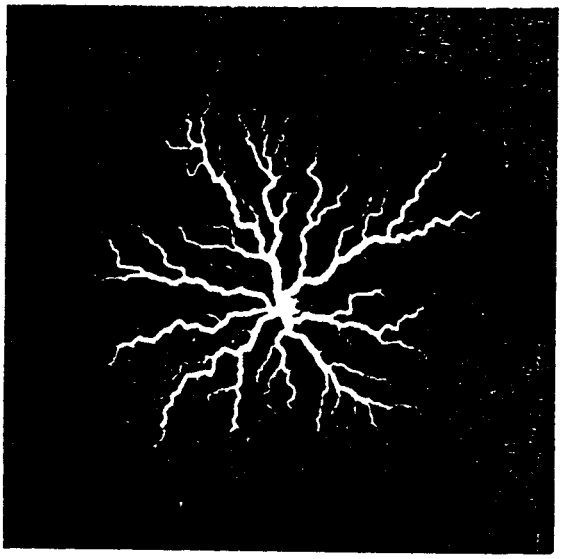

(c)

(d)

Figure 1.1 Examples of fractal structures observed in various experiments (a) viscous fingering, (b) electrodeposition of zinc, (c) dielectric breakdown and (d) crystallization

(Ding and Liu 1989a) and annealed superconducting $BaPb_{0.7}Bi_{0.3}O_3$ film in atmospheres containing lead oxide (Hidala *et al* 1983).

1.2 Cluster growth models

1.2.1 Eden model

A simple model was proposed by Eden in 1961 to explain the evolution of tumors. This model has since been applied to many other physical situations and even if it does not lead to a fractal structure, it is now considered as a fundamental basic model for aggregation.

In this model, the aggregation mechanism follows an iterative rule in which, starting from a seed particle at the origin, a new particle is added on a non-occupied site neighbor to an occupied site of the aggregate, by choosing the site at random among all the possibilities. Thus any empty neighboring site of the aggregate has the same chance to accept the new particle. Figure 1.2 (a) shows an Eden cluster of 8000 particles built on a square lattice (Jullien and Botet 1987).

1.2.2 Diffusion limited aggregation model

The diffusion limited aggregation (DLA) model was introduced by Witten and Sander in 1981. It is thus also called the Witten-Sander model. This model is able to build a fractal aggregation and is widely used to explain and

analyze various physical and chemical phenomena.

The original model in two dimensions will be described below. One chooses a seed particle at the origin of the lattice; then, one considers a large circle around the origin and chooses a point at random on this circle. A particle is released from this point and starts to follow a random walk on the lattice. The new position is chosen at random among the four possibilities assuming a square lattice. This random walk simulates the diffusive motion of a particle (Witten and Sander 1983). If during its random walk the particle reaches a site nearest neighbor to the seed site, it stops and stays stuck to the seed. By repeating the same procedure, a cluster is formed. Figure 1.2(b) shows a typical example of a two dimensional Witten-Sander aggregate, with a modest (N=1024) number of particles. One can see that the recently arrived particles preferentially stick on the tips. This screening effect qualitatively explains why Witten-Sander aggregates are fractal objects.

After this model was introduced, several authors (Meakin 1983b, 1986, Rácz and Vicsék 1983, Bensimon *et al* 1983, Ball *et al* 1985) have also investigated its characterizations in more detail and in more sophisticated ways. Some extensions of this model were reported and these are described below.

a) Sticking probabilities

An interesting extension (Meakin 1983b) of the DLA model consists in introducing a sticking probability p, when the diffusive particle reaches a site nearest neighbor to the aggregate. It was found that the fractal properties are independent of p in the range of $0.1 \leq p \leq 1$. However, when p is small, the

aggregate is apparently more compact. In the limit $p \rightarrow 0$, the aggregate starts to grow as in the Eden model.

b) Trajectories or mean free path

Another extension has been suggested by Bensimon and collaborators (1983). They pointed out that in the DLA model the mean free path l used for the particle diffusion is chosen equal to the characteristic distance between particles. The mean free path is exactly the lattice spacing when one works on a lattice. An interesting limit is the case where the mean free path becomes very large. In the limit of $l \rightarrow \infty$, the aggregate grows into another model, called the ballistic model (Vold 1963), in which the particles follow straight line trajectories rather than the random walk. It is interesting to study the "cross-over" between the two regimes governed by different models.

c) Geometries

Extensions of the original DLA model have been introduced where the seed particle is replaced by an infinite line or infinite plane. The aggregates then grow into different geometries, such as a tree-like cluster in 2-dimensions or 3-dimensions. Another interesting geometry has been obtained from the anisotropy effect. One way to impose anisotropy is to make the sticking probability direction dependent (Ball *et al* 1985). Numerical results show that the overall shape (or envelope) of this kind of anisotropic aggregate depends on the symmetry of the subjacent lattice.

1.2.3 Cluster-cluster aggregation model

The DLA model described in 1.2.2 was the first simple model able to describe irreversible random processes and to generate fascinating fractal structures. The model was also able to interpret a large number of chemical and physical phenomena. However, it was not able to describe most of the regular aggregation processes, such as those encountered in colloids and aerosols. In these phenomena, the aggregates themselves are able to move (diffuse) in space and stick to one another. In 1983, two years after the introduction of the DLA model, the cluster-cluster aggregation model was independently suggested by Meakin (1983a) and Kolb (1983).

The original cluster-cluster aggregation model is described here. Consider on a square lattice N aggregates in a square box. Each aggregate contains one particle in the starting situation. When, on their diffusing way, two aggregates come into a neighboring position, they irreversibly stick to form a new single aggregate (or cluster) which will be able to diffuse and stick to other aggregates or clusters. Thus, when such a collision occurs, the total number of aggregates decreases by one. This integrative process will stop when there remains only a single aggregate in the box. Figure 1.3(c) shows cluster-cluster aggregates with a total of 5000 site clusters (or particles) (Meakin 1983a). In the cluster-cluster aggregation model there are some features considerably different from the DLA model. For example, the aggregates obtained from the cluster-cluster aggregation exhibit quite different shapes than the DLA clusters, resulting in a difference in their fractal dimensions. Some extensions to this model were also reported (Meakin and

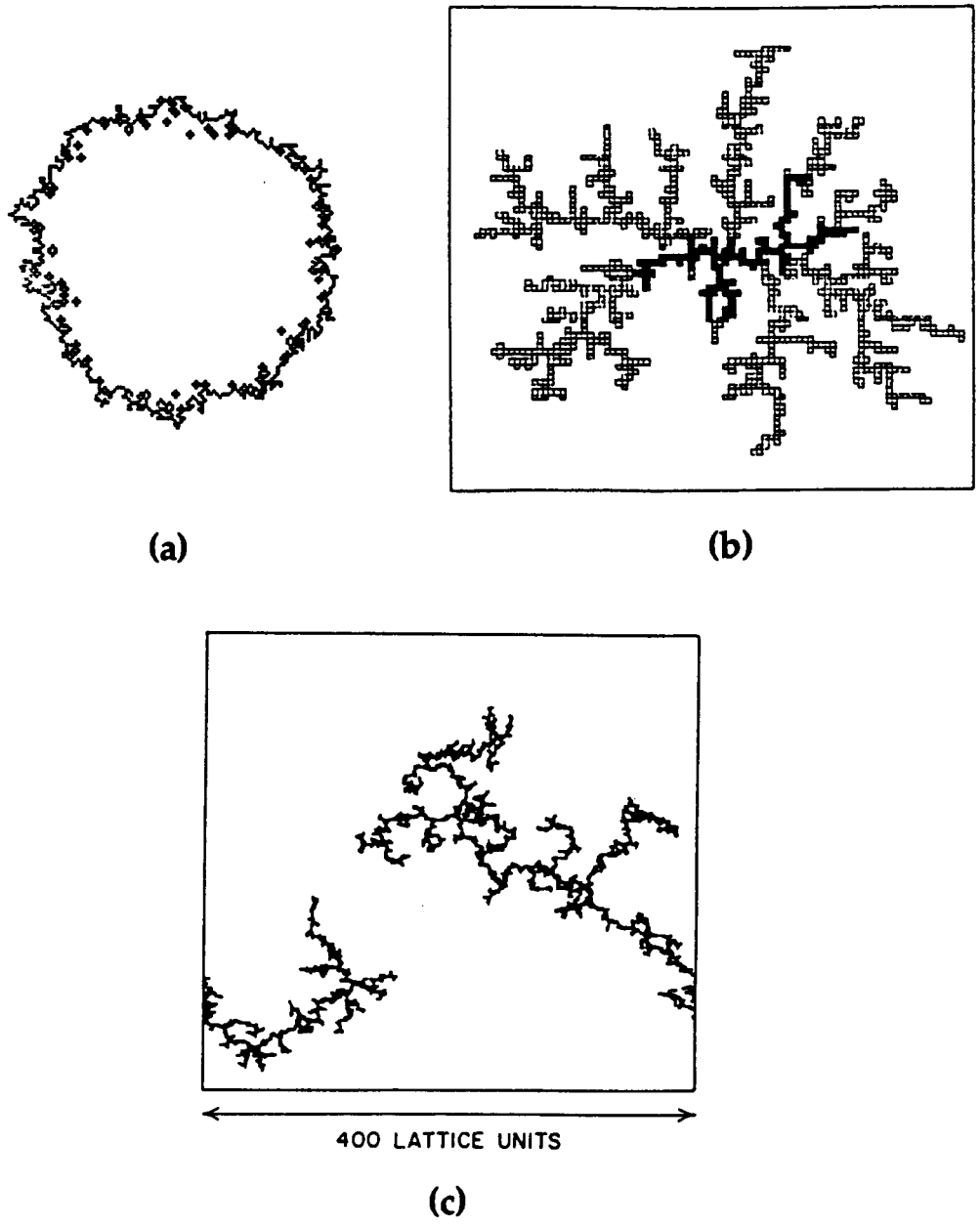

Figure 1.2 (a) Eden cluster of 8000 particles built on a square lattice. (b) A typical Witten-Sander aggregate containing 1024 particles. (c) A 5000 site clusters (particles) grown on a 400 X 400 two dimensional square lattice

Wasserman 1984, Jullien 1984).

1.3 Computer simulation of DLA

As mentioned in 1.1 and 1.2, there are various types of aggregate formed in nature and several models introduced to explain these phenomena. In our experiment, we observed fractal cluster formation on SnO_2 thin films that can be described in terms of the diffusion limited aggregation model (DLA). Thus, we will focus on the DLA model in the following sections, and will discuss our experimental results using this model.

1.3.1 Equations

Many growth processes in nature are described by the diffusion equation:

$$\frac{\partial u(\underline{x}, t)}{\partial t} = C \nabla^2 u \qquad (1.1)$$

where $u(\underline{x}, t)$ is a field-like variable which may denote pressure, concentration or temperature. C is a diffusion coefficient.

When the time derivative in eqn (1.1) can be neglected, the diffusion equation reduces to the Laplace equation:

$$\nabla^2 u(\underline{x}, t) = 0 \qquad (1.2)$$

with appropriate boundary conditions. For example, in the case of electrodeposition, the distribution of the electric potential satisfies eqn. (1.2) because there are no sources of charge present (Grier *et al* 1987). Then, the normal velocity of the interface is given by the first boundary condition:

$$v_n = -c\, \underline{n} \cdot \nabla u(\underline{x}, t) \qquad (1.3)$$

where c is a constant and $\underline{n}$ denotes the unit vector normal to the interface. Thus the local interfacial velocity is proportional to the gradient of the field. Far away, the field is a constant and isotropic:

$$u_\infty(\underline{x}, t) = \text{Const.} \qquad (1.4)$$

Finally, if the particles stick irreversibly on the cluster and never escape, the boundary condition on the growth interface is:

$$u(\underline{x}, t) = 0 \qquad (1.5)$$

These equations describe the unstable non-linear nature of interfacial pattern formation.

In the original version of the DLA model, Witten and Sander (1981, 1983) made an attempt to relate the DLA cluster growth model to these equations.

Let $u(\underline{x}\, t')$ be the probability that a randomly walking particle released far from the interface reaches site $\underline{x}$ after having made t' steps on the lattice. If the particle visits $\underline{x}$ at $t'+1$, it must have been at a nearest neighbor of $\underline{x}$ at t'. By considering Z nearest neighbors, the probability $u(\underline{x}, t'+1)$ can be expressed by (Vicsek 1989):

$$u(\underline{x}, t'+1) = \frac{1}{z} \sum u(\underline{x}+\underline{a}, t') \qquad (1.6a)$$

where $\underline{a}$ runs over the Z neighbors of site $\underline{x}$. In terms of a small time step τ and lattice spacing "a", the eqn. (1.6a) can be re-expressed as (Witten, 1986):

$$\tau \frac{\partial u}{\partial t'} + \frac{1}{2}\tau^2 \frac{\partial^2 u}{\partial t'^2} + \cdots\cdots = \frac{a^2}{2}\nabla^2 u + 0(a^4 \nabla^4 u) \qquad (1.6b)$$

Obviously, the eqn. (1.6a) represents the discrete version of the continuum diffusion eqn. (1.1). Since in the DLA model particles are released one by one, the changes in time are slow. The DLA model, thus, is the extreme implementation of diffusion limited growth and obeys the Laplace's equation (1.2).

The probability that the perimeter site r gains a particle at $t'+1$ can be expressed analogously to the velocity of the interface given by eqn. (1.3). Since in the DLA model, the particles, released from distant points with a steady flux, stick irreversibly on the cluster, we have the boundary conditions (1.4) and (1.5).

1.3.2 *Simulation of DLA*

Numerical simulations of the DLA process were first carried out by Witten and Sander (1981). Figure 1.3 shows an original version of DLA simulation in two dimensions using a square lattice. Particles are launched from distant points on a circle with a radius $r_{max} + 5$. The r_{max} is a maximum radius of the cluster. Then they undergo a random walk on the lattice until they either reach an unoccupied lattice site with an occupied nearest neighbor (as shown as trajectory **t1** in the figure) or they wander a large distance from the cluster (trajectory **t2**). Particles which are wandering far away from the cluster, typically 3 times the aggregate size, are removed and a new particle is started off from the launching circle. Repeating the same procedure a cluster is formed. The different size clusters in the range of $1000 < N < 100{,}000$ have been simulated by computer (Meakin 1983b, Meakin and Sander 1985). The structure of these clusters was characterized by the dependence of the radius of gyration on cluster mass or by the two point density-density correlation function which will be described in the next section. These parameters are insensitive to model details, such as the lattice type: square or triangle, on lattice or off lattice etc. (Meakin 1986a, 1986b), and the sticking probability in the range of $0.1 < p, < 1.0$ (Meakin 1983b).

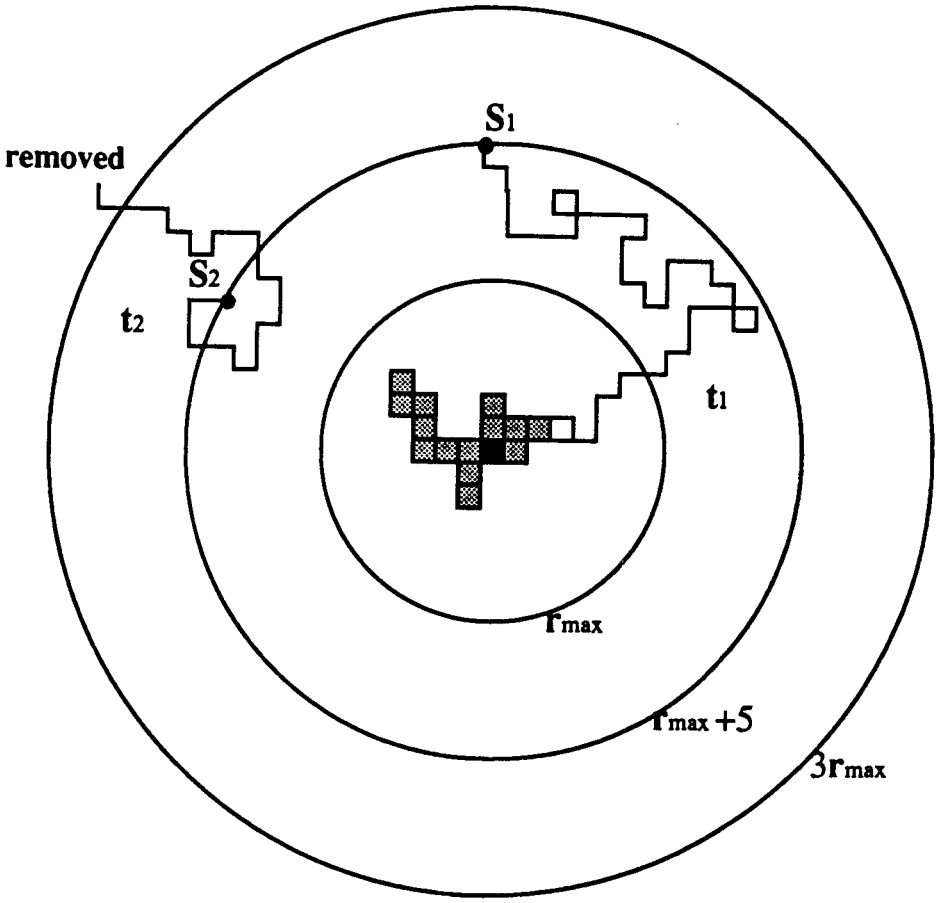

Figure 1.3 The simulation of a two dimensional DLA using a square lattice. The two particles' trajectories (**t1** and **t2**) start at random points (**s1** and **s2**) on the "launching circle". Trajectory **t1** reaches an unoccupied interface site, while trajectory **t2**, which is wandering away from the cluster, is removed.

1.4 Universal properties of fractals

1.4.1 Fractal dimension

One of most common approaches to study the fractal structure is to determine the fractal dimension of a growing cluster. In general, the mass **M** of the fractal as a function of the linear size **L** of the object obeys an equation of the form $M = L^D$, where **D** is the fractal dimension, a non-integer number for fractals and an integer for compact structures.

The fractal dimension of DLA clusters can be mathematically estimated by determining the radius of gyration $R_g(N)$ as a function of the mass of the cluster (or number of particles) which follows a power law:

$$R_g(N) \sim N^{1/D} \qquad (1.7a)$$

The radius of gyration $R_g(N)$ is obtained from:

$$R_g^2(N) = \frac{1}{N} \sum (r_i - r_c)^2 \qquad (1.7b)$$

where $r_i - r_c$ is the distance of the ith particle from the center of mass of the cluster. N is the total number of particles in the cluster at a given stage of the growth process.

The fractal dimension of a growing structure can also be estimated from the density-density correlation function (Witten and Sander 1981):

$$C(\mathbf{r}) = \frac{1}{N} \Sigma \rho(\underline{\mathbf{r}}+\underline{\mathbf{r}}')\rho(\underline{\mathbf{r}}') \qquad (1.8a)$$

This equation gives the probability of finding a particle at the position $\underline{\mathbf{r}}+\underline{\mathbf{r}}'$, if there is one at $\underline{\mathbf{r}}'$. In this equation, ρ is the local density which is defined to be 1 for the occupied sites and 0 for the others. It can be shown that $C(\mathbf{r})$ obeys a power law (Vicsék 1989):

$$C(\mathbf{r}) \sim \mathbf{r}^{\alpha} \qquad (1.8b)$$

with $\alpha = \mathbf{D} - \mathbf{d}_0$, where $\mathbf{d}_0$ is the dimension of the space in which the cluster grows. The fractal dimensions $\mathbf{D}$ of DLA clusters grown in $2 \leq \mathbf{d}_0 \leq 6$ dimensions have been estimated as listed in Table 1.1. The results are in good agreement with the relationship $\mathbf{D} = \frac{(\mathbf{d}_0^2+1)}{(\mathbf{d}_0+1)}$ obtained from a mean-field prediction (Tokuyama and Kawasaki 1984).

The fractal dimensions from experimental results have been reported, for example, $\mathbf{D} = 1.66 \pm 0.03$ for electrochemical deposition (Matsushita *et al* 1984), and $\mathbf{D} = 1.70 \pm 0.05$ for viscous fingering (Daccord *et al* 1986b), both for $\mathbf{d}_0 = 2$.

Table 1.1 The fractal dimension **D** of DLA clusters grown on $2 \leq d_0 \leq 6$ dimensions. The mean-field prediction $D = (d_0^2+1)/(d_0+1)$ is also shown for comparison.

d_0	D	$(d_0^2+1)/(d_0+1)$
2	1.70 ± 0.06	1.667
3	2.53 ± 0.06	2.500
4	3.31 ± 0.10	3.400
5	4.20 ± 0.16	4.333
6	5.3	5.286

1.4.2 The scaling of the active zone

The structure of diffusion limited aggregates is complex and the fractal dimension itself is not enough to characterize its scaling properties. Plischke and Rácz (1984) first suggested that there exists an "active " region in the surface structure of a growing cluster, where newly arriving particles join the

existing cluster. This active zone, usually the outer part of the surface, moves outward and leaves behind a frozen structure. Numerical evidence was obtained by Monte Carlo simulations for two and three dimensional DLA (Rácz and Plischke 1985). According to the simulations, the active zone is well described in terms of a Gaussian probability density **P(r, N)dr** that the Nth particle is deposited within a shell of width **dr** at a distance **r** from the center of mass of the cluster. Figure 1.4 shows **P(r, N)** for DLA in two dimensional clusters for selected values of N=100, 400 and 900. The solid lines are Gaussian Fits of the form:

$$P(r, N) = \frac{1}{(2\pi)^{1/2}\sigma_N} \exp\{-\frac{(r-r_N)^2}{2\sigma_N^2}\} \qquad (1.9)$$

From this, the active zone of the clusters can be therefore characterized by two parameters: the mean deposition radius r_N and the width of the active zone σ_N. Double-logarithmic plots of r_N and σ_N were also performed by Plischke and Rácz, and a power-law behavior was found by fitting the data points to a straight line.

$$r_N \sim N^{\upsilon} \quad \text{and} \quad \sigma_N \sim N^{\upsilon'} \qquad (1.10)$$

The two exponents υ and υ' were estimated to be 0.584 ± 0.02 and 0.48 ± 0.01, respectively, for the cluster size $200 < N < 2500$ (Plischke and Rácz 1984).

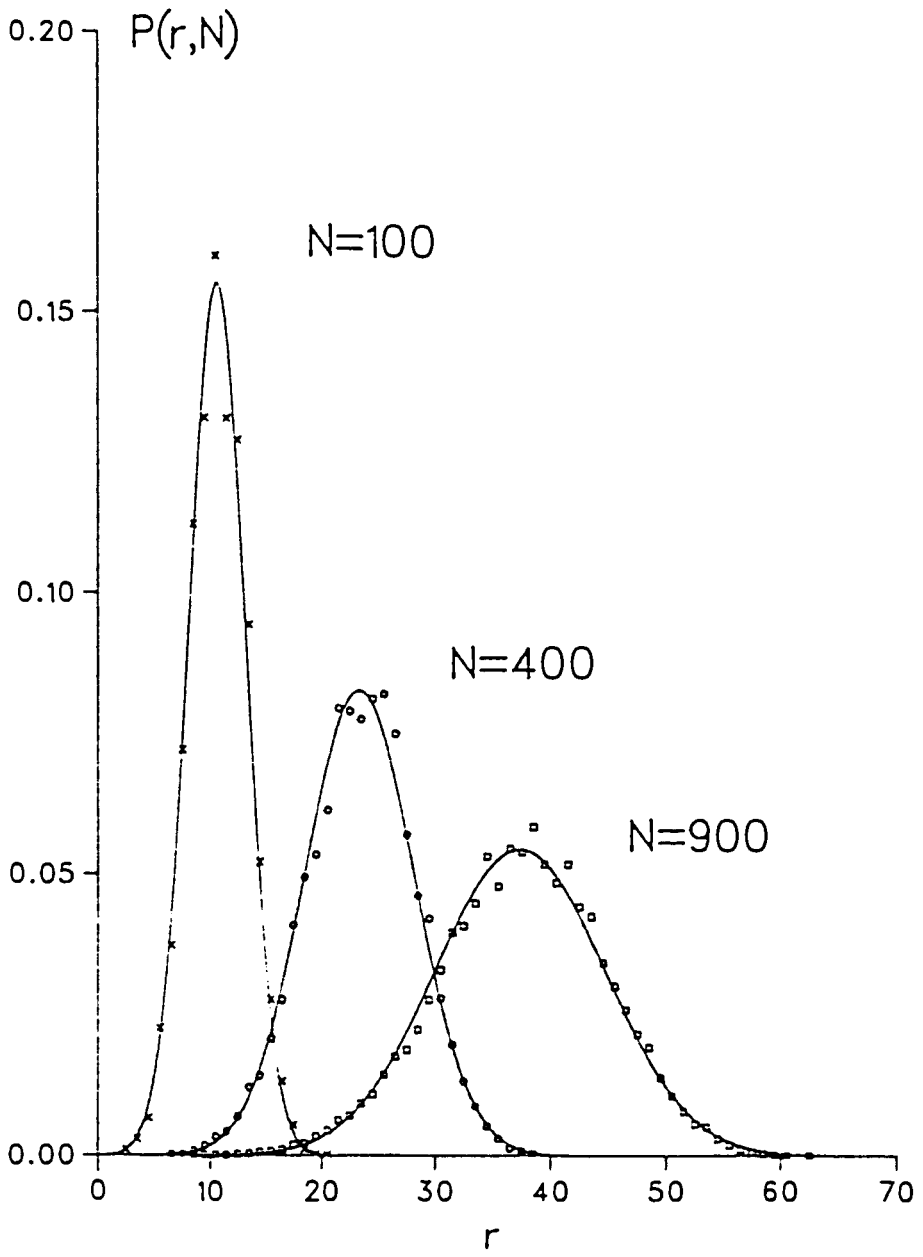

Figure 1.4 Probability **P(r, N)** of the Nth particle be attached at a distance **r** from the center of mass of the clusters for DLA in $d_0 = 2$. The solid lines are the Gaussian fits to averages over 200 clusters.

Chapter 2

Materials and Experimental Techniques

2.1 Preparation of SnO_2 films

Tin oxide SnO_2 (or fluorine doped SnO_2 : F) films were prepared on different substrates (glass, alumina, silica etc.) by aerosol spray pyrolysis (Zhang *et al* 1990, 1991, Zhou *et al* 1988) from aqueous solution containing 1M $SnCl_4 \cdot 5\ H_2O$ and 0.2M SnF_2. Figure 2.1 shows the schematic set up for the preparation of pyrolytically spray deposited SnO_2 films. An ultrasonic nebulizer (EN145 Medigas Pacific Ltd. Burnaby, B. C.) was used to generate an aerosol. A powerstat variable transformer was used to supply power for the electric heater and N_2 or air was used as a carrier gas. Prior to spraying, the substrates were heated to the required temperature that was measured by the thermocouple sensing temperature controller (Fenwal model 550). During spraying, the heater with the substrate could move forwards and backwards to obtain a uniform film.

The chemical reaction of the pyrolytic process may be written as:

$$SnCl_4 + 2H_2O \longrightarrow SnO_2 + 4HCl \qquad (2.1)$$

The thickness of SnO_2 films was controlled by varying the spraying time, and the substrate temperature was varied by changing the applied heating voltage.

2.2 Measurements of film thickness and surface resistance

For the thickness measurement of SnO_2 films, four random holes were made in each film by placing a small amount of Zn powder on the film and then adding a drop of concentrated HCl solution. After reaction, the mixture was rinsed from the film with distilled water and dried. The thickness of the film was then measured using a Wild Microscope 20 (Wild of Canada Limited) by the interference fringe step method:

$$t_0 = \frac{\lambda_0}{2} \frac{a_0}{b_0} \qquad (2.2)$$

where λ_0 is the wavelength of high transmitted filter, a_0 the interference fringe step and b_0 the distance between two fringes. The measured error is estimated at ±20 nm.

The surface resistance or sheet resistance of SnO_2 films on square samples was measured by a two-point probe method.

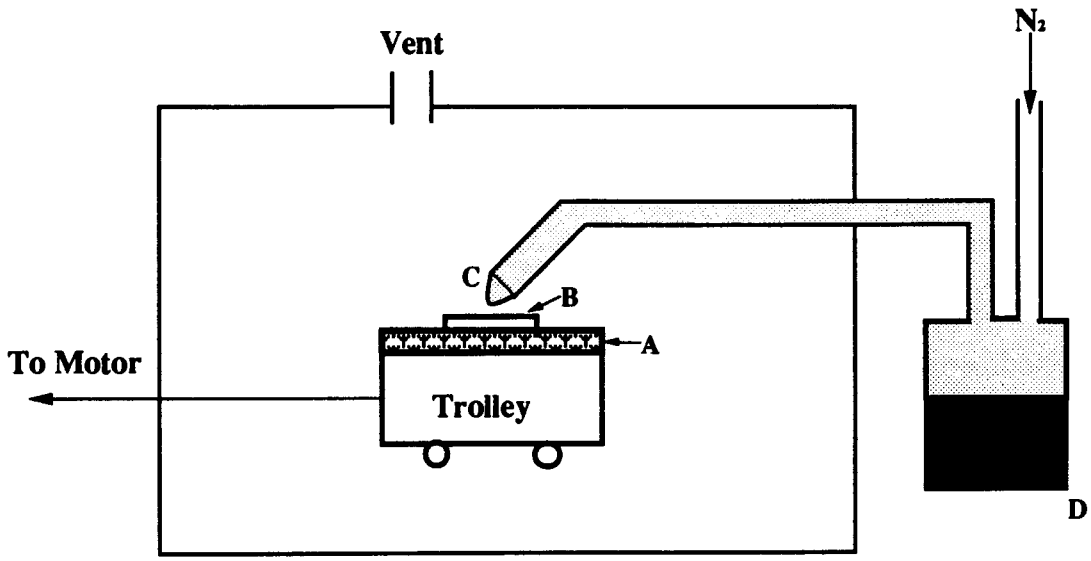

A: Electrical Heater
B: Substrate
C: Spray Nozzle
D: Nebulizer

Figure 2.1 Schematic of pyrolytic spray deposition unit

2.3 Experimental arrangements for pattern growth on SnO_2 film

Each tin oxide film on the substrate was cut into squares of side 2.5 cm. Silver dag, a colloidal solution of fine silver powder in a methyl isobutyl ketone solvent ($C_6H_{12}O$), was applied to the tin oxide film surface as the diffusion sources as well as the electrical contacts. Two contacts with small circular dots or strips were about 1.5 cm apart. After the silver dag dried, the sample was placed in a small open air oven while a DC voltage was applied across the contacts. The oven was heated by heating tape and the temperature was measured with a chromel-alumel thermocouple. The pattern growth processes were observed under a microscope with a video camera and stored in a PC computer. A schematic diagram of the experiment is shown in Figure 2.2. Pictures of image of patterns were also taken by a microscope (Wild Model 20) with micro-photoautomat.

2.4 X-ray diffraction studies

X-ray diffraction (XRD) spectra were obtained using an X-ray generator system (Model: PW1730 Philips Electronic Instruments Inc., Mahwah, N. J.) with CuKα radiation. The voltage applied to the X-ray tube was 50 kV and the current 35 mA. By analyzing peaks in the diffraction pattern of the polycrystalline samples, the space between adjacent parallel lattice planes (d-spacing) was found from the Bragg relation (Nuffield 1966):

$$d = \frac{n\lambda}{2\sin\theta} \qquad (2.3)$$

where **n** is the order of the diffraction spectrum, λ is the wavelength of CuKα radiation, and θ is the diffraction angle. The diffraction peaks were assigned to the corresponding crystal planes by comparing the experimental d-spacings from the diffraction pattern with theoretical d-spacings calculated from the lattice parameters and Miller indices (hlk).

For tetragonal SnO_2 film, the d-spacing was calculated from the formula (Nuffield 1966):

$$\frac{1}{d^2} = \frac{h^2+k^2}{a^2} + \frac{l^2}{c^2} \qquad (2.4)$$

where a = 4.747 Å, and c = 3.191 Å (Mirkin 1964).

For cubic Ag and AgCl, the theoretical d-spacing was obtained by using the equation:

$$\frac{1}{d^2} = \frac{h^2+k^2+l^2}{a^2} \qquad (2.5)$$

where a = 4.086 Å for Ag and a = 5.549 Å for AgCl (Mirkin 1964).

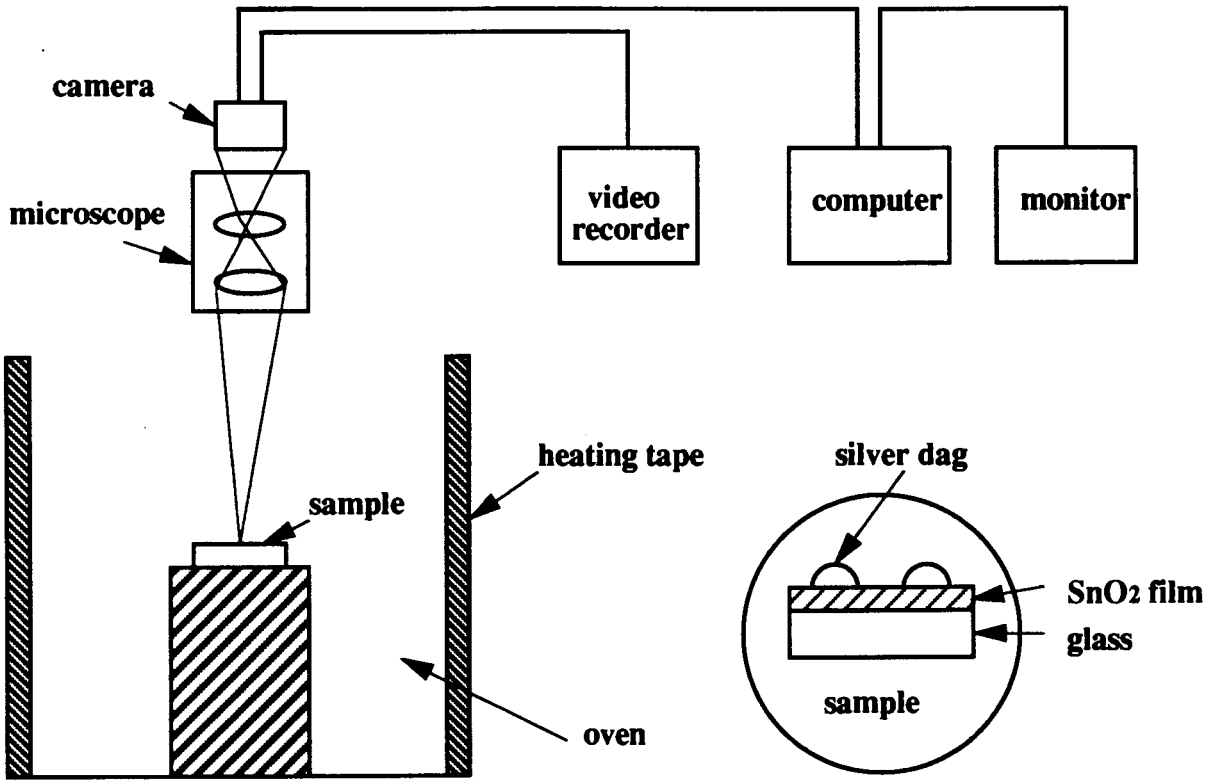

Figure 2.2 Schematic diagram of the experimental set-up

2.5 SEM and AES measurements

The electron microscope pictures were taken with a Model ISI-DS 130 (International Scientific Instruments, Santa Clara, CA) scanning electron microscope, while Auger analyses of samples were performed using a scanning Auger microprobe instrument (Model PHI 595, Physical Electronics, Minneapolis, MN.).

2.6 Computer programs

In this research work, several computer programs have been used.

To view, record and review the pattern growth process, we used the programs " DT2871", "TL" and "DISPLAY".

To digitize and plot clusters graphically, the programs "TAB", "BIG" and "GRAF" were used.

To calculate the cluster parameters, such as fractal dimension and Gaussian distribution, the programs "IGORF-PROCEDURE" and "GAUS.FIT" were created.

These programs are available in our lab.

Chapter 3

Fractal Pattern Formation on SnO_2 Films

3.1 Crystallinity and resistivity of pyrolytic spray deposited SnO_2 films

The crystallinity of pyrolytic spray deposited SnO_2 films is strongly dependent on the deposition temperature. Figure 3.1(a) shows the typical X-ray diffraction spectra for SnO_2 films deposited on glass slides at substrate temperatures ranging from 250 ^{0}C to 450 ^{0}C. The thickness of the samples ranged from 0.5 to 1 μm. It was found that the films prepared at temperatures above 400 ^{0}C were polycrystalline while those below 350 ^{0}C were amorphous. By comparing the d-spacing calculated from the lattice constants a = b = 4.747Å and c = 3.191 Å, the main peaks in the X-ray diffraction spectra of polycrystalline films were assigned to the planes SnO_2 (110), (101), (200), (211), (310) and (301). The films were predominantly oriented with the SnO_2 (200) plane parallel to the substrate surface. The observed diffraction spectra of pyrolytic spray deposited SnO_2 films were similar to the spectrum obtained from SnO_2 powder except some additional peaks SnO_2 (220), (002) and (112) were observed in SnO_2 powder as shown in Fig. 3.1(b). Comparison of peak positions, relative intensities and d-spacings for SnO_2 powder and SnO_2 film

is shown in Table 3.1.

Table 3.1 XRD peak positions, relative intensities, crystal planes and d-spacings for SnO_2 powder and SnO_2 film (prepared at 450 ^{0}C). The theoretical d-spacings for SnO_2 calculated from lattice constants and Miller indices (hkl) are also shown for comparison.

(hkl)	peak 2θ ±0.05 (deg.)		relative intensities		d-spacing (Å)		
	powder	film	powder	film	powder	film	theoretical
(110)	26.65	26.60	100	7	3.343	3.349	3.356
(101)	33.93	33.82	93	25	2.640	2.648	2.648
(200)	38.01	37.89	33	100	2.366	2.373	2.374
(211)	51.85	51.71	77	6	1.762	1.766	1.767
(220)	54.77	--	19	--	1.675	--	1.678
(002)	57.86	--	15	--	1.592	--	1.596
(310)	61.91	61.80	22	2	1.498	1.500	1.501
(112)	64.72	--	24	--	1.439	--	1.441
(301)	66.01	65.77	27	28	1.414	1.419	1.418

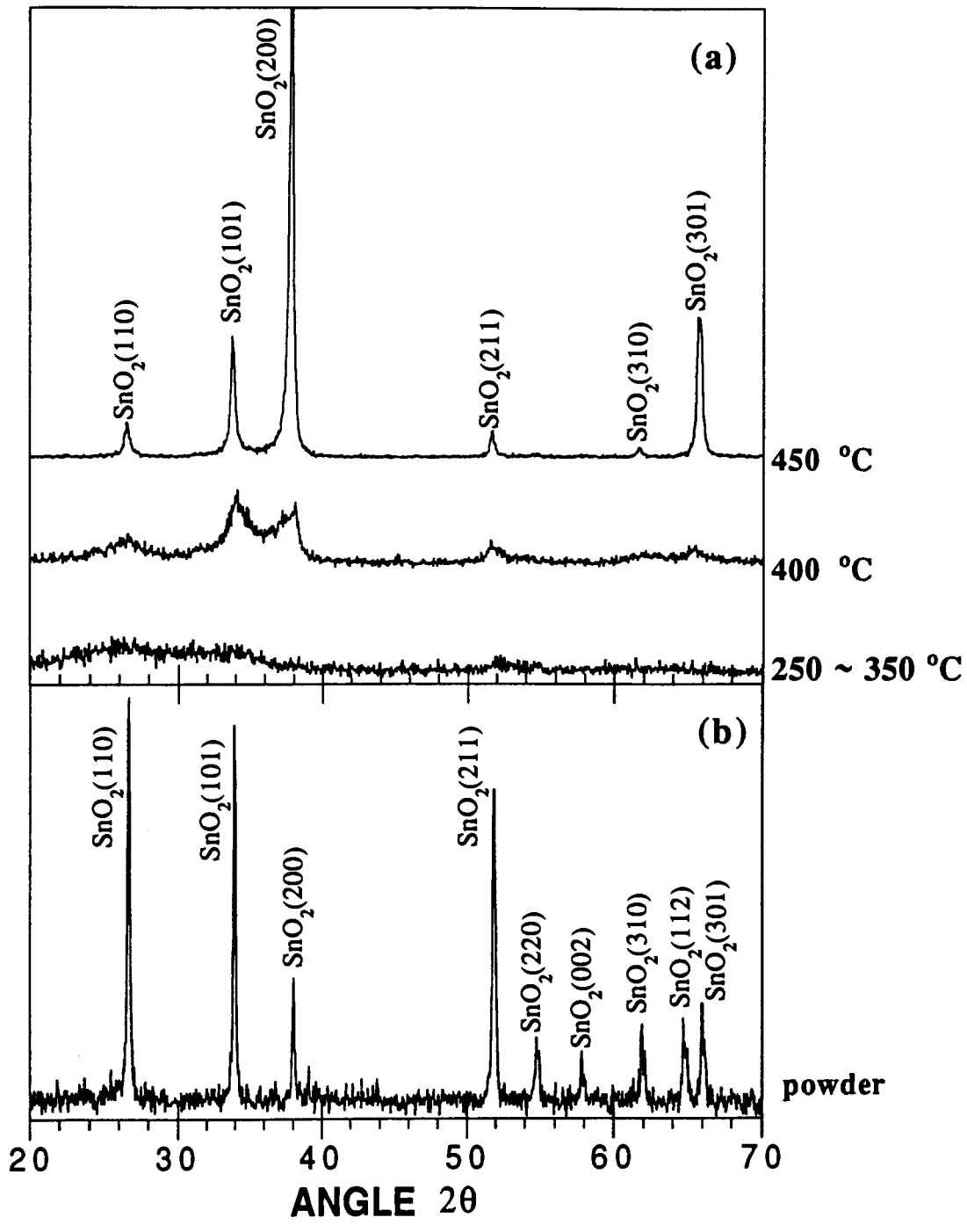

Figure 3.1 (a) XRD spectra of SnO_2 films deposited onto glass at different temperatures. (b) XRD spectrum obtained from SnO_2 powder.

Table 3.2 shows the dependence of the surface resistance of SnO_2 films on the deposition temperature. It was found that the films prepared at higher temperatures (400 to 450 ^{0}C) were more conductive with a sheet resistance of the order of 10 Ω per square, while those prepared at 250 to 300 ^{0}C had a sheet resistance in a range of megaohm per square.

SnO_2 films are nonstoichiometric n-type semiconductors, and their conductivity is due to the presence of foreign impurities, lattice vacancies, interstitial tins and F^- ions, which form a donor level just below the conduction band (Islam 1985).

Table 3.2 The sheet resistances of pyrolytic spray deposited SnO_2 films on glass at different deposition temperatures.

deposition temp. (^{0}C)	thickness (nm)	sheet resistance (Ω per square)
250	560	$> 10 \times 10^6$
300	600	5×10^6
350	650	3×10^3
400	530	80
450	740	10

3.2 Pattern formation on SnO_2 films

3.2.1 Observation of pattern growth on SnO_2 films

Pattern growth on two types of SnO_2 films, one prepared at ~ 425 ^{0}C with highly polycrystalline structure and low resistivity, and the other at ~ 300 ^{0}C with amorphous-like structure and high resistivity, were observed (Zhang and Colbow 1992, Sears and Colbow 1989). In both films, a 5 V DC bias was applied to the contacts after the sample was heated to 320 ± 20 ^{0}C in air. With the voltage applied and the temperature increasing slowly up to and then remaining at 380 ^{0}C, silver metal (or silver ions) diffused into and over the film. In the highly conductive film, metallic silver readily migrated over the film surface. After 1/2 to 1 hour, the DC bias and oven power supply were disconnected. However, in the highly resistive film the silver diffusion was very slow. The sample had to kept in the oven for a day or longer rather than hours as for the highly conductive films. No pattern was observed during heating for either type of film, but patterns suddenly appeared as the temperature dropped below 300 ^{0}C. The pattern growth is completed in seconds and there is no significant effect of the rate of temperature decrease on the pattern formation. In this thesis most of data used were obtained from the highly conductive films. Figure 3.2(a) and (b) show the photographic images near one of the contacts at a magnification of 40 times. Some additional experiments have also been carried out :

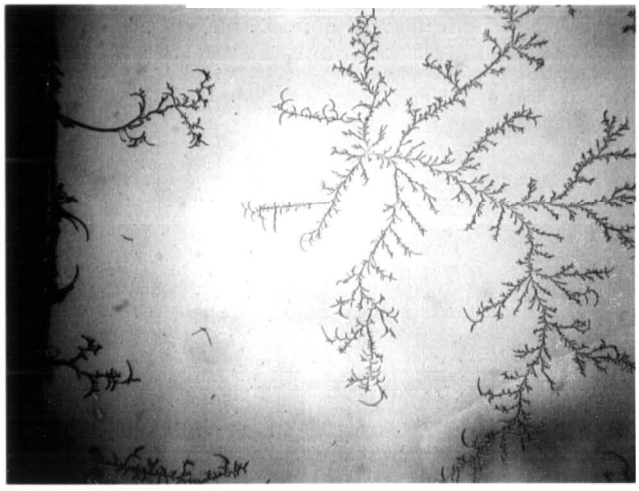

(a)

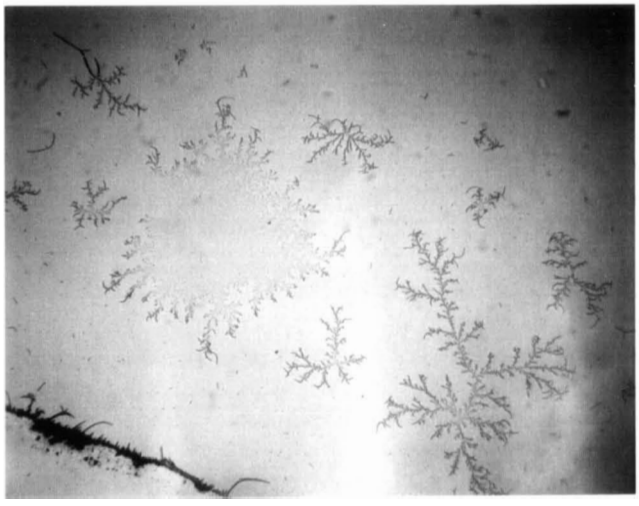

(b)

Figure 3.2

(a) and (b) Photograhps showing silver patterns on SnO_2 films at a magnification of 40X.

(1). The patterns were also observed without applied DC bias. With bias the patterns were observed at a larger distance from the contact and more patterns appeared at the positive electrode than without bias.

(2) An evaporated silver film of 1μm thickness, instead of silver dag, produced a similar patterns in a region near the edge of the silver film.

(3) All patterns disappeared when the sample was reheated to 350 ^{0}C and reappeared after cooling back down. However, the growth sites and shapes of patterns were considerably different from the previous ones due to the random aggregation.

As displayed in Figure 3.2(a) and (b), the patterns can be divided into three cases: (1) self-similar clusters which appeared in the region away from the silver contact, (2) tree-like clusters grown on the edge of the contact, and (3) typical clusters with dense packed structure which look like Eden cluster (Jullien and Botet 1987) as shown in Figure 3.2(b). In cases (1) and (2), pattern growth processes likely obey the DLA growth model (Witten and Sander 1981) with beautiful fractal structure, which will be discussed and studied in more details later. In the case (3), the patterns are compact, however, there exists DLA structures on the surface of the patterns. This can be explained by two possibilities: one is that the pattern is formed by another model or a modified DLA model, the other that some big clusters are joined to form a typical cluster which seems to resemble the diffusion limited aggregation at multiple growth sites (Witten and Meakin 1983).

3.2.2 *Effect of DC voltage on pattern selection*

As shown in the previous section, self-similar clusters were observed on the SnO_2 films when a smaller DC bias was applied or without DC bias. However, different shapes of patterns were obtained when the DC voltage was increased. Figure 3.3(a), (b) and (c) show the photographic images of the different types of patterns obtained with different DC applied: 3 V, 8 V and 10 V. At a smaller DC bias < 5 V, the patterns were mostly fractal structures as shown in Figure 3.2 and Figure 3.3(a). At a DC bias ranging from 5 V to 10 V, the pattern grew with the preferred direction along the direction of the electric field as shown in Fig. 3.3(b). At a DC > 10 V, the patterns grew further following the electric field line as shown in Fig. 3.3(c).

This can be explained qualitatively on the basis of the different motions of the metallic silver. At a small DC voltage, the pattern formation process is basically an aggregation process which can be described theoretically by the DLA model, where random walk trajectories are assumed. When the DC bias was large, the silver ions may move up the branch from the source and out onto the film thereby extending the branch roughly in the direction of the electrical field. In this case, the motion of the silver ions likely consists of ballistic trajectory (straight motion) rather than of random walks. In an intermediate case (5 V to 10 V), the motion of the silver ions could be a combination of the random walk and ballistic trajectories, resulting in the observed growth pattern along the direction of the electric field as shown in Fig. 3.3(b).

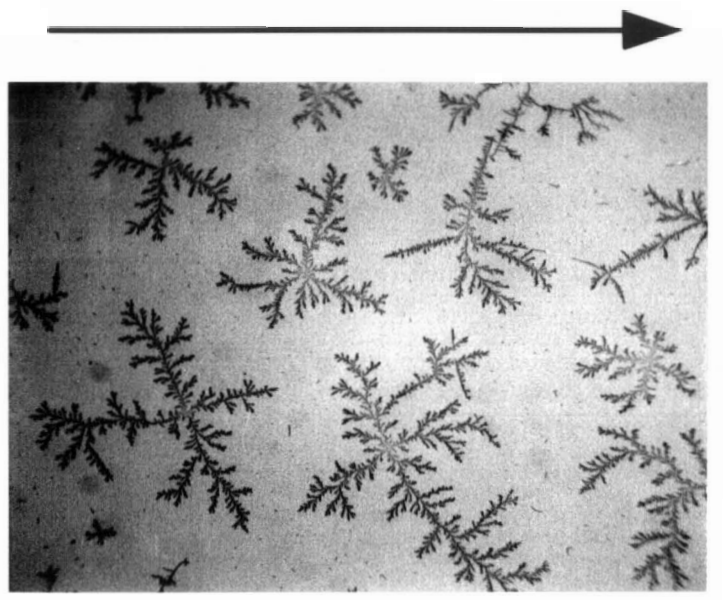

(a)

Figure 3.3 (a)

Photograph, at a magnification of 40X, showing patterns obtained from 3V DC bias. The arrow indicates the direction of DC electric field.

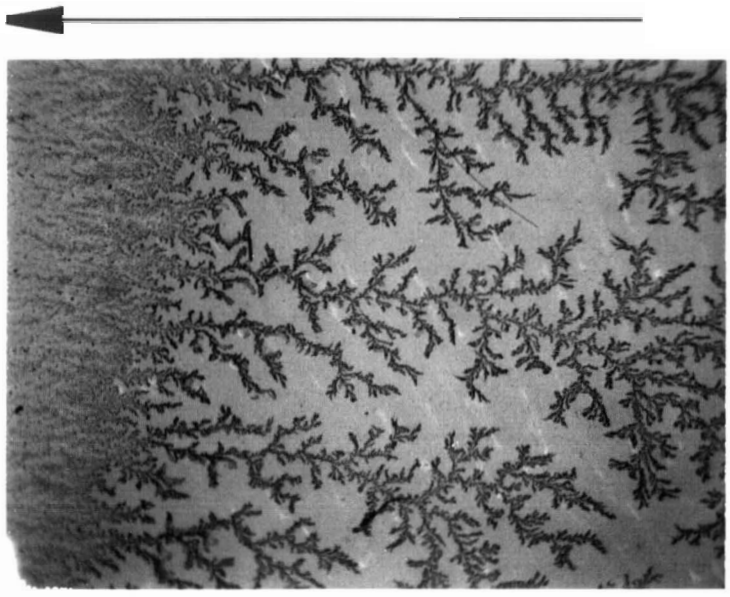

(b)

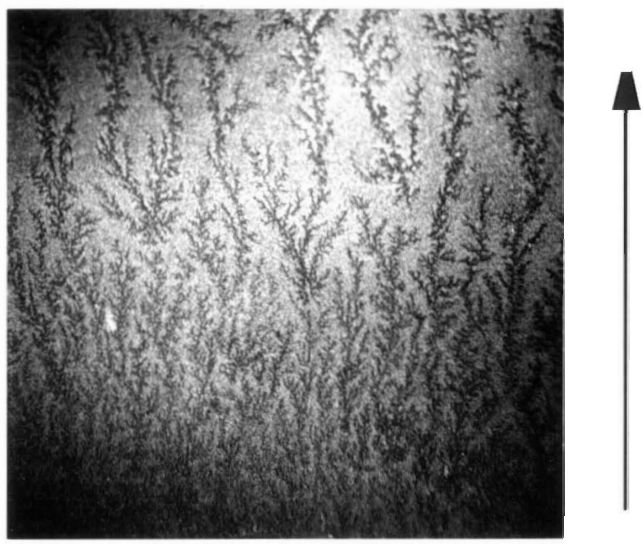

(c)

Figure 3.3(b) and (c)

Photographs, at a magnification of 40X, showing patterns obtained from DC bias 8V and 10V. The arrow indicates the direction of DC eletric field.

3.3 Surface observation of fractal patterns by SEM, AES and XRD

3.3.1 Scanning electron microscopy (SEM)

The scanning electron microscopy was performed to look at the fractal structures in more details. It was found that the size of patterns varied from ten to hundreds of micrometers. Figure 3.4(a) shows the SEM picture of a part of a self-similar cluster in the region away from the silver contact, while a typical tree-like cluster was observed at the edge of the contact as shown in Fig. 3.4(b). Figure 3.4(a) and (b) show that the branches of the patterns are isolated from each other. The reason for this will be explained in section 3.4. One can also notice in Fig. 3.4(b) that the branches curve toward the same direction due to the boundary condition at the edge of the contact. Figure 3.5 presents one branch in a larger magnification and with a specimen tilt x-axis angle of 60^0. The diameter of the branch is about 1 ~ 2 μm. One can see that the lower side edge on the branch is sharp and bright, while the upper one is diffuse. From this we could suggest the hypothesis that the patterns were grown on the surface of the tin oxide film. This hypothesis is enhanced by the further experiments which will be presented next.

3.3.2 Auger electron spectroscopy (AES)

In order to give further insight into this new type of aggregate, Auger scanning measurements were carried out. Figure 3.6 presents a series of the

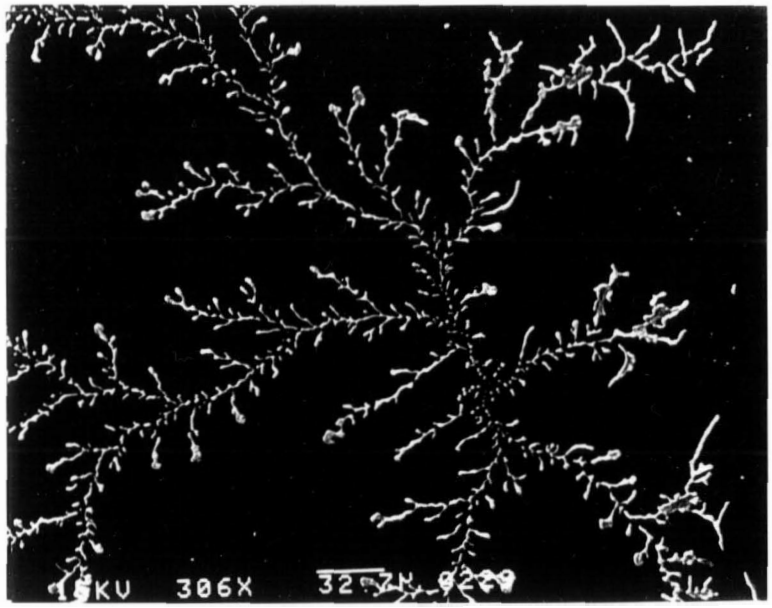

(a)

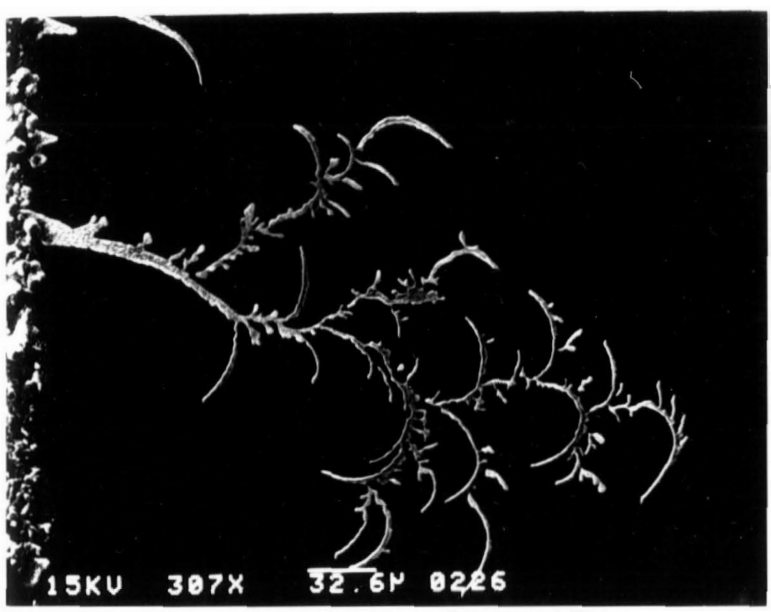

(b)

Figure 3.4

Electron micrographs showing surface morphology of fractal clusters grown on SnO_2 films (a) in the region away from the silver contact and (b) at the edge of the silver contact.

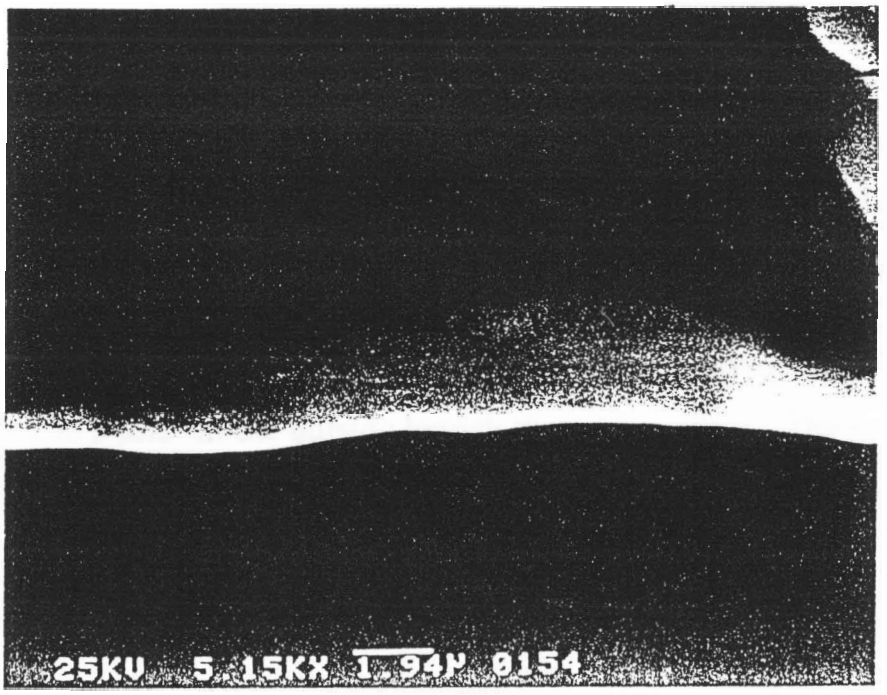

Figure 3.5 Electron micrograph showing one branch of cluster with higher magnification and with a specimen tilt x-axis angle 60^0.

Auger scanning images of Ag in the area of a branch of the cluster. The brightness of Auger maps is normalized with respect to the most intense Auger signal of the particular element, such that different gray shades indicate the varying concentration of the element. The bright spots in figure 3.6(a) show the highest concentration of Ag, while a lower concentration of Ag can be revealed by varying the gray shades as shown in Fig. 3.6(b) to (d). From Fig. 3.6 one can see that the Ag atoms are not uniformly distributed in the area, the Ag concentration is maximum in the middle, and decreases gradually toward the edge of the branch of the cluster. This was further indicated by Auger line scanning measurement.

Figure 3.7 presents the Auger line scanning of Ag, Sn, Cl and O across the branch shown in Fig. 3.6. The beam size used in the Scanning Auger Microprobe was 2 to 3 μm. In the outside branch there is no silver. The silver distribution on the inside branch resembles a Gaussian distribution, a fact, which may be useful for studies of DLA cluster in three dimensions of space. We also notice that there are oxygen atoms both on the inside and outside the branch, with larger concentration on the outside. This is most likely explained by the fact that the fractals consist of AgCl, perhaps Ag as well, with a thin layer of silver oxide on the metal surface, since only the surface layer is readily oxidized from the air and converted into silver oxide. To support this hypothesis, the sample was sputtered by a 3 KeV Ar^+ beam. After 5 minutes of sputtering, the measured Auger spectrum revealed no detectable oxygen inside the fractal cluster. Figure 3.8 shows the differential Auger spectra of (a) the initial SnO_2 film, (b) the cluster on the SnO_2 film surface and (c) the

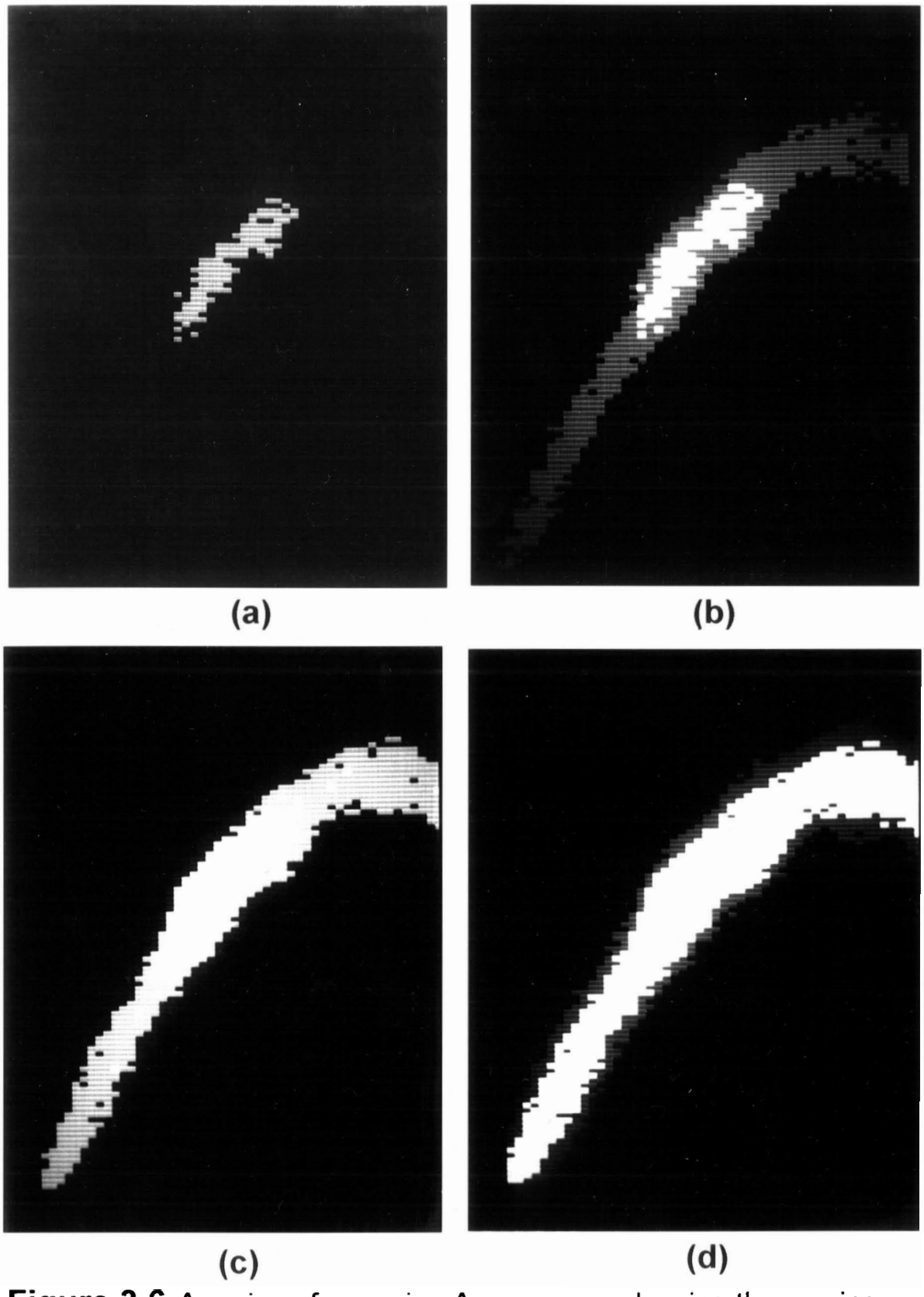

Figure 3.6 A series of scanning Auger maps showing the varying concentration of Ag by different gray shades from (a) weakest to (d) strongest Auger signal

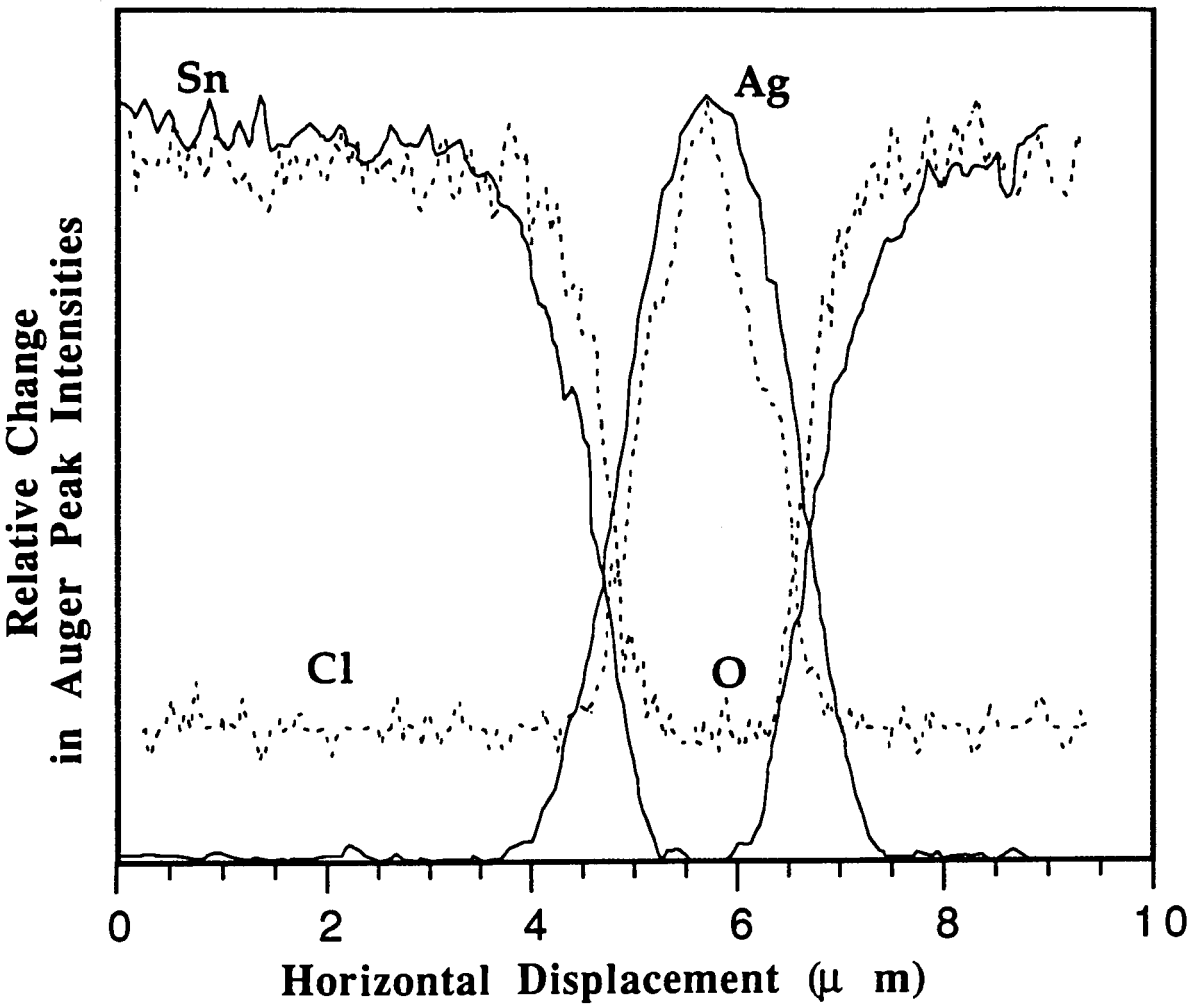

Figure 3.7 Auger line scanning of Sn, Ag , Cl and O. The Sn, Ag, Cl and O are normalized with respect to the most intense Sn, Ag, Cl and O signals.

cluster after 5 minutes of sputtering. In Figure 3.8(a) the two prominent peaks at 425 and 510 eV result from Sn and O. The peaks at 181 eV and 250 eV are due to chlorine and carbon which were present during the deposition of the SnO_2 film (Craigen *et al* 1987). Some of the carbons may be removed by washing with distilled water. After pattern formation, the differential Auger spectrum for the area outside the cluster is the same as in Fig. 3.8(a). In the Auger spectra from inside the cluster, shown in Fig. 3.8(b), the Sn peak disappeared and the new peak at 350 eV is due to Ag atoms. We also notice that the chlorine peak height increased and the oxygen peak decreased inside the cluster, which is consistent with the measurement from the Auger line scanning in Fig. 3.7. After sputtering for 5 minutes, the oxygen peak disappeared completely as indicated from Fig. 3.8(c).

In order to investigate quantitatively the relative concentrations of the elements, the intensities and sensitivity factors of the observed elements were considered. Table 3.3 lists the intensities, sensitivity factors and relative concentrations of these elements.

According to the quantitative analysis of the compositions of the cluster from the AES data, we found that the relative concentration of Ag is larger than Cl. Also, there exists a certain amount of O atoms. Therefore, it was concluded that the patterns are formed by metallic silver and silver chlorine with a thin layer of silver oxide on the surface.

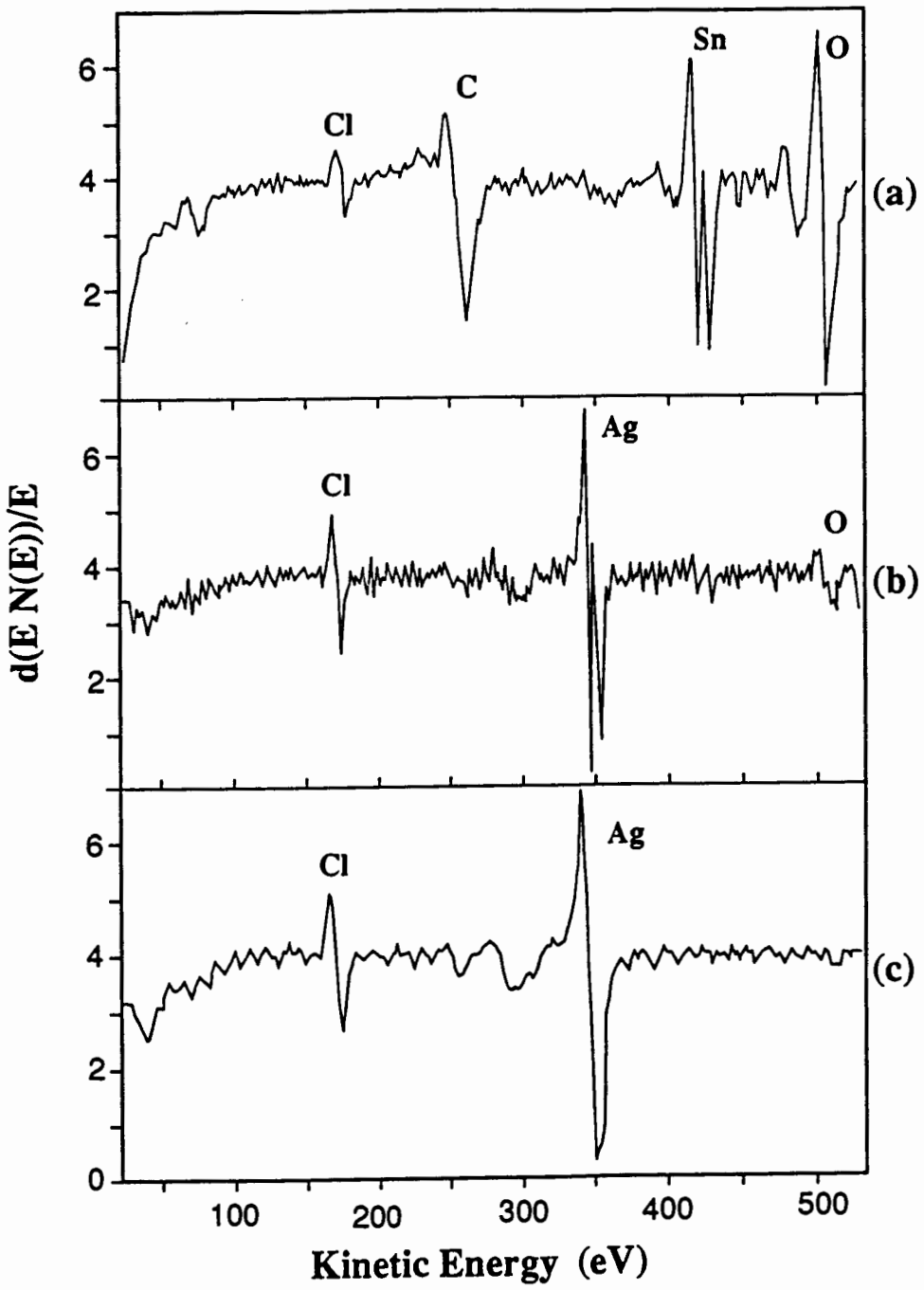

Figure 3.8 Differential Auger Spectra of (a) initial SnO_2 film on glass, (b) the cluster before the sputtering and (c) the cluster after argon sputtering

Table 3.3 Differential Auger peak intensities (peak to peak) and their relative element concentrations for Fig. 3.8 (a), (b) and (c). The sensitivity factors were also given in this table.

(a) SnO_2 film

element	relative intensity	sensitivity factor	element concentration
Sn	82	0.8	17%
O	100	0.5	33%
C	56	0.2	46%
Cl	22	1	4%

the cluster (b) before and (c) after sputtering

element	relative intensity		sensitivity factor	element concentration	
	(b) before sputtering	(c) after sputtering		(b) before sputtering	(c) after sputtering
Ag	100	100	0.9	62%	75%
Cl	38	37	1	21%	25%
O	15	0	0.5	17%	0%

3.3.3 *X-ray diffraction (XRD)*

In addition, XRD measurements were carried out. XRD spectra revealed that silver dag or evaporated silver film had cubic structure with lattice constant a = 4.090 ± 0.005 Å which is consistent with the literature value a = 4.08624 Å (Mirkin 1964). Figure 3.9(a) shows the XRD spectrum of silver dag on glass. The three XRD peaks at $2\theta = 37.95^0$, 44.15^0 and 64.30^0 correspond to planes Ag(111), (002) and (022). The peak at 51.50^0 is Ni(220) since the nickel foil was used as a substrate for high temperature x-ray measurement. After heating the silver dag to temperatures above 230 ^{0}C in air, some new peaks were observed as shown in Fig. 3.9(b). These peak heights (intensities) increased with increasing temperature up to 350 ^{0}C, shown in Fig. 3.9(c), indicating an increase of the relative concentration of this new component . Figure 3.9(d) shows the XRD spectrum for the sample after cooling back to the room temperature. To determine the structure of this new component, the Bragg peak position, as well as the intensity that is related to the geometrical structure factor, were carefully examined, and all Bragg peaks must be observed to have confirmation of a match. It was found that all these new observed peaks matched well with planes of AgCl with a = 5.549 Å as shown in Table 3.4. The source of chlorine was determined by SEM microanalysis. The SEM data showed that the atomic percent of Cl and Ag in the silver dag are 38 and 62 respectively, suggesting that the silver dag contains silver powder, a solvent and a chlorine containing binder. At higher temperature, the chlorine combines with silver forming AgCl. Therefore, the XRD measurements revealed that the structure of heated Ag dag is mainly a

Table 3.4 XRD peak positions, relative intensities, d-spacings and crystal planes (hkl) for Ag dag heated in air at 350 °C. Theoretical d-spacings and line intensities are also shown for comparison.

peak 2θ (deg.)	**(hlk)**	**relative intensity**	***line intensity***	**d-spacing**	***theoret. d-spacing***
27.50	AgCl(111)	33	*50*	3.240	*3.205*
31.95	AgCl(200)	100	*100*	2.798	*2.774*
45.85	AgCl(220)	38	*50*	1.975	*1.962*
54.45	AgCl(311)	11	*16*	1.683	*1.672*
57.10	AgCl(222)	8	*18*	1.612	*1.602*
37.85	Ag(111)	100	*100*	2.372	*2.356*
44.00	Ag(002)	55	*40*	2.055	*2.043*
64.10	Ag(220)	89	*25*	1.452	*1.445*

Note: Due to thermal expansion, all observed peak positions (2θ) were systematically lower than the expected angles by 0.2 to 0.4 degree (about 1 % higher for the d-spacings)

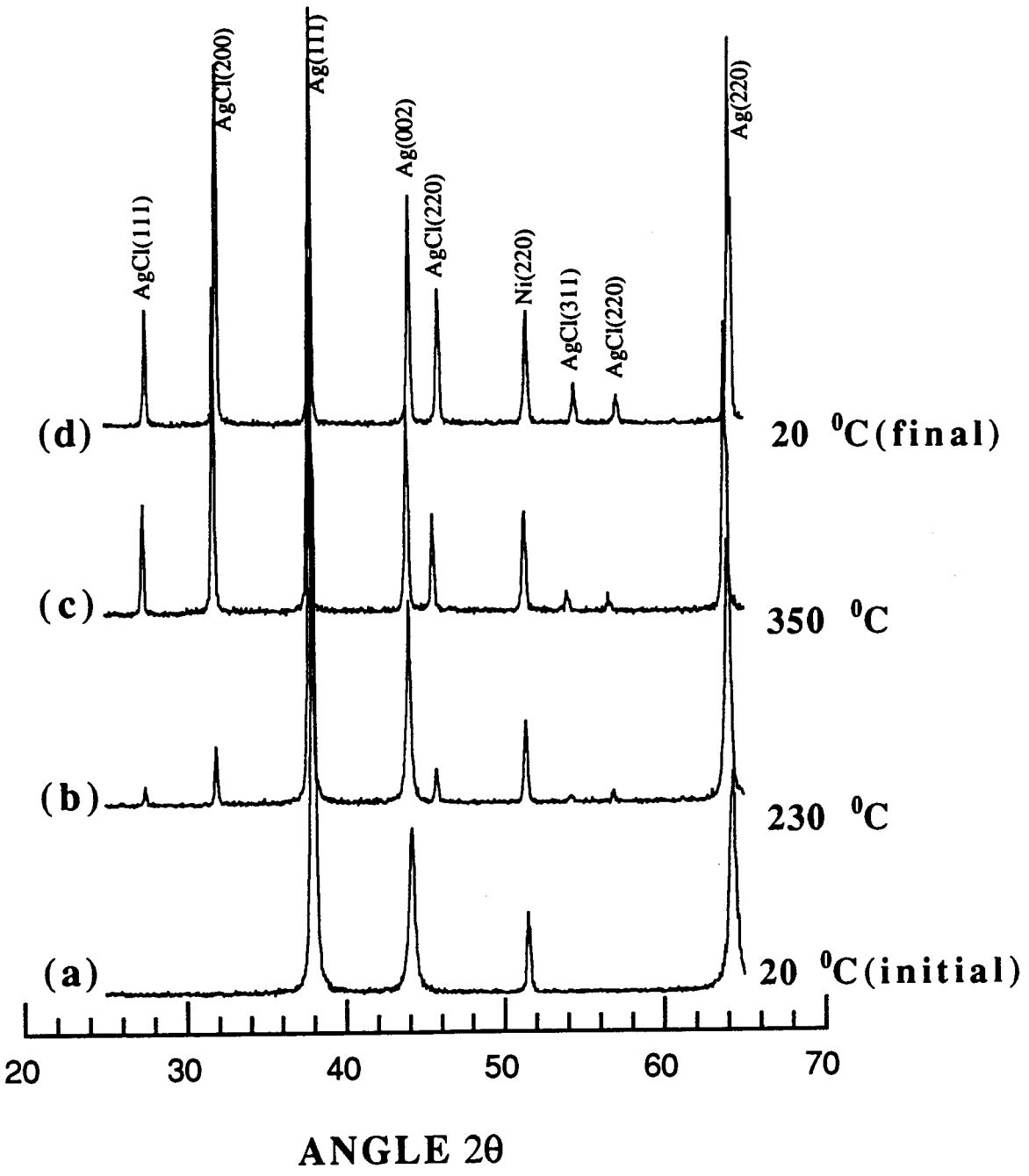

Figure 3.9 XRD spectra of (a) silver dag on glass, (b) and (c) silver dag heated in air at 230 °C and 350 °C respectively. (d) heated silver dag cooled back to room temperature.

mixture of Ag and AgCl. Table 3.4 lists these peak positions, relative intensities, d-spacings and crystal planes. Theoretical d-spacings and line intensities for these different planes are also quoted for comparison.

XRD spectra for Ag diffused onto tin oxide films were obtained as well. Figure 3.10 shows the XRD spectra of SnO_2 film before and after silver diffusion. Figure 3.10(a) is the XRD spectrum for polycrystalline SnO_2 film prepared at 400 ^{0}C. After silver diffusion, there are some additional peaks at $2\theta = 27.75^0$, 32.20^0 38.05^0 and 46.15^0, which could be associated with AgCl and Ag as shown in Fig. 3.10(b). These peaks, especially in Ag peaks, are weak due to the fact that the fractal clusters cover only a small portion on the SnO_2 surface. Figure 3.10(c) shows the XRD spectrum for dense pack patterns. From this one, we can clearly see the Ag and AgCl peaks. It was found that the intensities of these peaks varied from sample to sample because the patterns of these samples are different from each other.

In contrast with the AES data in 3.3.2, the Bragg peaks do not indicate silver oxide. This is probably explained by the fact that the oxygen only exists on the surface region of the cluster. Such a thin layer of surface silver oxide could not be detected by XRD. Matsushima *et al* (1988) also observed no evidence of the oxidation state of Ag and Pd from XRD analysis, but they did observe the oxidation state of surface metals by X-ray photoelectron spectrum (XPS). The similar observations of surface metal oxides by XPS were reported as well by Cheong *et al* (1992) and Tamaki *et al* (1992).

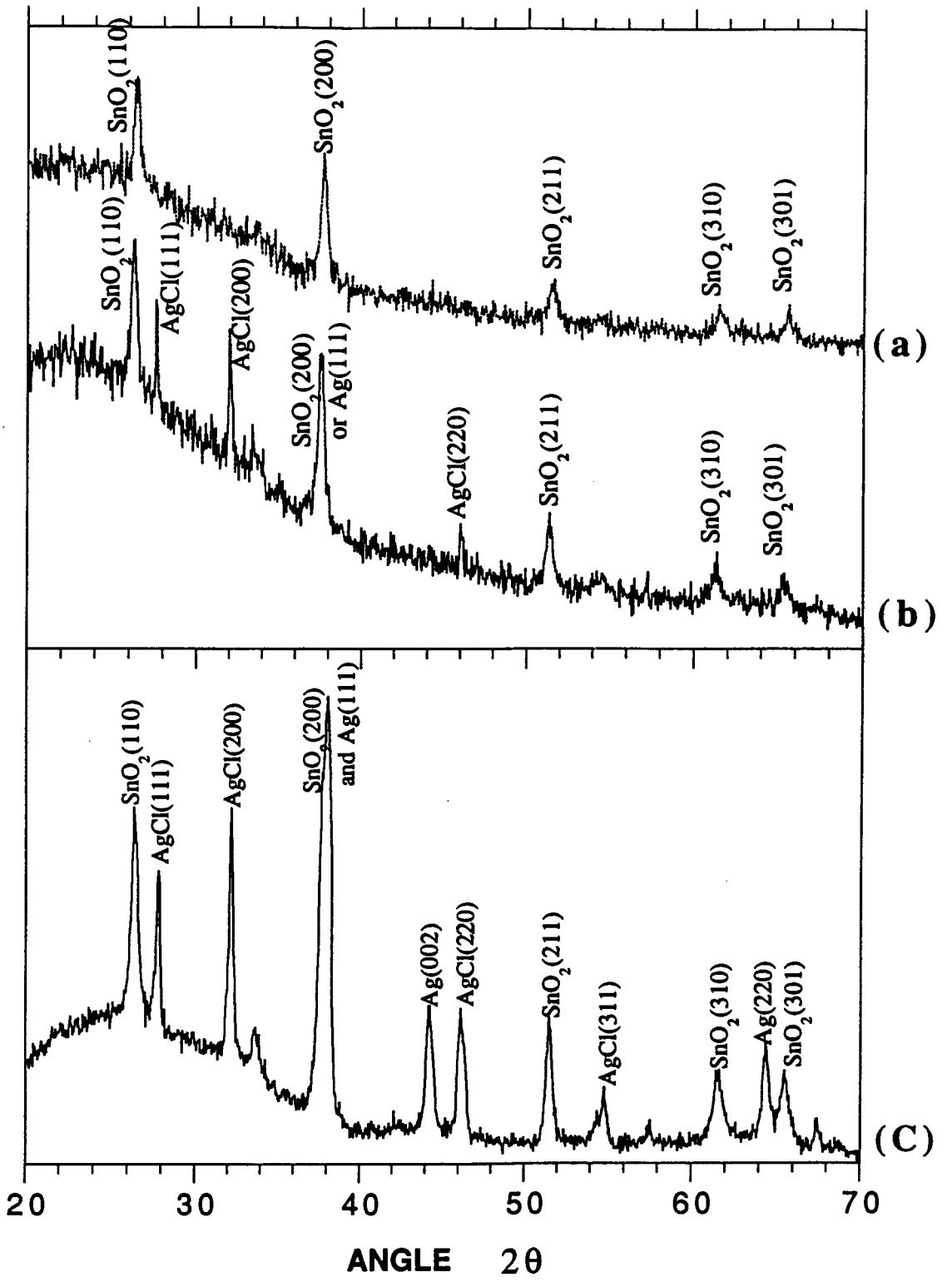

Figure 3.10 XRD spectra of SnO_2 film (a) before and (b), (c) after silver diffusion.

3.4 Explanation of pattern growth on SnO_2 films

We shall attempt to explain the mechanism for formation of this new type of aggregate on the SnO_2 film according to the experimental observations and data given in sections 3.2 and 3.3. A number of different growth mechanisms may be at work. However, the following one is considered most likely.

Silver or silver ions (Ag^+) may move on the n-type SnO_2 semiconductor surface above the silver oxide decomposition temperature of 300 ^{0}C after ejection from the silver contact (silver dag or silver film). These silver atoms or ions aggregate at nucleation points on the tin oxide surface at temperature of 300 ^{0}C. The first Ag attached to the nucleation point is considered as a seed. Then the next one, after releasing from the silver source, follows a random walk until it reaches the seed or another nucleation site. It will stick to become a newly added Ag. Repeating the same procedure, an aggregate is formed as illustrated in Fig. 3.11. More Ag would diffuse across the film for longer diffusion times and for higher temperatures, producing more aggregates and bigger clusters. These aggregated Ag atoms on the SnO_2 surface capture Cl from the SnO_2 forming AgCl. Since the formation of AgCl was observed at temperature of 230 ^{0}C as shown in the XRD measurement of Fig. 3.9. There are two important processes involved in this experiment: the Ag diffusion process and pattern growth process.

Silver (or silver ion) diffusion onto the surface of the film is influenced by some factors, such as the conductivity of the SnO_2 surface, the substrate temperature and the external voltage applied. It was found that the silver

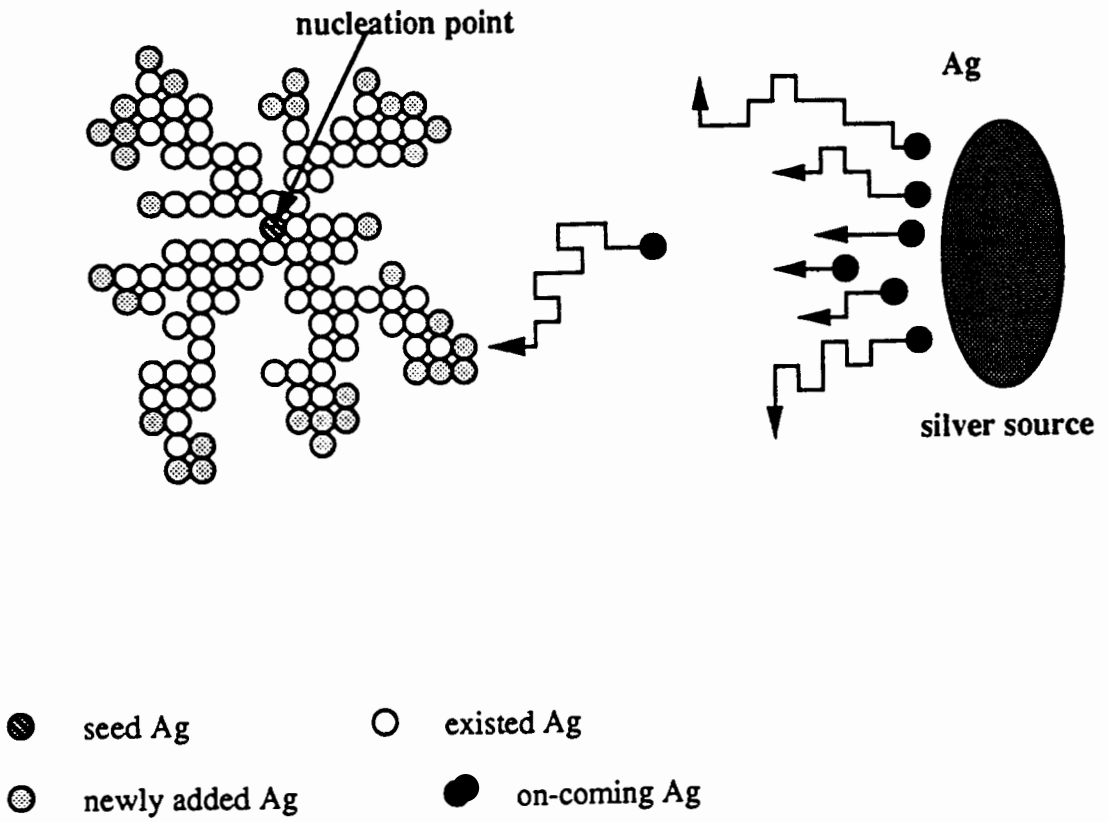

Figure 3.10 A sketch illustrating the silver aggregation at a nucleation point.

diffusion was not observed on pure silica or insulator surfaces, where the movement of free ions is somehow inhibited. Silver movement is hardly realized on a highly resistive SnO_2 film. However, silver readily migrates over polycrystalline SnO_2 surfaces with higher conductivity due to large grain boundaries and low barriers on the film surface. This is indicated by the experiment that the higher resistive sample had to be kept in the oven for a day or longer, while the higher conductive one needed only an hour to complete a similar diffusion distance. It was also observed that the silver diffusion occurred at a temperature above 300 ^{0}C.

Silver movement on the SnO_2 films is dependent on the DC voltage applied across the two contacts as discussed in the section 3.2.2. At a lower DC or without bias, the neutral silver atoms are likely to be more mobile and their movements are likely a random walk, thus resulting in fractal clusters similar to those simulated structures obtained from the DLA model. With increasing the DC bias, the silver charged ions tends to a ballistic trajectory along the direction of the electric field, which results in a preferred growth direction as shown in Fig. 3.3.

The growth process of the patterns basically is an aggregation process, which can be described theoretically by the DLA model. The patterns were observed only after the temperature was decreased to about 320^{0}C. (The difference between our observed value of 320^{0}C and the literature value of 300^{0}C is likely due to our measurement error.) No pattern was observed during the heating process. These patterns vanished when the sample was reheated above 320 ^{0}C, and new patterns developed once more after cooling back down. It was

also observed that patterns appeared to their full extent within seconds when the temperature was lowered below 320 ^{0}C, the rate of temperature change had no significant effect on this. However, these patterns took a much longer time to disappear, roughly 10 minutes, varying according to the size of the clusters and the rate of temperature change. This observation helps us to further understand the pattern growth process. The observed stable patterns after cooling below 320 ^{0}C are most likely due to the immobility of silver, or the" solidification of pattern". This cooling process caused some shrinking of the branches of the cluster, which helps us to explain why some branches of the cluster are isolated from each other as observed in Fig. 3.4.

It is of interest to understand under what condition the fractal structures grow. It was found that there is some general correlation between the growth of fractal patterns and physical or chemical transitions in the pattern formation in thin solid films system. For example, dendritic structures are formed on a superconducting $BaPb_{0.7}Bi_{0.3}O_3$ film annealed with lead oxide PbO_2, and are not formed when the film is annealed with Pb_3O_4 or PbO (Hidaka *et al* 1983). In annealed amorphous $GeSe_2$ films (Radnoczi *et al* 1987) and ion irradiated Ni - Zr films (Huang *et al* 1988) fractal patterns were formed during amorphous-crystal transitions. In our experiment the pattern appearance and disappearance seem to be associated with the oxidation of surface silver and the decomposition of surface silver oxide at around the decomposition temperature of silver oxide. It was found that the no pattern was observed if the sample was placed in nitrogen or argon gas instead of air during heating and cooling, thus inhibiting the oxidation of silver.

For studying the fractal pattern growth on the thin solid film, there are some features considerably different from other experiments: metal electrodeposition (Matsushita *et al* 1984), dielectric breakdown (Niemeyer *et al* 1984) and viscous fingering (Daccord *et al* 1986a, 1986b). Long-range bulk diffusion is hard to realize in thin solid films. Thus it is reasonable to believe that silver diffusion mostly occurs on the surface. It was interesting to find that our patterns can be removed by wiping with tissue paper and washing with distilled water which left no silver on the SnO_2 surface. This was confirmed by XRD and AEM measurements. After the fractal pattern was removed from the SnO_2 film surface, the XRD spectrum and AES data showed no evidence of silver composition.

Chapter 4

Universal Properties of Fractals

4.1 Fractal dimension

Both theorists and experimentalists are not only interested in the form of fractal-grown subjects as observed in nature and in laboratories, but also in their growth structures and properties. One parameter that characterizes a structure is the fractal dimension. The fractal dimension can be calculated by choosing the model which is suitable to describe a given experimental situation. The diffusion limited aggregation (DLA) model is considered widely applicable. By computer simulation, the fractal dimension D was calculated to be 1.70 ± 0.02 for two dimensional DLA cluster growth (Witten and Sander 1983). In this section, the results for the fractal dimension obtained from our experimental data will be presented.

First, an image of a fractal cluster was transformed into a digitized figure for numerical analysis. Figure 4. 1(a) and (b) show the initial real fractal image and its digitized figure with a total of 4250 pixels in a 200 X 200 matrix. Each pixel in the digitized one represents a gray level larger than the average intensity (i. e. the black area in a rectangle or square is larger than 50%).

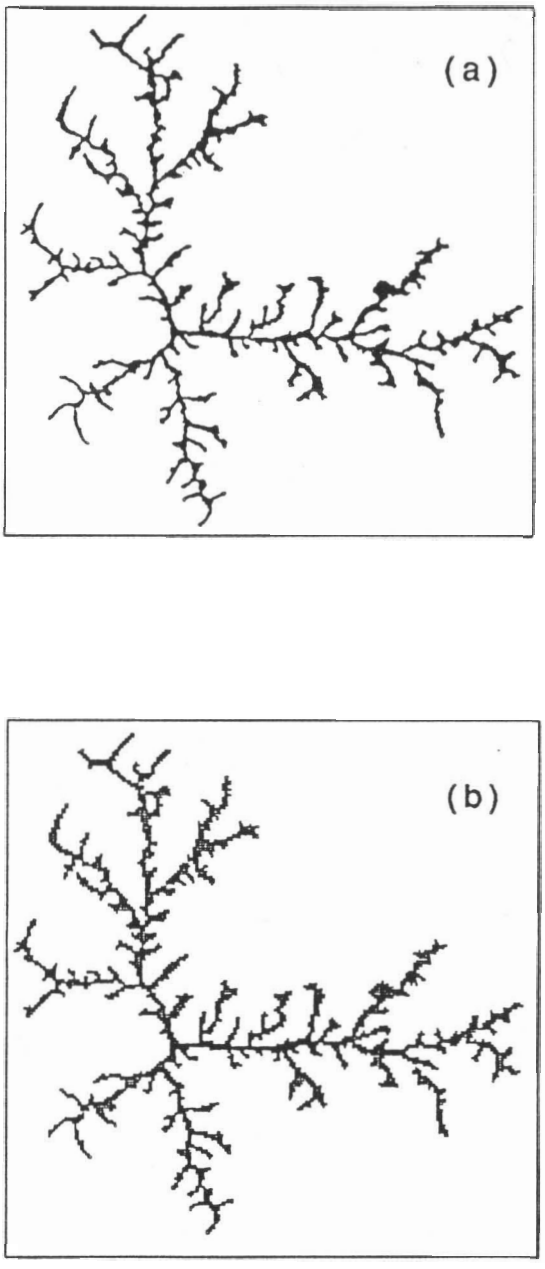

Figure 4.1 (a) Photograph of typical self-similar cluster at a magnification of 150X, (b) digitized image of (a) with a total of 4250 pixels.

A pixel, as distinguished from a particle, may contain thousands of Ag atoms. In a cluster, the coordinate of the ith pixel is defined as $\underline{r}_i = \underline{r}(x_i, y_i)$ as shown in Fig. 4.2(a), and the center of mass of the cluster is obtained from:

$$\underline{r}_c = \frac{1}{N}\sum \underline{r}_i , \qquad |r_c| = \sqrt{x_c^2 + y_c^2},$$

where $\underline{x}_c = \frac{1}{N}\sum \underline{x}_i$, $\underline{y}_c = \frac{1}{N}\sum \underline{y}_i$, and N is a total number of pixels in the cluster. The number of pixels inside a circle of radius r from the center of mass of the cluster and the radius itself follows a power law behavior with an noninteger exponent D, which is defined to be the fractal dimension: $N(r) \sim r^D$. The fractal dimension D, extracted from plotting N as a function of r in Fig. 4.2(b), is obtained to be D = 1.71 for the self-similar cluster in Fig. 4.1, which is in excellent agreement with the theoretical value of 1.70 for the DLA cluster growth (Witten and Sander 1981, 1983). Figure 4.3(a) shows a digitized image of a tree-like cluster grown at the edge of the contacts. The fractal dimension for this structure is calculated to be 1.49. The value of the fractal dimension for this cluster is expectedly low, since the cluster includes an apparently non-fractal branch in the lower part of the tree as shown outside the box in Fig. 4.3(a). If this portion is discarded in the calculation, the fractal dimension D is again obtained to be 1.70 from Fig. 4.3(b), consistent with the theoretical value. An average fractal dimension was obtained, from the most linear part of the curves, to be 1.69 ± 0.03. Figure 4.4 shows the radius vs. the number of pixels for several samples. We therefore conclude that the cluster-growth process in our experiment is basically an aggregation process which

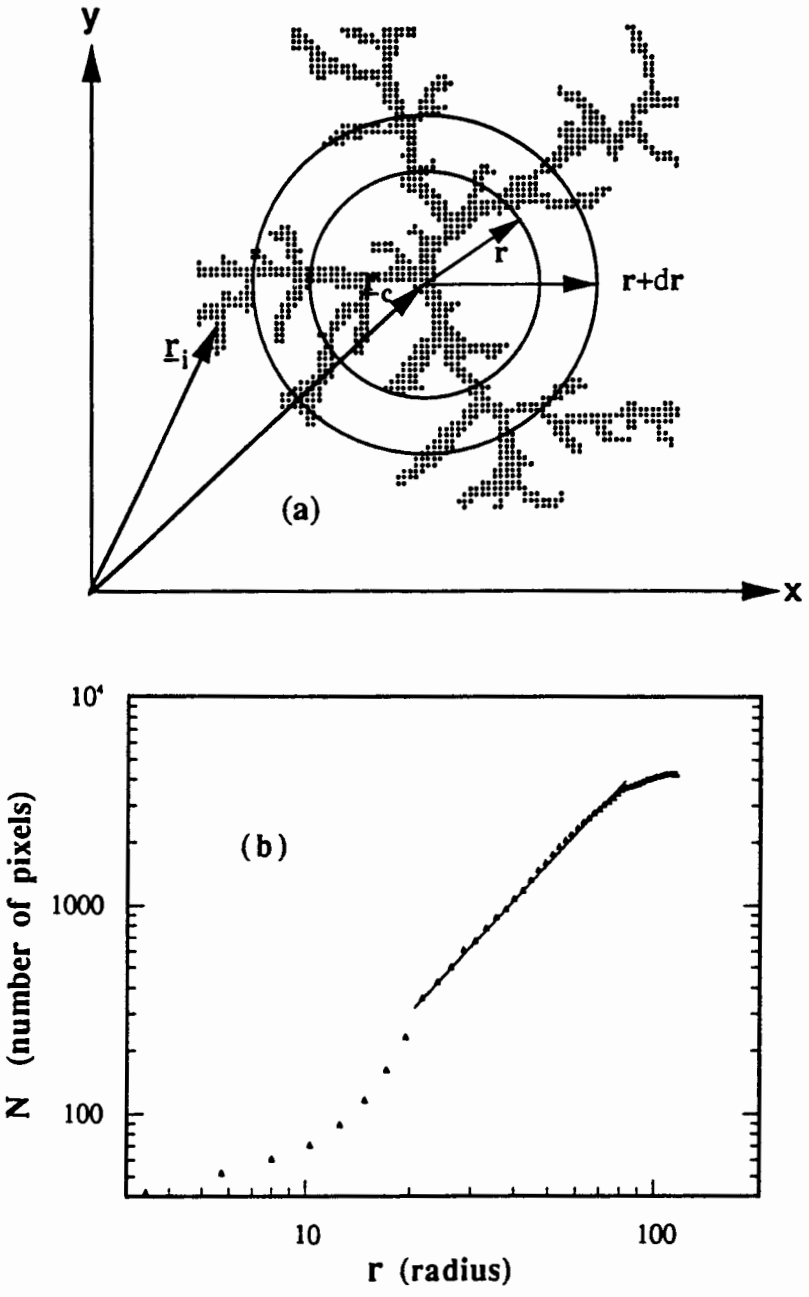

Figure 4.2 (a) Schematic diagram showing the ith pixel coordinate and the radius r from the center of mass of the cluster, (b) radius vs. the number of pixels for the cluster in Fig. 4.1. The fractal dimension D = 1.71 is obtained from the linear part of the curve.

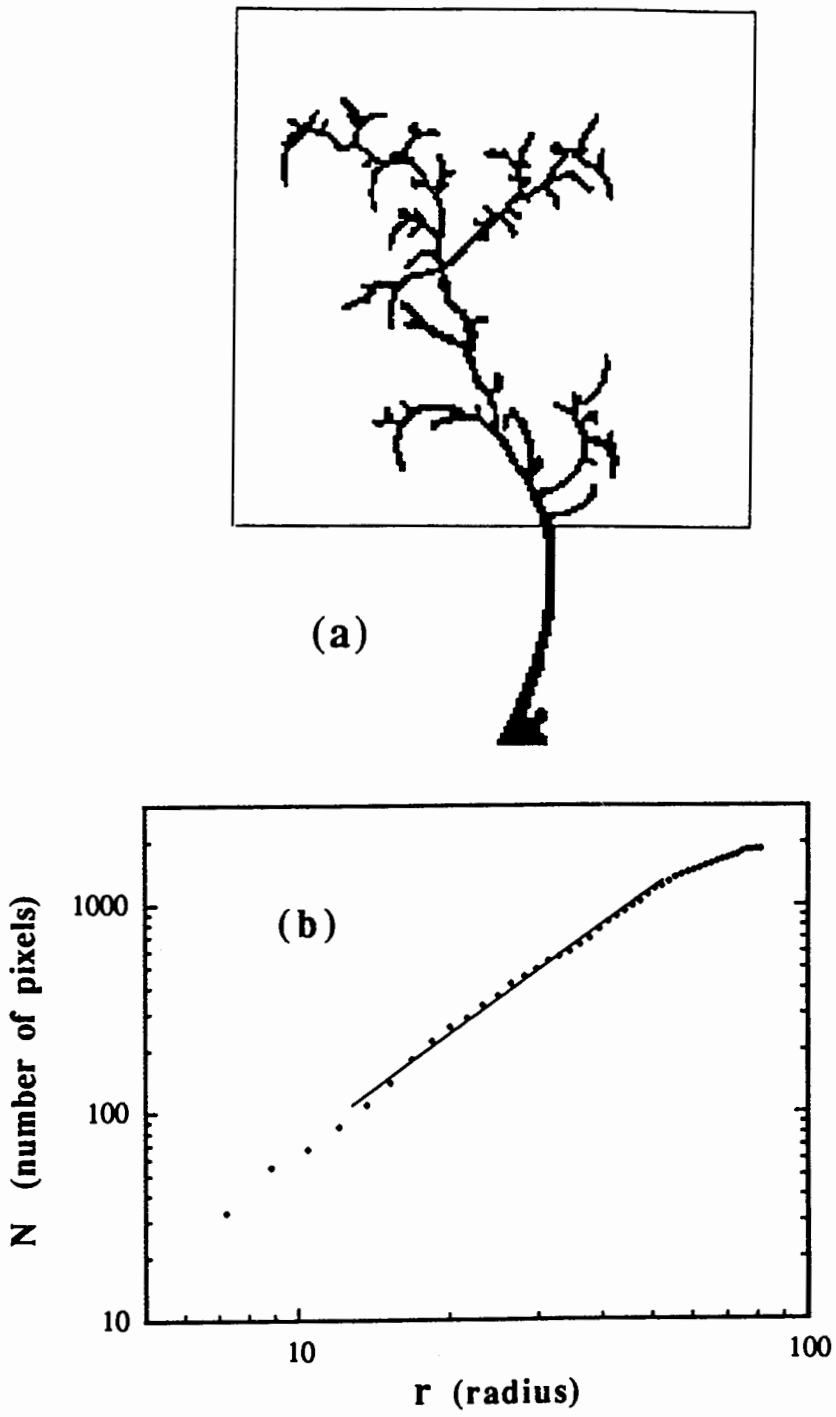

Figure 4.3 (a) Digitized image of tree-like cluster growth at the edge of the contact with a total of 2246 pixels, (b) radius vs. the number of pixel for the cluster shown inside the box in (a). The fractal dimension D = 1.70 is obtained from the linear part of the curve.

can be described theoretically by the diffusion-limited-aggregation model where random walk trajectories are assumed.

4.2 Scaling of the active zone

The active zone was first investigated theoretically by Plischke and Rácz (1984). By fitting the growth-site probability distribution with a simple Gaussian curve, they found that the mean radius r_N and width of the active zone σ_N with the number of particles N of the cluster scale as:

$$r_N \sim N^{\upsilon} \quad \text{and} \quad \sigma_N \sim N^{\upsilon'}$$

where the exponents $\upsilon' < \upsilon$ with $\upsilon = \frac{1}{D}$. By averaging over a large number of relatively small clusters ($N < 4000$), they found $\upsilon = 0.584 \pm 0.02$ and $\upsilon' = 0.48 \pm 0.01$, indicating the presence of two distinctly diverging lengths in the fractal growth process.

From our experiment, we calculated the probability density **P(r, N)dr** by finding the number of the pixels present in a shell of width **dr**, at a distance **r** from the center of mass of the cluster, as shown in Figure 4.2(a). Figure 4.5 shows **P(r, N)** as a function of **r** for the cluster in Fig. 4.1. The dashed line represents the Gaussian distribution function:

$$P(r, N) = \frac{1}{(2\pi)^{1/2}\sigma_N} \exp\{-\frac{(r-r_N)^2}{2\sigma_N^2}\}$$

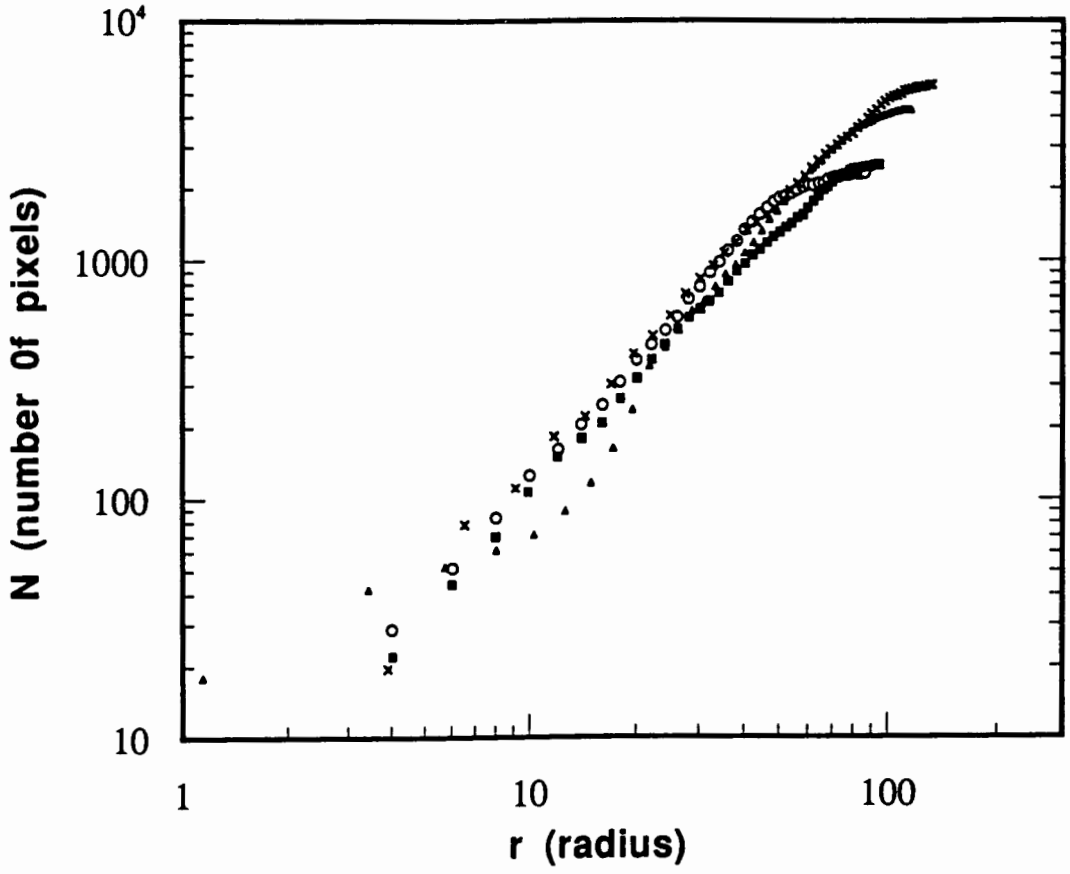

Figure 4.4 N number of pixels vs. radius for several samples, yielding an average of D = 1.69 ± 0.03 from the linear part of the curves.

with $r_N = 60$, and $\sigma_N = 27.5$; where r_N is the mean radius of the cluster and σ_N the standard deviation, which is defined as the width of the active zone. We see that the fitting to the experimental data is very good. As the shell width is broadened, the data points (symbol "o") move closer to the Gaussian fit as shown in Fig. 4.5 . Similar results were obtained for different sizes of clusters. Figure 4.6 presents the other example of a cluster size of N = 2300 with r_N = 38.5, and $\sigma_N = 18.3$. We, therefore, have confirmed that the active zone of the cluster can be described by a Gaussian probability distribution function, which is characterized by two parameters, r_N and σ_N. For different sizes of clusters found in our experiment, we calculated r_N and σ_N for each size. Clearly, r_N and σ_N are functions of N. By plotting the double-logarithm of r_N and σ_N shown in Fig. 4.7, and fitting the data points by the least-squares method (Daneil and Wood 1967), we found a power-law behavior, as predicted theoretically by Plischke and Rácz (1984):

$$r_N \sim N^{\upsilon} \quad \text{and} \quad \sigma_N \sim N^{\upsilon'}$$

where $\upsilon = 0.607 \pm 0.013$ and $\upsilon' = 0.512 \pm 0.026$ in agreement with theoretical values of $\upsilon = 0.584 \pm 0.02$ and $\upsilon' = 0.48 \pm 0.01$ calculated from Monte Carlo simulations. Detailed discussions of the two lengths r_N and σ_N were made in the papers by Plischke and Rácz (1984, 1985). The r_N describes the cluster expansion as the particles (pixels in our case) are added to the growing cluster. The υ is related to the fractal dimension D, with $\upsilon = \frac{1}{D}$. This is confirmed by also plotting the radius of gyration $R_g(N) \sim N^{1/D}$ which is in parallel to the r_N curve. Clearly, the mean radius r_N scales as the radius of

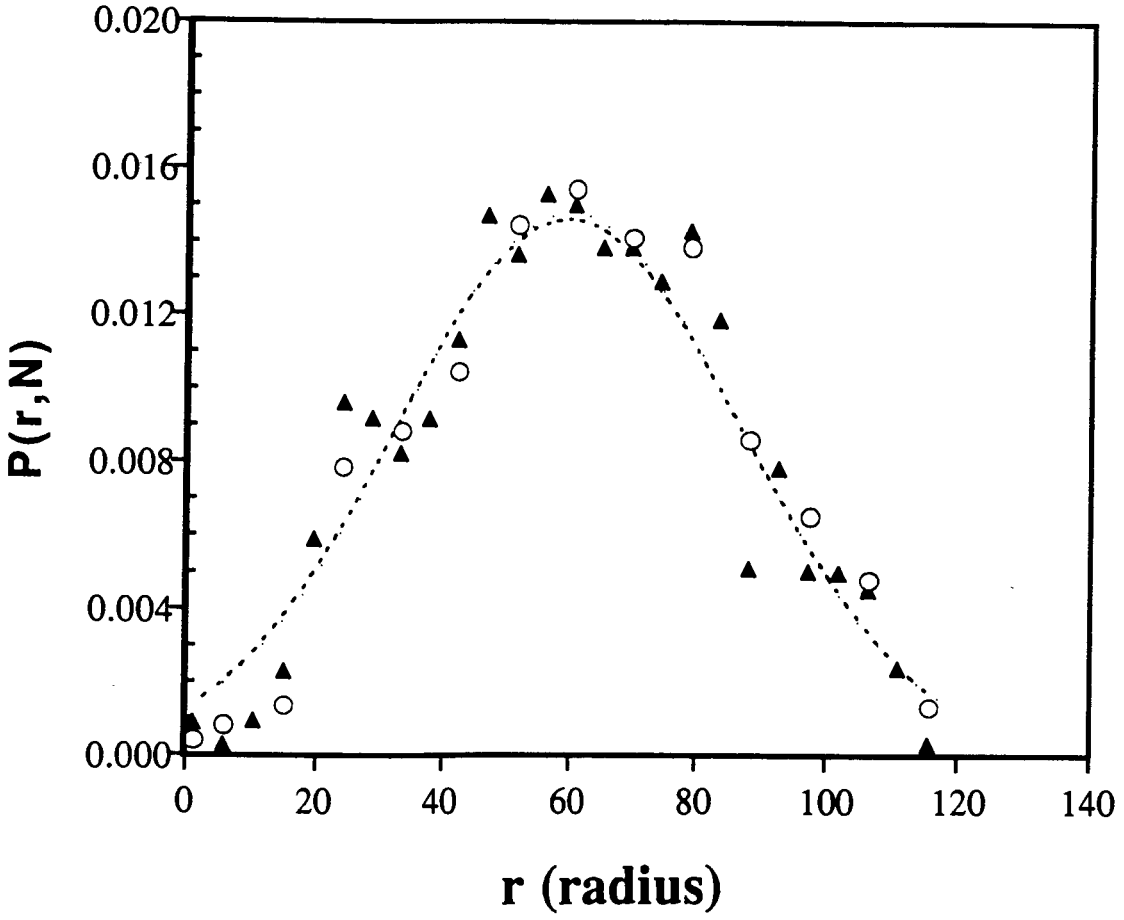

Figure 4.5 Probability of pixels present at a distance r from the center of mass of the cluster for Fig. 4.1. The dashed line is the Gaussian fit. As the shell width is broadened, the data points (O) move closer to the Gaussian fit.

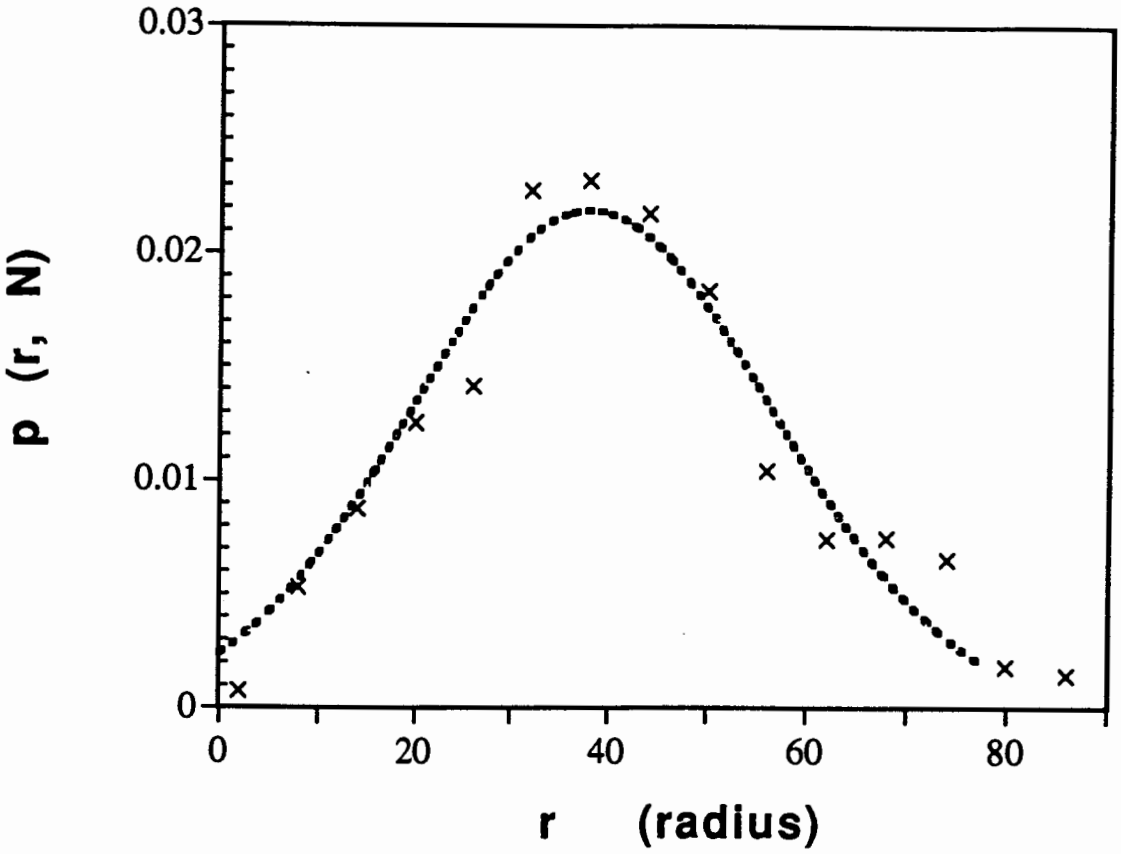

Figure 4.6 Probability of pixels present at a distance r from the center of mass of the cluster with a total of 2300 pixels. The dashed line is the Gaussian fit.

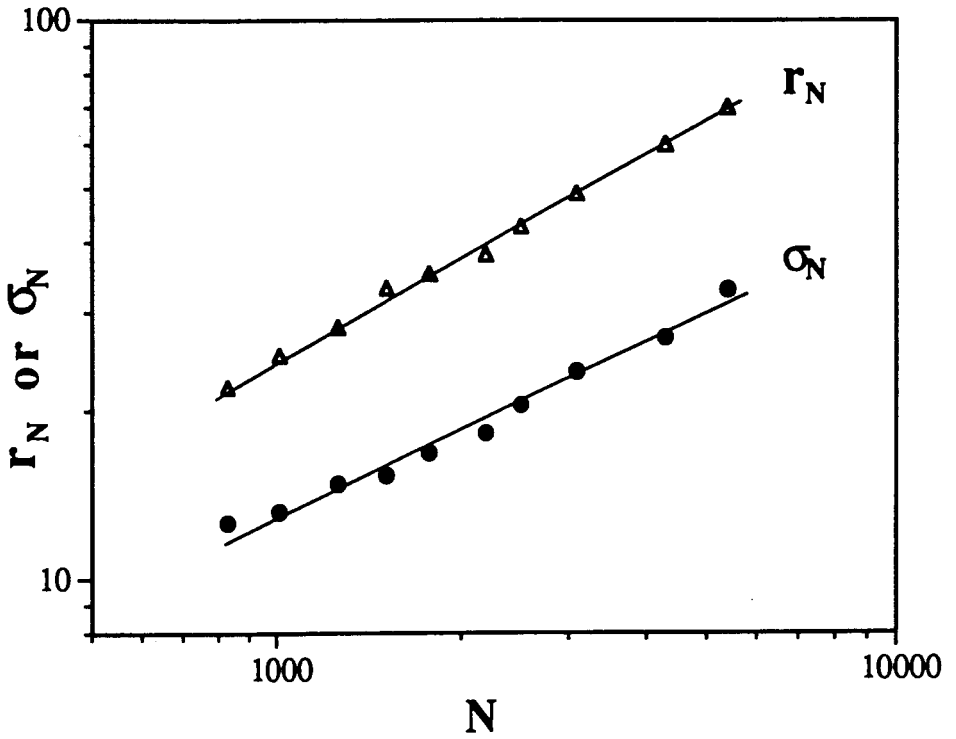

Figure 4.7 Exponents υ and υ' obtained from the double-logarithmic plot of the lengths r_N and σ_N

gyration. From finding $\upsilon' < \upsilon$, we can see that the growing clusters are characterized by two distinct lengths r_N and σ_N which scale differently. However, this conclusion may not hold in very large clusters. Meakin and Sander (1985) performed a similar calculation on larger clusters of up to 50000 particles, and found that υ' approaches υ as $N \rightarrow \infty$. Therefore, it appears that an extremely slow cross-over takes place in the surface structure of DLA clusters as they grow. Several other authors (Meakin and Vicsek 1985, Cates and Witten 1986, Halsey *et al* 1986a, 1986b, Amitrano *et al* 1986, Sempere *et al* 1993, Cafiero et al 1993) have also investigated the surface of growing diffusion-limited aggregates in more detailed and sophisticated ways.

Chapter 5

Summary to Part I

We obtained fractal patterns of silver growth on tin oxide films under appropriate operating conditions. The structures were studied by us in detail by SEM, AES and XRD. Some highlights of this work are summarized as following:

1. Patterns obtained from our experiments have both fractal and dense packed structures. The size of clusters varied from ten to hundreds of micrometers with a branch diameter of about 2 micrometers. According to Auger measurements, the aggregation cluster consists of silver, chlorine and small amounts of oxygen; no silver was found outside the patterns. It was suggested that the patterns were formed by Ag and AgCl with a thin layer of silver oxide on the surface.

2. It was noticed that metallic silver readily diffuses over polycrystalline SnO_2 surfaces above the oxide decomposition temperature of 320 ^{0}C. No pattern was observed during the heating process. Patterns suddenly appeared as the temperature dropped below 320 ^{0}C. These patterns vanished when the

sample was reheated above 320 ^{0}C, and new patterns developed after cooling back down. The cycling effect is believed to be associated with the decomposition of silver oxide and the oxidation of silver at around the decomposition temperature of 320 ^{0}C (Zhang and Colbow 1992).

3. The patterns were grown on the surface of the SnO_2 films. This is supported by the fact that patterns can be removed from the surface by wiping and washing. AES and XRD measurements showed that no silver composition on the SnO_2 surface was detected (Zhang *et al* 1993a).

4. The fractal dimension of our clusters was determined to be 1.69 ± 0.03 which is in excellent agreement with the theoretical value of 1.70 ± 0.02 predicted from the diffusion limited aggregation (DLA) cluster. We concluded that the cluster growth process in our experiment is basically an aggregation process which can be described theoretically by the DLA model where random walk trajectories are assumed (Zhang *et al* 1993b).

5. We also studied scaling of the active zone of the growth cluster and confirmed that the active zone of the cluster can be described by a Gaussian probability distribution function which is characterized by two distinctly diverging lengths r_N and σ_N, governed by exponents υ and υ' with power-law behaviors: $r_N \sim N^{\upsilon}$ and $\sigma_N \sim N^{\upsilon'}$, respectively. These two exponents for our clusters were found to be $\upsilon = 0.607 \pm 0.013$ and $\upsilon' = 0.512 \pm 0.026$, in good agreement with theoretical values of $\upsilon = 0.584 \pm 0.02$ and $\upsilon' = 0.48 \pm 0.01$ calculated by Plischke and Rácz (Zhang *et al* 1993b).

It is not clear at this point how the silver diffuses over the SnO_2 surface, if

for example the grain boundaries or the bulk are involved. Also there is not enough evidence to support the explanation of the mechanism of pattern growth on the SnO_2 film surface . Therefore, some further experiments may be necessary in the future:

1. It will be interesting to study the diffusion mechanism. This can be partly done by measuring the diffusion coefficient and drift diffusion rate as a function of temperature, surface preparations (or properties) and external voltage. Fick' diffusion equation or a variant thereof can be used to analyze the data.

2. The type of pattern and the rate of diffusion could be examined under AC bias, instead of DC bias, as a function of frequency and magnitude. The changes caused by different electric field configurations (eg. coaxial, points charges and parallel plates etc.) might be useful to trace out field lines.

3. Other surfaces besides tin oxide and other metals besides silver can be tried.

Part II

Ag-SnO_2 Thin Film Gas Sensors

Chapter 6

Introduction to Gas Sensors

Sensors are types of devices which can be used to measure universal physical parameter such as pressure, temperature and electrical properties. The recent concern over environmental pollution and over a need to monitor hazardous gases has stimulated substantial research and development in the field of gas sensors (Madou and Morrison 1989, Azad *et al* 1992, etc.). Semiconductor gas sensors based on SnO_2, ZnO and other metal oxides (McAleer *et al* 1988, Kohl 1989, Takayama and Fujitsu 1989) are considered to be most prominent among these gas sensors; they have been studied most extensively and are currently manufactured commercially in large quantities. Although these semiconductor sensors have shortcomings of reproducibility, stability and selectivity, they are simple and inexpensive. It is well known that the characteristics of these sensors can be significantly improved by addition of small additives (Yamazoe *et al* 1983, Gautheron *et al* 1993). However, the sensitization mechanism for these additives is not been well understood so far.

6.1 Preparation techniques

The semiconductor gas sensors can be prepared from sintered powder (Matsuura and Takahata 1991, Tamaki *et al* 1992, Xu *et al* 1991) or from thin/thick films (Sberveglieri *et al* 1991, 1993, Harkoma-Mattila *et al* 1992).

The sintered powder, an original method of preparing a semiconductor SnO_2 gas sensors, was introduced by Taguchi (1971). Generally, the SnO_2 powder was prepared by neutralizing a cold solution of $SnCl_4$ with an aqueous ammonia solution. The resulting precipitate of stannic acid was dried and calcined at a prescribed temperature (for example 400 ^{0}C) in air. Then the SnO_2 was impregnated with palladium chloride, calcined again at a higher temperature (550 ~ 600 ^{0}C) in air and then ground. The SnO_2 powder was admixed with alumina or other additives and formed into a paste by addition of a small amount of water. SnO_2 powder-based sensors, as shown in Fig. 6.1, were fabricated by applying this paste on a ceramic or alumina tube with Pt or Pd wire electrodes and with a heater within the tube, followed by drying and calcining. The other method of preparing the sintered powder sensor is screen printing (Oyaba *et al* 1982, Martinelli and Carotta 1993). Figure 6.1(b) shows this type of sensor with planar structure. Such structure may become more popular because cheaper batch processes are possible.

Semiconductor gas sensors can also be prepared from thin films. SnO_2 is the most successful material for film-based semiconductor sensors. For preparing these sensors, SnO_2 films were deposited onto substrates such as

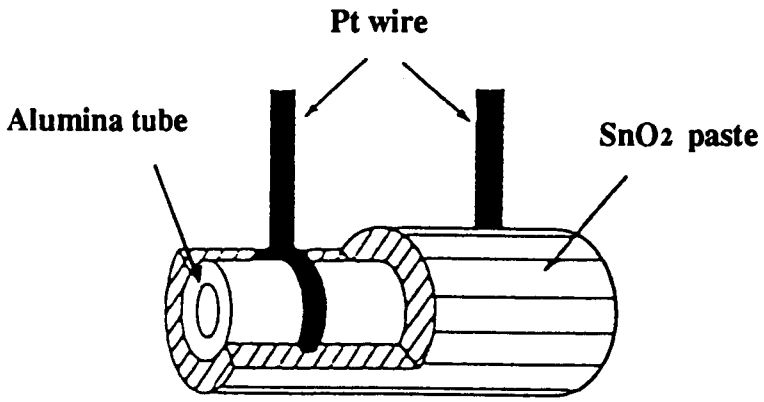

(a)

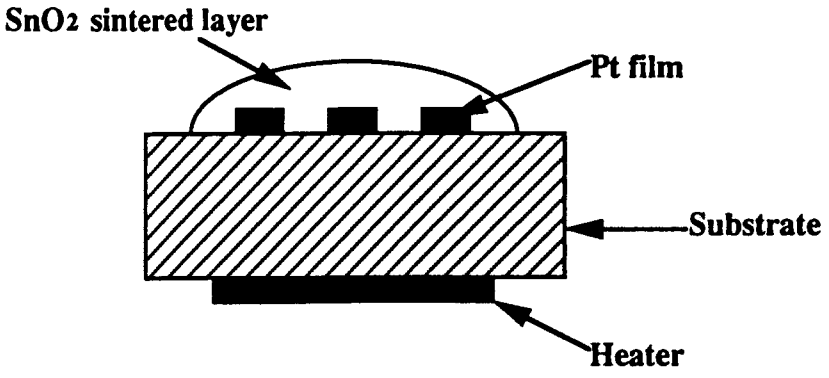

(b)

Figure 6.1 (a) structure of tube-type gas sensor. (b) Structure of planar-type sensor

alumina, ceramics or sapphire, by sputtering (Advani and Jordan 1980, Lantto and Mizsei 1991), evaporation (Sberveglier *et al* 1991) and chemical vapor deposition (Sberveglier *et al* 1993a). The structure of thin film sensors is similar to the planar structure of sintered powder sensors as illustrated in Fig. 6.1(b). The advantage of thin film sensors is that more automated production methods are available. In our research work, a spray pyrolysis method was used for preparing SnO_2 thin films, and most of the content in the following sections is related to the film-based SnO_2 semiconductor sensors.

6.2 Theoretical background

SnO_2 gas sensors are surface sensitive to the environmental gases by changing the surface electrical conductivity of the oxide semiconductor. It is necessary to provide background models describing the surface properties of semiconductor, especially in surface band structure and surface conductivity.

6.2.1 Surface band model

In a tin oxide semiconductor, impurities and oxygen vacancies usually act as donors to provide additional electrons to the conduction band. The density of electrons **n** in this n-type semiconductor can be expressed as:

$$\mathbf{n} = \mathbf{N_c} \exp\left[\frac{-(\mathbf{E_c} - \mathbf{E_F})}{\mathbf{kT}}\right] \qquad (6.1)$$

where N_c is the "effective density of states" near the edge of conduction band, E_c and E_F are the conduction band edge and the Fermi energy, respectively. The Fermi level E_F is shifted above mid-gap due to the extra electrons in the conduction band.

When the surface of the semiconductor is in contact with ambient gases, electrons will transfer to or from the semiconductor if their Fermi energies are different. Figure 6.2 shows the surface band structure for the n-type semiconductor. After the electrons have moved from the semiconductor to the surface state (acceptor in this case), a depletion layer is formed with the positively charged donor ions near the surface. By contrast, an accumulation layer will be formed if the surface state is a donor. These layers with uncompensated ions are called "space charge layers". Thus, the electron concentration near the semiconductor surface varies with the density and occupancy of surface states (acceptors or donors). In the gas sensor this density of surface states depends on surface reactions with ambient gases.

As seen in Fig. 6.2, the surface barrier arises from the band bending in the semiconductor surface. The value of the surface barrier V_s can be determined by the Schottky relation (Morrison 1982):

$$V_s = \frac{qN_iX_0^2}{2\varepsilon\varepsilon_0} \qquad (6.2)$$

where N_i and X_0 are the charge density in, and the thickness of , the space charge region, respectively.

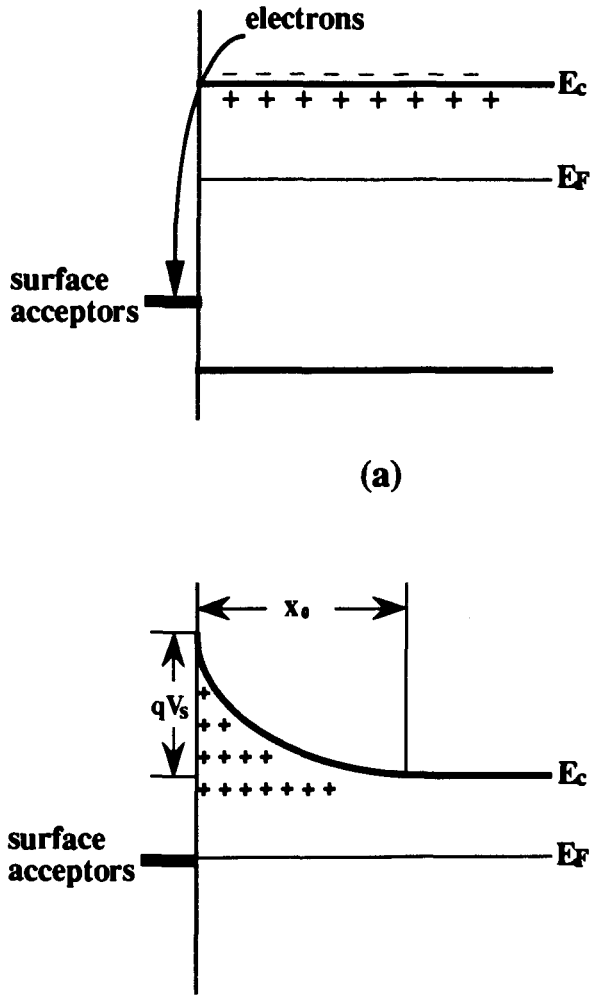

Figure 6.2 (a) Electrons from the conduction band are captured by surface states (acceptors). (b) The surface band bending leads a space charge layer on the surface (depletion layer in this case). V_s is the surface barrier, x_o is the thickness of the space charge layer.

The density of the electron n_s at the surface on a n-type semiconductor is given by the eqn. (6.1) involving qV_s:

$$n_s = N_c \exp\left[\frac{-(qV_s + E_c - E_F)}{kT}\right] \qquad (6.3a)$$

$$= N_D \exp\left[\frac{-(qV_s)}{kT}\right] \qquad (6.3b)$$

where N_D refers to the donor density in the bulk if the majority of carriers are electrons.

6.2.2 *Surface conductivity*

The presence of surface states at the semiconductor surface leads to important changes in the resistance or conductance of the semiconductor. Considering a thin film with the thickness t, width w and length l, the bulk conductance G for the n-type semiconductor is written as:

$$G = \frac{\sigma wt}{l} = \frac{N_D q \mu_n wt}{l} \qquad (6.4)$$

where σ is the bulk conductivity, q the electronic charge and μ_n the mobility of electrons.

Consequently, the surface conductance G_s is given by (Morrison 1982)

$$G_s = \frac{N_s q \mu_n w}{l} \qquad (6.5)$$

where N_s is the surface density of electrons extracted from the semiconductor.

From eqns. (6.4) and (6.5) we have:

$$\frac{G_s}{G} = \frac{N_s}{N_D t} \qquad (6.6)$$

N_s is about $10^{12}/cm^2$, and N_D is about $10^{17}/cm^3$ or more for most oxide semiconductors. It is clear that t must be 10^{-4} to 10^{-5} cm or less to permit a high sensitivity.

6.3 Sensing mechanism

For the semiconductor gas sensor, changes in the physical and chemical properties mostly occur at a solid/gas interface. Some investigations have been carried out on analysis of the influence of gas on the conductance by surface reactions (Morrison 1987a, Kohl 1989, Ohnishi *et al* 1993). It was found that the ionosorption plays an important role in the gas sensors. The adsorbates, acting as surface acceptors or donors, extract or reject electrons from or to the semiconductor, resulting in the conductance decrease or increase correspondingly. For the oxide semiconductors such as SnO_2, ionsorbed oxygen in the form of O^- or O_2^- is strongly adsorbed at the surface of

the semiconductor in the atmosphere of air. The adsorbed oxygen is a dominant contributor to the negatively charged surface state acting as a surface acceptor. The oxygen adsorption leads to a decrease of conductance in the semiconductor by consuming the electrons. In the atmosphere of reducing agents, the reaction of the reducing gases with adsorbed oxygen ions causes a decrease of the oxygen acceptors and an increase in conductance by restoring the electrons to the conductance band of the semiconductor.

These reactions can be expressed by some chemical equations. In the first reaction, the adsorption of oxygen consumes the electrons:

$$O_2 + e^- = O_2^- \qquad (6.7)$$

or

$$O_2 = 2O \qquad (6.8)$$

$$O + e^- = O^- \qquad (6.9)$$

The reaction of the reducing agents R with these adsorbed oxygens can be represented by reactions such as:

$$R + O_2^- \rightarrow RO_2 + e^- \qquad (6.10)$$

$$R + O^- \rightarrow RO + e^- \qquad (6.11)$$

The difference between the form of O^- and O_2^- has been studied by some investigators (Chon and Pajares 1969, Yamazoe *et al* 1979, Madou and Morrison 1989). O^- normally is more active than O_2^-. It was found that

adsorbed oxygen in form of O^- was dominant at a higher temperature (170 ^{0}C for ZnO, 150 ^{0}C for SnO_2). Madou and Morrison (1989) have also made a theoretical calculation on the relative concentration of O_2^- to O^- as a function of parameters such as temperature and partial oxygen pressure. They found that the concentration of O^- decreases as the oxygen pressure increases, but increases as the temperature increases. A useful formula is stated as:

$$\frac{[O_2^-]}{[O^-]} \propto P_{O_2}^{1/2} \, Exp[-\frac{(E_{O_2} - E_O - \Delta E/2)}{kT}] \qquad (6.12)$$

where $\mathbf{P}_{O_2}$ is the oxygen pressure. $\mathbf{E}_{O_2}$ and $\mathbf{E}_O$ are the energy levels of the oxygen molecule and oxygen atom, respectively. $\Delta\mathbf{E}$ is the free-energy change associated with the reaction in the eqn. (6.8). The double charged oxygen ion O^{2-} is not in general to be expected for adsorbed species, because such a high charge on the ion may lead to instability. However, Ohnishi *et al* (1993) considered that the oxygen adsorbates are in the form of O^{2-} at the very high temperature of 400 to 500 ^{0}C for a thin SnO_2 film, which was suggested from the Electron Spin Resonance (ESR) measurements.

Not only the adsorbed oxygen, but also surface lattice oxygen, especially in the TiO_2 film surface (Kirner *et al* 1990), can act as a surface state. The lattice oxygen was formed from oxygen vacancy by the reaction:

$$V_{\ddot{o}} + 2e^- + \frac{1}{2}O_2 = O_0^x \qquad (6.13)$$

where $V_{\ddot{o}}$ denotes the oxygen vacancy and O_0^x the lattice oxygen.

The influence of gas concentration or partial gas pressure on the conductance of the semiconductor was investigated mostly. It was found that the conductivity σ and the gas pressure **P** have a power law behavior of the form

$$\sigma \propto P^{\beta} \qquad (6.14)$$

The sign and the value of β depend on types of gases. For example β was determined to be 1/3 for CH_4 (Geloven *et al* 1989), 0.3 ~ 0.8 for CO (McAleer *et al* 1987), and - 0.5 for O_2 (Ohnishi *et al* 1993).

6.4 Catalytic additives

The addition of catalysts into the gas sensors can enhance the sensor performances (sensitivity, recovery and selectivity). The use of noble metals such as Pt, Pd is currently dominant in both the sintered powder gas sensors and thin film sensors. Depending on the added catalyst and the preparation condition, the sensor characteristics were improved mostly by either increasing the sensitivity or impacting the selectivity or speeding up the reaction. Advani *et al* (1981/82) successfully used the gold diffusion into SnO_2 film to reduce the recovery time by a factor of four to six. This was explained due to fact that the gold saturated the grain boundaries so that the grain boundaries were insensitive to the gaseous ambient, and the surface

reactions were now dominant. Most other investigations were carried out to improve the sensitivity and selectivity. Sulz *et al* (1993) found that the H_2 response was strongly improved by adding Pt into SnO_2 film. Gautheron *et al* (1993) claim that Pd incorporation into the SnO_2 thin film significantly improves the sensitivity and selectivity to CO. In some cases, use of Cd, Li, Cr doped SnO_2 also improved the sensor performances. It was reported that the Cd-doped SnO_2 thin film (Sberveglieri *et al* 1991) results in high sensitivity and selectivity to NO_x, while Li-doping (Sberveglieri *et al* 1993b) improves the sensor selectivity to O_2. They also found that the crystalline average size was reduced by the presence of dopants. The reason for this is still not clear. Dopant is distinguished from catalyst by the fact that the electrical and/or structural properties of the semiconductor can be changed by doping, but not by adding catalyst. Recently the combination of catalyst and dopant (Low *et al* 1992) or an alloy of noble metals has been employed. The role of these additives has been reviewed by some authors (Madou and Morrison 1989, Kohl 1990, Azad *et al* 1992).

To interpret the promotional role of additives, two possible sensitization mechanisms, chemical and electronic, were proposed (Yamazoe *et al* 1983, Matsushima *et al* 1988). The chemical sensitization is mediated by a spillover effect. Hydrogen spillover has been extensively studied, but oxygen, and even CO, can also "spill over" from the catalyst metal. The spillover is a process where the ambient gas in the form of molecules is adsorbed on the surface of the catalyst metal to be dissociated; then the atoms spill over the surface of the semiconductor and thus react with the adsorbed or surface oxygen, resulting in an increase in the surface conductivity of the n-type semiconductor.

Surface reactions can be accelerated by the presence of dispersed metallic catalysts. By contrast, the electronic sensitization is mediated by the direct exchange of electrons between the semiconductor and metal additives. A change in the oxidation state of the additives, by electron donors or acceptors to or from the semiconductor upon contact with the objective gases or air cause a conductivity change in the semiconductor. The electronic sensitization is expected to be the dominant mechanism when oxide catalysts are used on the sensor. When metallic catalysts are used, the sensitization may be electronic or chemical.

Although two sensitizations were suggested, the sensing mechanism in actual gas sensors is far from being well understood due to insufficient investigations. It is also very difficult to compare results obtained from different laboratories because different preparation methods and different additives were used.

6.5 Application of sensors

Presently, there are different types gas sensors in substantial use commercially. These are mostly based on the semiconductor materials SnO_2, ZnO, WO_3, TiO_2 and In_2O_3, for the detections of a variety of gases such as H_2, CO, CO_2, H_2O, NH_3, SO_x, NO_x, CH_4, H_2S etc.. Although these semiconductor gas sensors owe their popularity to their small size, simple operation, high sensitivity and low cost, they have problems of selectivity, stability and reversibility. To improve the selectivity, some methods such as varying the catalyst as discussed in the section 6.4, adopting the filter, selecting the

operation temperature and using arrays of different sensors may be helpful. However, substantial research is now being carried out on the development of new materials and new fabrication techniques to improve these properties and to meet a need in monitoring and controlling domestic and industrial environments.

Besides the oxide semiconductor gas sensors, there are chemFET sensors and solid electrolyte sensors as recent developments. ChemFET sensors (Janata *et al* 1985, Madou and Morrison 1989) utilize the gate structure in Field-effect transistor (FET). In a FET one has a thin channel of conductance at the surface of the silicon, which is controlled by the voltage applied to a metal film (a gate) separated from the channel of conductance by a thin insulator (silicon oxide). It was found that if the metal film was removed from the FET and either adsorbed gases or ions from the ambient atmosphere or else liquid appeared at the surface of the gate, the effect was similar to applying a voltage at the gate (Bergveld 1970). One advantage in the FET sensors is that it is possible to use well-understood integrated circuit technology to produce multisensors in which arrays of sensor elements are incorporated onto one chip for multispecies detection. In solid electrolyte sensors (Madou and Morrison 1989, Azad *et al* 1992), the conductivity stems from mobile ions rather than electrons. Examples of solid electrolytes used in sensors are an O^{2-} conductor in yttria (Y_2O_3) stabilized zirconia (YSZ), a F^- conductor in LaF_3 and Ag^+ conductors in α–AgI, Ag_3Si etc.. Both, chemFET sensors and solid electrolyte sensors, can be used not only for detection of gas-phase species, but also for detection of liquid-phase species.

These chemical sensors, including semiconductor gas sensors, chemFET sensors and solid electrolyte sensors, have their current and projected applications in industrial control, environmental monitoring, and in working places such as mines, laboratories, hospitals, homes etc.. The major markets currently existing for the chemical sensors are the toxic and combustible gas sensor market, the automotive market, the medical market and the home market. The largest current use of sensors is in environmental monitoring and pollutant control in industry. The most common toxic and combustible gases monitored include H_2S, CO, HCl, CH_4, HC, H_2 and AsH_3. There are great potential applications for the chemical sensors in the medical market and the home market. The sensors used in medicine are mainly for blood and urine chemical analyses such as blood gases (O_2, CO), pH, Ca, Cl etc.. The other promising application of sensors is in home appliances and home automation systems to detect and control the humility, smoke, leaking gas, pressure, cooking condition etc..

Chapter 7

Materials and Measurements

7.1 Preparation of sensor element

The SnO_2 films

SnO_2 films were prepared on alumina or silica substrates by aerosol spray pyrolysis. The experimental details were described in section 2.1. The films used in the sensors were deposited at 270 ^{0}C to 320 ^{0}C.

After the deposition of SnO_2 film, the sample was cut into squares of side about 1 cm.

The silver clusters

A thin layer of silver (Ag) film was deposited onto the surface of SnO_2 samples by vacuum evaporation. A vacuum unit (Cha Industries), operating in $10^{-6} \sim 10^{-7}$ torr, was used to produce an uniform Ag film. The thickness of the metal films was estimated from the formula $\mathbf{d} = \frac{\rho}{\mathbf{R_s}}$, where ρ is the resistivity of Ag which is known to be 1.60 $\mu\Omega$·cm at 22 ^{0}C (Handbook of Chemistry and Physics), and $\mathbf{R_s}$ the sheet resistance of the Ag film which was measured by the two-points probe method. This thickness determination assumes that the metal film is uniform.

The sample of Ag/SnO_2/substrate was annealed at a temperature of about 400 ^0C to disperse the silver on the SnO_2 surface.

The electrode contacts

Electrode contacts were made from a conductive gold paste (Electron Microscope Science). The gold paste was painted on the desired area, followed by a curing procedure (heating for 30 min. at 80 ^0C). The structure of gas sensor element is shown in Fig. 7.1.

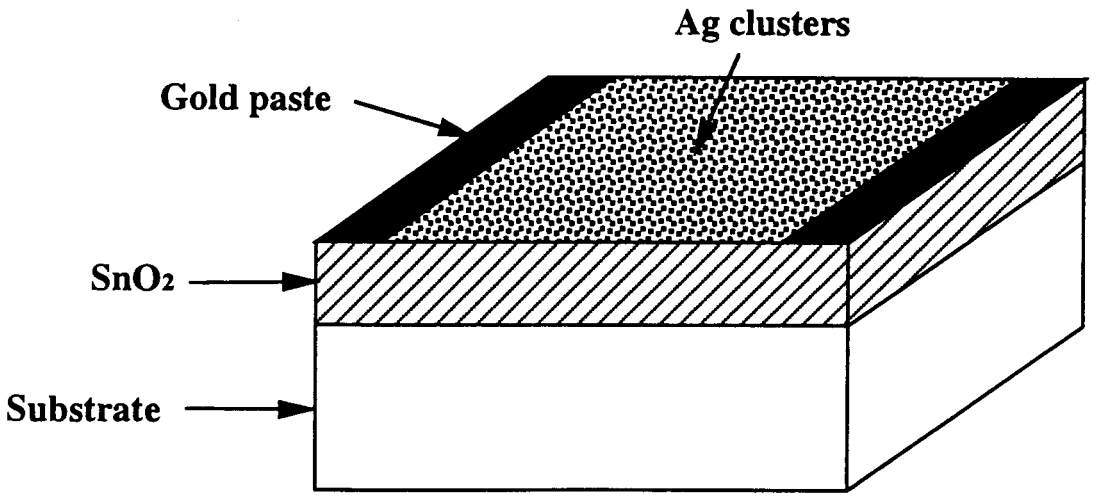

Figure 7.1 Schematic drawing of the $Ag\text{-}SnO_2$ thin film gas sensor element

7.2 Experimental arrangement for conductance measurement

The sensor element was inserted into a small furnace by a holder, which consists of a piece of quartz and two wires (gold or chromel) that acted as leads to attach to the electrodes of the sensor. The small furnace was placed inside a plexiglass box (approximate 30 liter) equipped with a built-in fan. The experimental set-up is shown in Fig. 7.2(a).

The signals of sensor electrical conductance and the operating temperature were sent to a PC computer through an A/D converter. The conductance and the temperature as a function of time were recorded graphically and stored in the computer. The block diagram of these measurements is illustrated in Fig. 7.2(b).

7.3 Sensitivity of sensors

The conductance **G** of the sensor is determined by knowing the shunt resistance **R**:

$$G = \frac{V_R}{V_0 - V_R}\frac{1}{R} \qquad (7.1)$$

where V_R is the potential difference across the shunt resistance and V_0 the potential difference across both the sensor element and the shunt resistance.

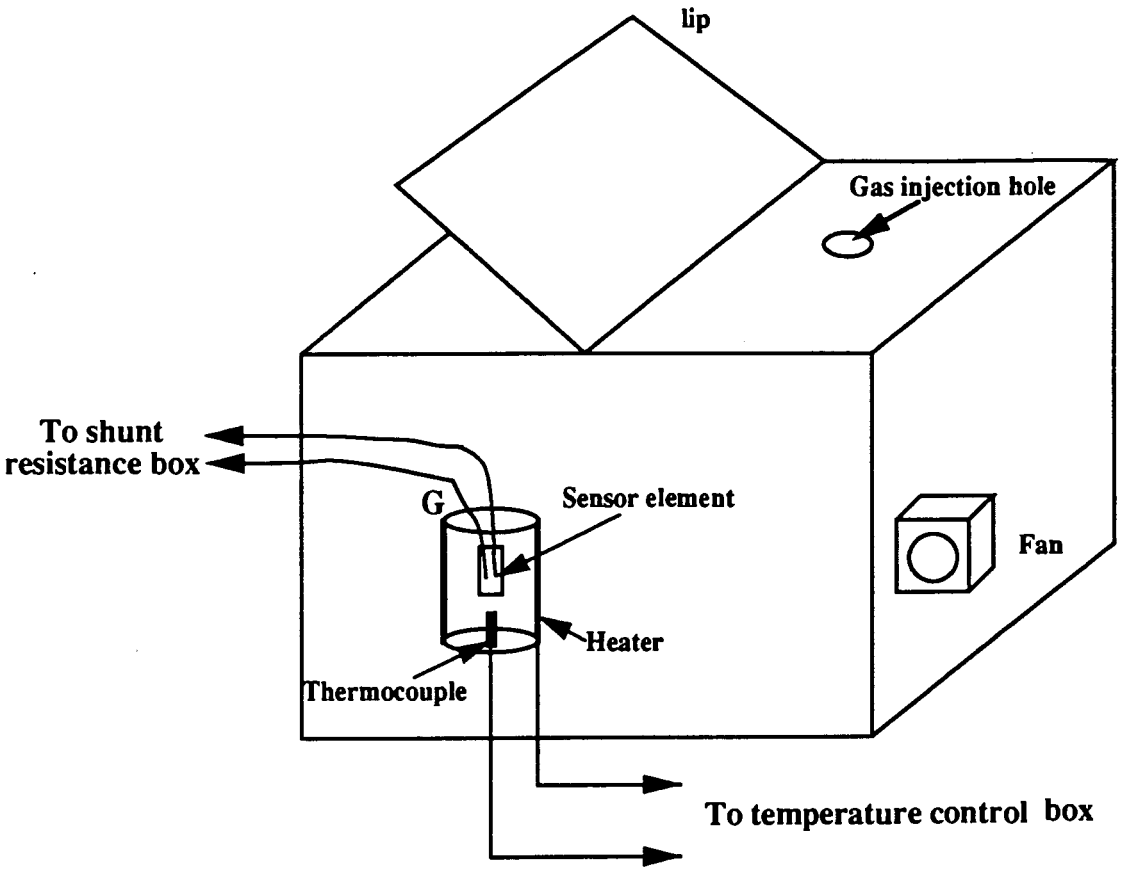

Figure 7.2(a) Experimental set-up for gas detection

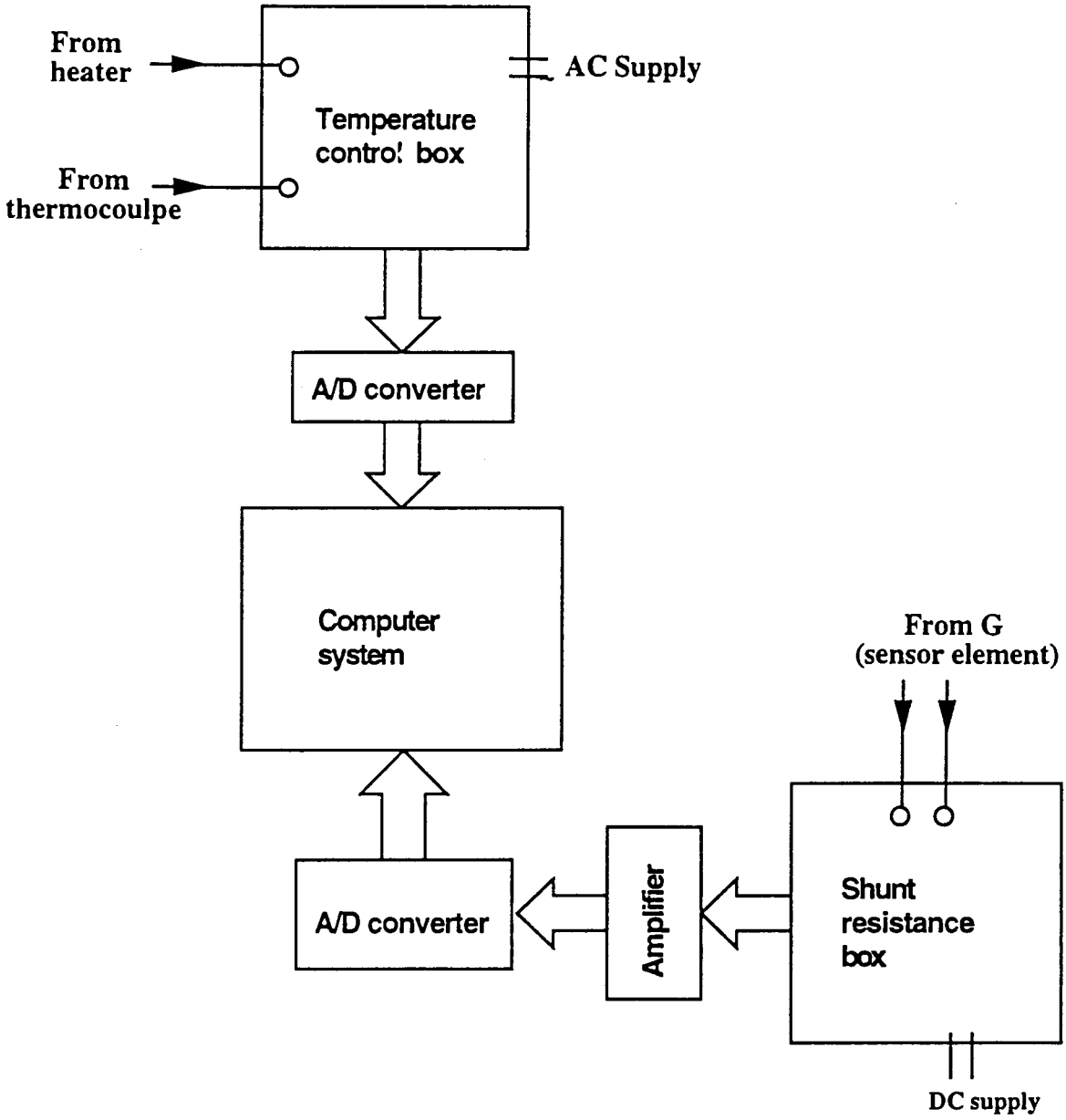

Figure 7.2(b) Block diagram showing the conductance and the temperature measurements

The sensitivity of the sensor for the reducing gases is determined as:

$$S = \frac{(G_{gas} - G_{air})}{G_{air}} \qquad (7.2)$$

where G_{air} and G_{gas} are the conductance of the sensor in air and the in tested gas respectively.

Since only relative conductance changes are of interest and G_{gas} is much much larger than G_{air}, the measurement becomes independent of R and the sensitivity can be rewritten as:

$$S \approx \frac{G_{gas}}{G_{air}} = \frac{V_{R(gas)}/(V_0 - V_{R(gas)})}{V_{R(air)}/(V_0 - V_{R(air)})} \qquad (7.3)$$

The gas concentration, expressed in general by ppm, was determined by knowing a volume of the box in Fig. 7.2(a) and the amount of gas injected into the box. The built-in fan was used to distribute the gas quickly and uniformly through the volume of the box. A lid on the top of the box could be opened to release the gas from the box.

Other experiments related to this part such as SEM AES and XRD have been described in the Chapter 2.

Chapter 8

Ag-added SnO_2 Thin film Gas Sensors

8.1 Surface observation of Ag clusters on SnO_2 films

The dispersions of silver clusters on the SnO_2 films were observed by microscope and SEM measurements. Figure 8.1(a) shows the photographic image of Ag clusters obtained by evaporating a silver layer of about 200 Å onto the SnO_2 surface, followed by heating at 400 ^{0}C for one and a half hour. AES measurements revealed that the gray area in the photograph is silver and the white area SnO_2. This type of pattern looks like a percolation phenomenon (Deutsher *et al* 1983, Ding and Liu 1989b). A different morphology was obtained from a thinner silver layer of about 40 Å as shown in Figure 8.1(b). SEM analysis showed that the white area in this micrograph is silver and the black area SnO_2. One can see from Fig. 8.1(b) that the clusters are well distributed on the SnO_2 surface and quite uniform because of an appropriate thickness of Ag film used. This may be useful for Ag-added SnO_2 thin film gas sensors.

In order to provide further insight into these clusters, Auger scanning and XRD measurements were carried out. Figure 8.2 shows the Auger line

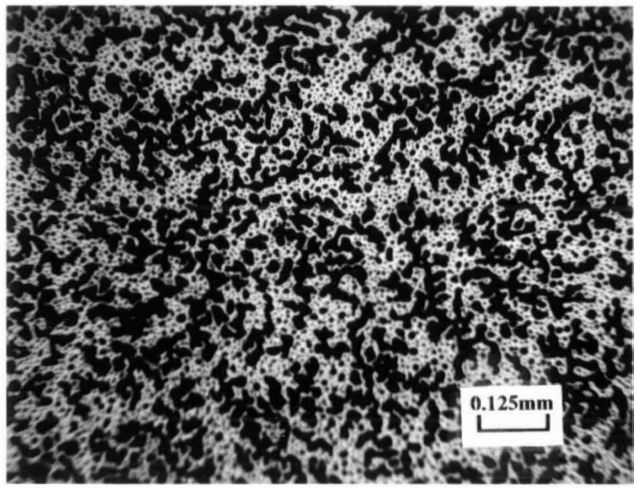

Figure 8.1(a)

Microscope photograph showing sliver clusters on the SnO_2 surface after an evaporated layer of Ag film (~200Å) was heated at 400° C for 1.5 hour.

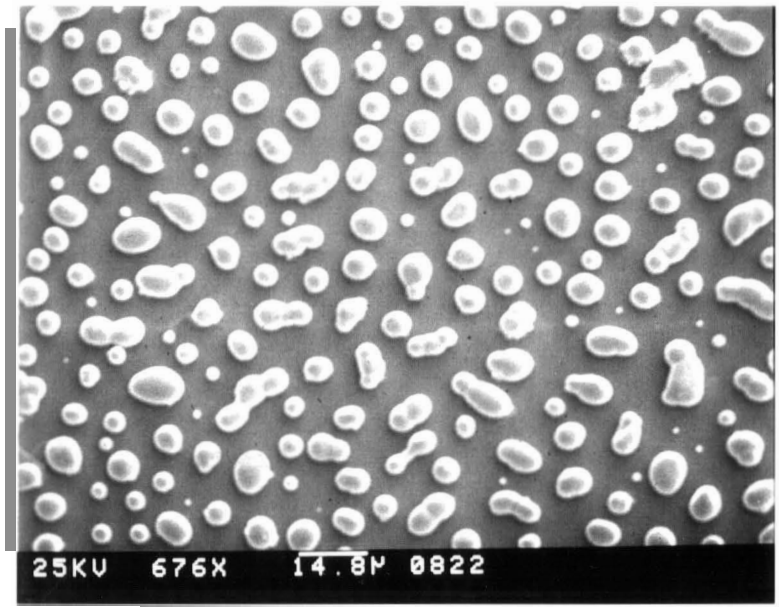

Figure 8.1 (b)

SEM micrograph showing surface morphology of silver clusters dispersed on the SnO_2 surface after a thinner layer of Ag (~40 Å) was heated for 1 hour.

scanning of Ag across the clusters for Fig. 8.1(b). The Ag clusters have sizes of 4 ~ 5 μm and are isolated from each other. Each cluster looks like an island on the SnO_2 surface. XRD measurements are presented in Figure 8.3. Figure 8.3(a) is the XRD spectrum for an evaporated Ag film on glass. A very strong peak Ag(111) observed in the XRD spectrum indicates that the Ag layer growth on the glass surface is predominantly oriented with Ag(111) plane parallel to the glass surface. Figure 8.3(b) shows the XRD spectrum for Ag clusters on the SnO_2 surface on a glass substrate. As found before, the as-prepared tin oxide films , deposited at 275 ~ 325 ^{0}C , have an amorphous-like structure. However, some weak XRD peaks of SnO_2 were observed in Fig. 8.3(b) after the sample was annealed at 400 ^{0}C for the dispersion of Ag clusters. This can be explained as phase transition from amorphous to polycrystalline during heat treatment, which has also been observed for SnO_2 by other authors (Fresart *et al* 1983, Das and Banerjee 1987). The other XRD peaks in Fig. 8.3(b) are mainly from a mixture of Ag and AgCl. According to AES and XRD measurements, it was suggested that the clusters are formed by Ag and AgCl with a thin layer of silver oxide on the surface.

8.2 Sensor performance

The sensor performance of SnO_2 thin film gas sensors was investigated. It was found that the sensitivity and the recovery of the sensors were improved by the addition of Ag on the SnO_2 surface (Zhang *et al* 1994). Figure 8.4(a) shows the conductance response to 200 ppm H_2 gas for an as-prepared SnO_2

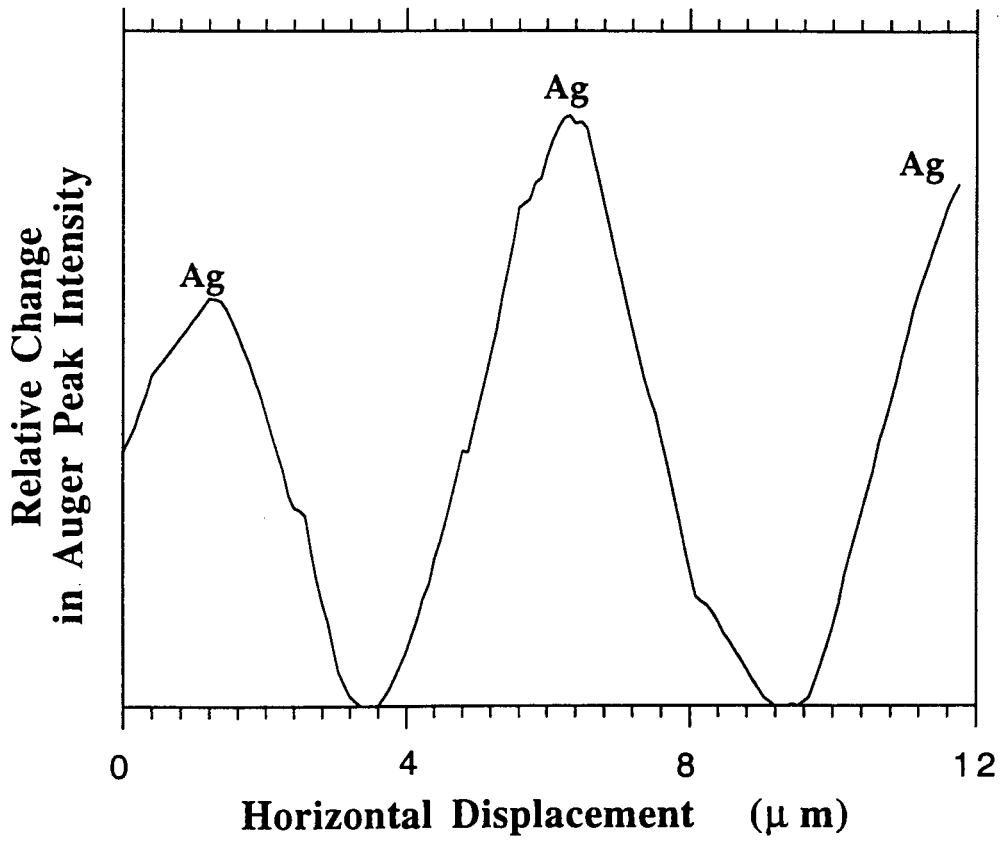

Figure 8.2 Auger line scanning of Ag across the clusters. The Ag is normalized with respect to the most intense of Ag signal.

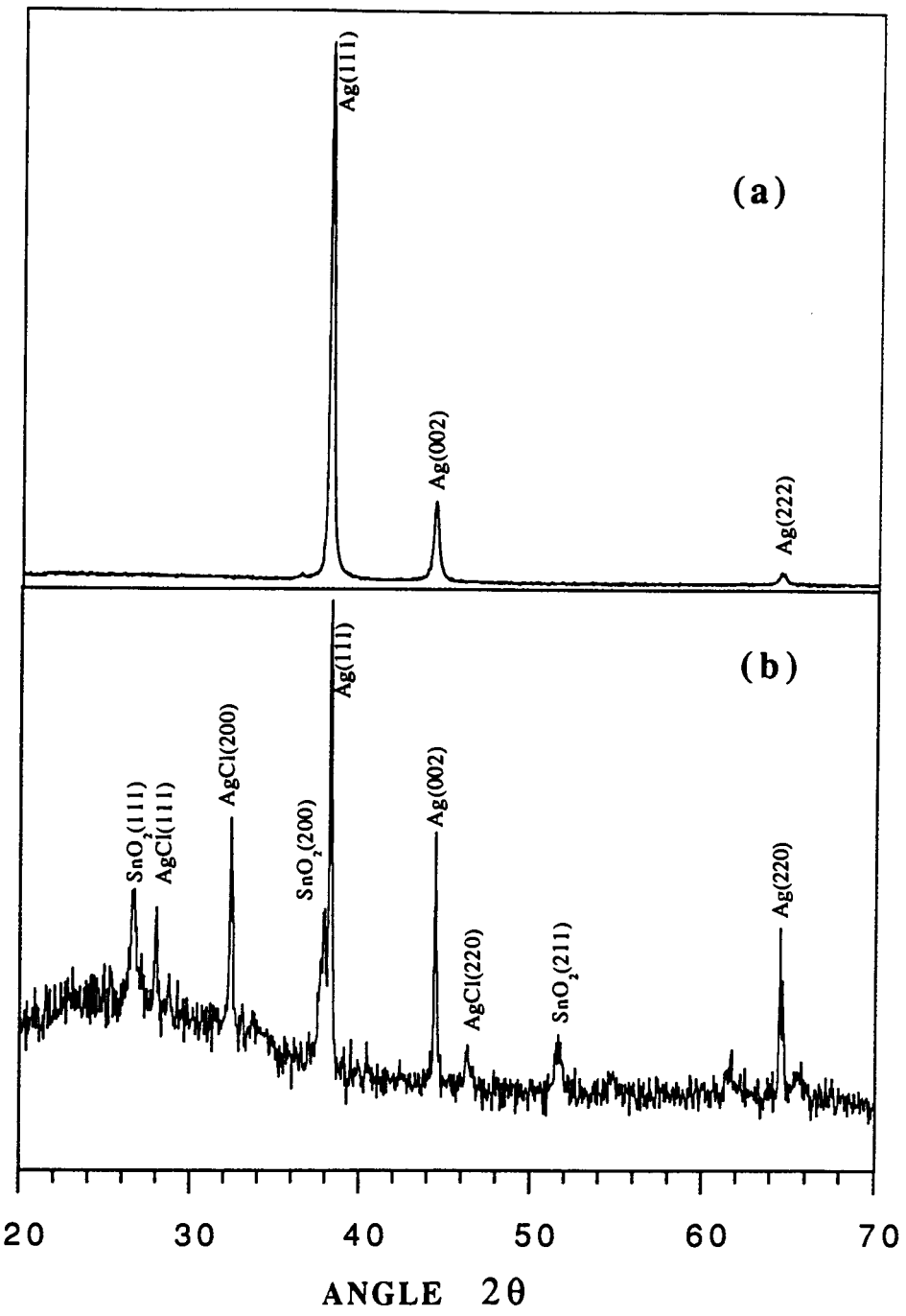

Figure 8.3 XRD spectra of (a) an evaporated Ag film on glass, (b) silver clusters on SnO_2 surface.

sensor, operated at a temperature of 275 ^{0}C. We can see that the sensitivity and recovery were quite poor. After silver additive to the SnO_2 film surface, the sensitivity and the recovery were much improved. Figure 8.4(b) presents an example with 50 Å thickness of Ag deposited onto the SnO_2 surface. The sensitivity increased by an order of magnitude. The response time and the recovery time were less than 30 seconds and 40 seconds respectively. The response time is defined as the time in which the conductance reaches 90% of the stable value and the recovery time is arbitrarily defined as the time required for the sample's conductance to reduce its stable value by 60%. The choice of 60% for the recovery time is dictated by a fact that samples need longer time to return to their original conductance values, even some of them could never recover (Advani *et al* 1981/1982).

8.2.1 Sensitivity

It was found that the sensitivity was quite dependent on the operation temperature of the sensor and the amount of Ag addition that influences the cluster details. Figure 8.5 shows the sensitivity response to 200 and 50 ppm H_2 respectively versus the operating temperature for a Ag-added (50 Å) SnO_2 thin film sensor. A maximum occurs at the temperature around 300 ^{0}C. The sensitivity or the conductance increase is caused by the desorption of the negatively charged surface oxygen in the presence of H_2. On the one hand, oxygen adsorption on the sensor surface in the form of O^- is more active and more dominant at higher temperature; on the other hand, O^- species could

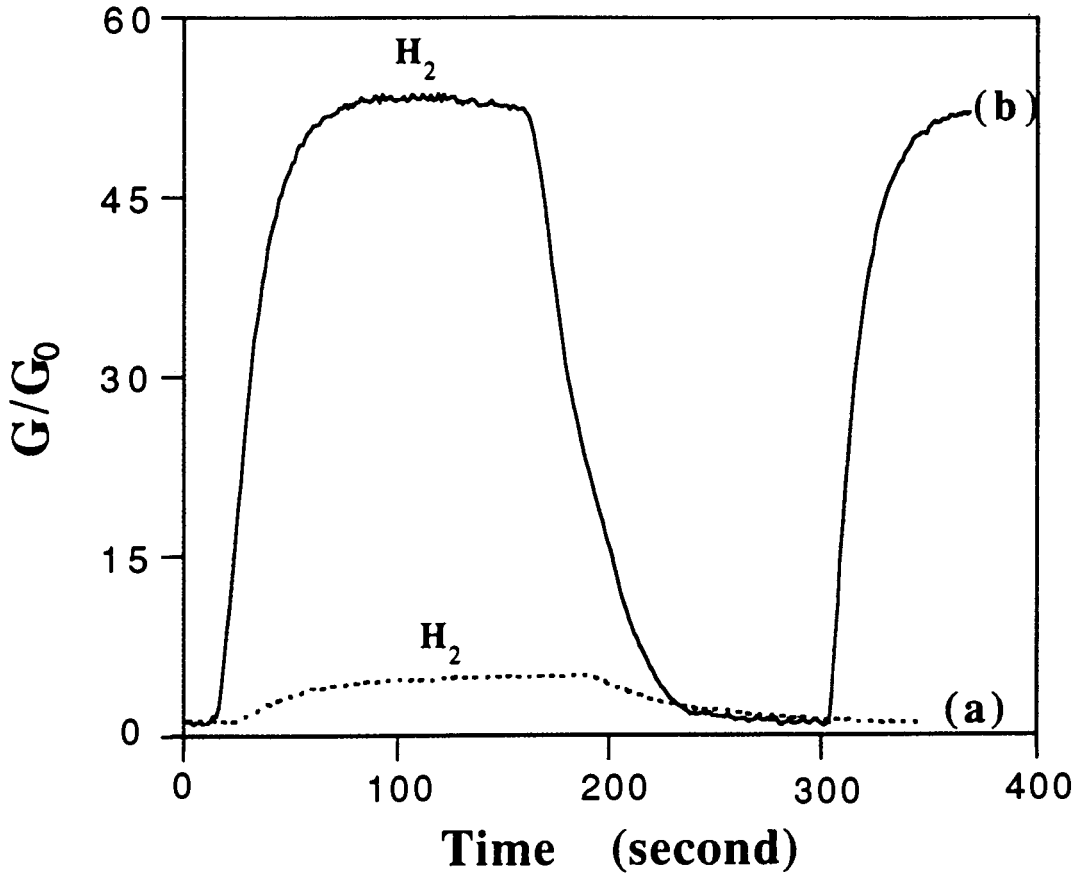

Figure 8.4 Conductance response to 200 ppm H_2 at 275 ^{0}C for (a) pure SnO_2, and (b) Ag added to SnO_2. G_0 is the initial conductance in air.

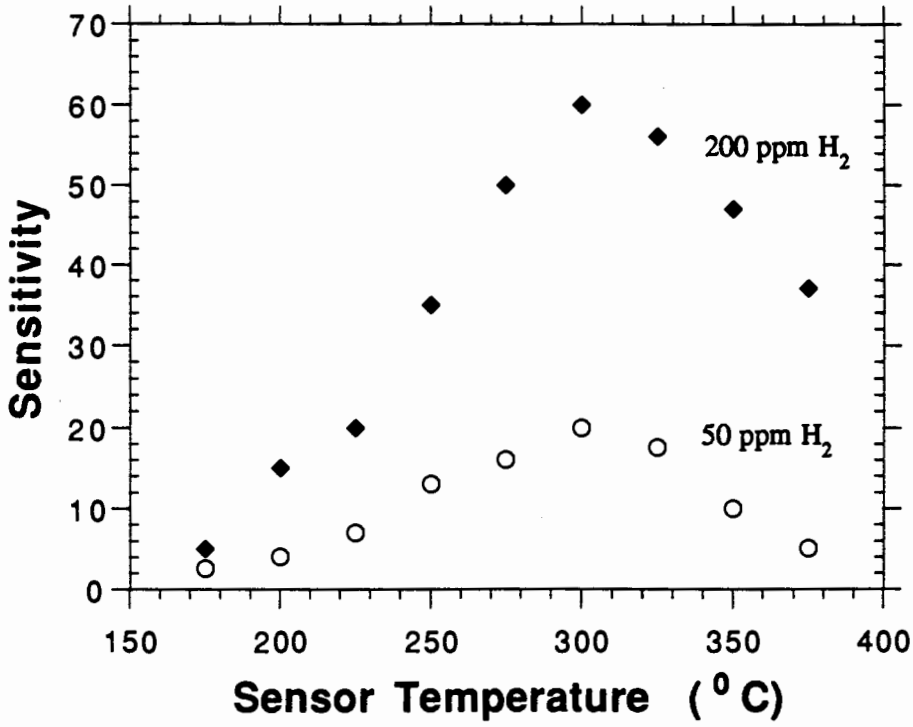

Figure 8.5 Sensitivity response to 200 ppm and 50 ppm H_2 respectively vs. sensor operating temperature.

be reduced by the transformation of O^- to O^{2-} at temperatures above 300 ^{0}C (McAleer *et al* 1987). Also, the silver cluster is not stable above the decomposition temperature of 320 ^{0}C. As a result, best performance of the sensors would be at temperatures around 300 ^{0}C.

The sensitivity influence by Ag clusters was studied. In part I, we reported the observation of fractal Ag clusters on the SnO_2 thin film surface. These fractal clusters produce an insignificant improvement of sensitivity. A method of evaporating a silver layer onto the SnO_2 surface, followed by the heat treatment to disperse the Ag clusters, was used in Ag-added SnO_2 thin film gas sensors. As shown in Fig. 8.4(b), the sensitivity was much improved by the presence of these Ag clusters. However, the level of improvement of the sensitivity depends on the cluster details which in turn were dependent on the thickness of the Ag layer evaporated onto the SnO_2 surface. Figure 8.6 shows the sensitivity to 200 ppm H_2 versus the Ag layer thickness at an operating temperature of 300 ^{0}C. A highest sensitivity is obtained by deposition of the Ag layer with a thickness of about 40 to 60 Å. This highest catalytic activity may be due to a good dispersion of Ag clusters as observed in Fig. 8.1(b). For a thicker Ag layer (> 100 Å), the silvers form large clusters or a semi-continuous layer (see Fig. 8.1(a)) and have little or no catalytic effect, while for a very thin layer an amount of silver is not enough to act as catalyst. The sensing mechanism of these additives will be explained in next section.

The sensitivity as a function of H_2 gas concentration for Ag (50 Å)-SnO_2 sensor is presented in Fig. 8.7. The sensitivity or the conductivity increases

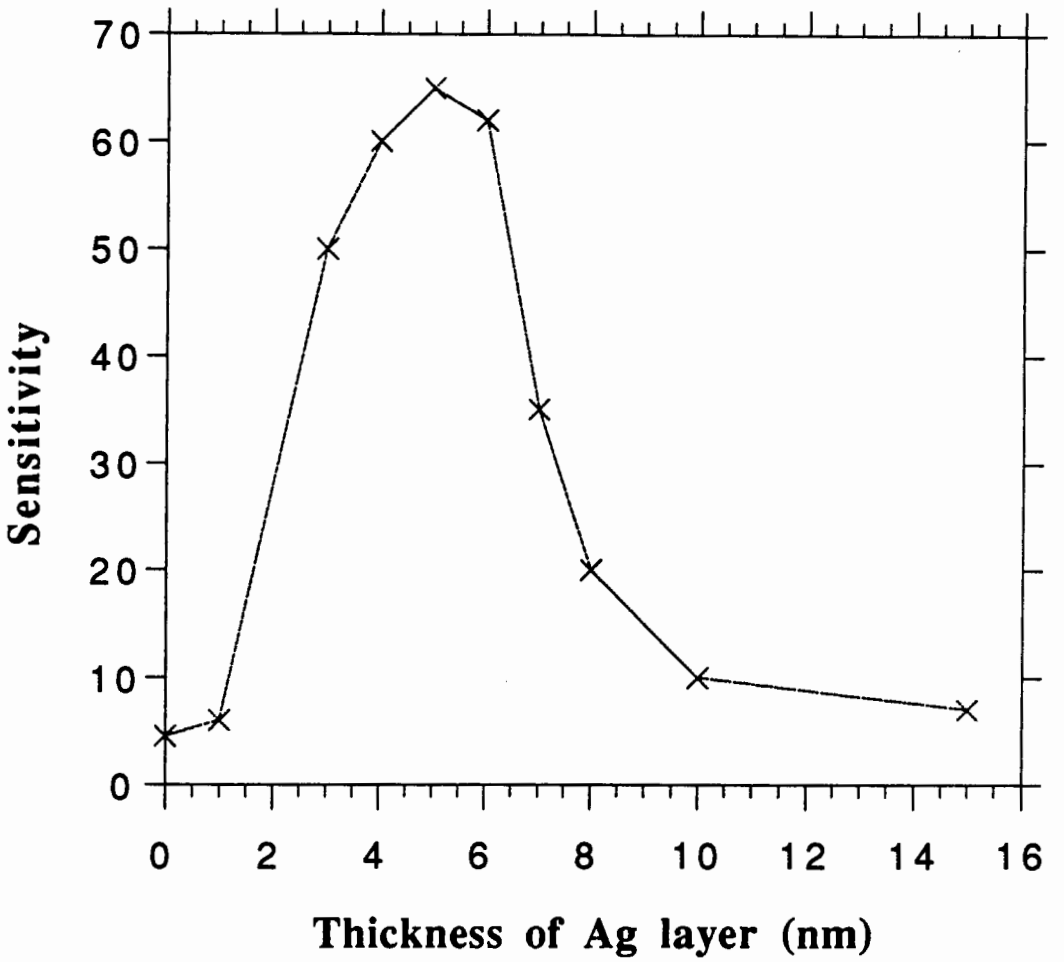

Figure 8.6 Sensitivity to 200 ppm H_2 vs. the Ag layer thickness evaporated onto the SnO_2 surface.

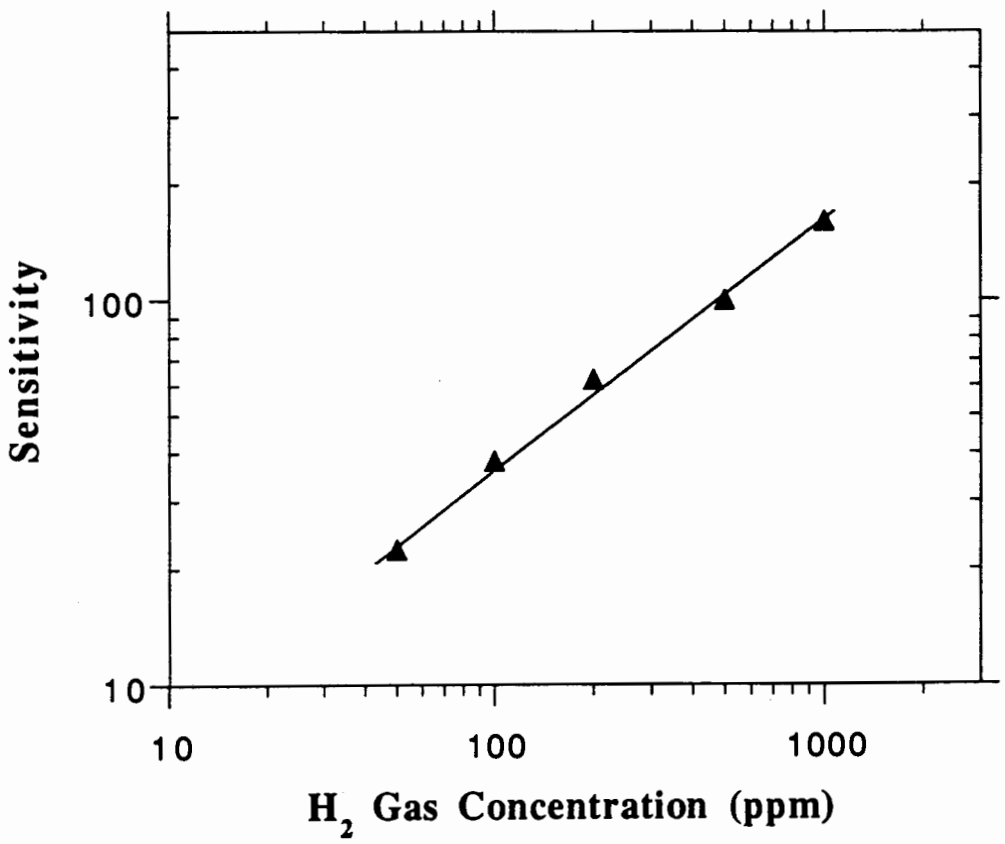

Figure 8.7 Log-log plot of gas sensitivity vs. H_2 concentration for Ag-added (50Å) SnO_2 gas sensors at 300 ^{0}C.

rapidly with increasing concentration of H_2. A log-log plot yields a straight line slope of 0.6, indicating a power law behavior between the sensitivity **S** and gas partial pressure **P:**

$$S \propto P^{\beta} \qquad (8.1)$$

where the exponent β was found to be 0.6 for H_2 in our experiment, which is close to a value of 0.5 for most reducing agents predicted theoretically by assuming that reactivity of O_2^- is negligible and pressure is small (Madou and Morrison 1989). The experimental value of β for H_2 has also been found to be 0.45 to 0.6 for SnO_2-Pd doping (Sberveqlieri 1992). This β value (<1) is dictated by the limitation of the space charged layer such that the sensor conductance tends to saturation for larger pressure of the gas.

8.2.2 Response and recovery

It was already shown that the response time and the recovery time were improved by the addition of Ag onto the SnO_2 surface. These time responses were also quite dependent on the operating temperature and the gas concentration. Figure 8.8 shows the response time and the recovery time to 200 ppm H_2 versus the sensor operating temperature. Both times were smaller for a higher operating temperature. Apparently, at higher temperature the adsorption and desorption of the oxygens are faster. Figure 8.9 shows two electrical conductance response curves for 200 ppm and 1000 ppm H_2 respectively. One can see that the response time and recovery time are longer for a higher gas concentration. This could be explained by a more

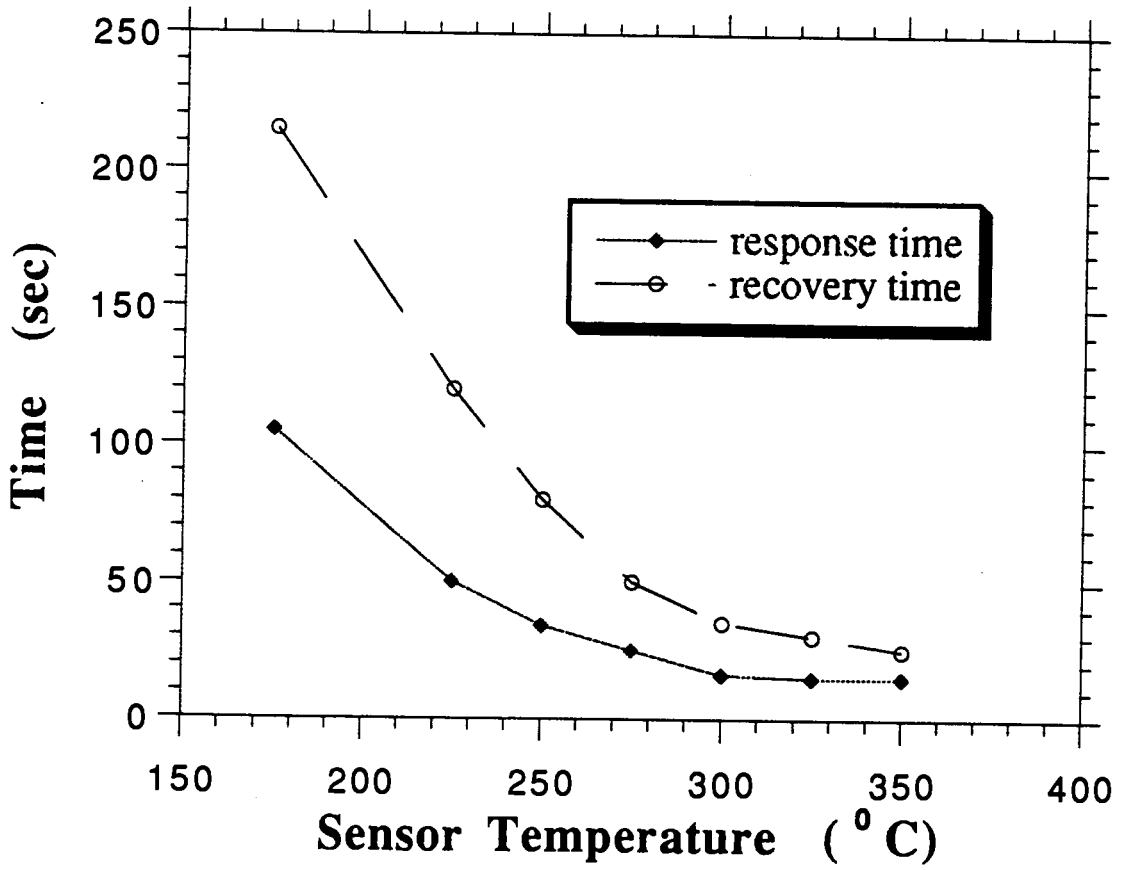

Figure 8.8 Response time and recovery time vs. the sensor operating temperature for Ag-added (50Å) SnO_2 sensor.

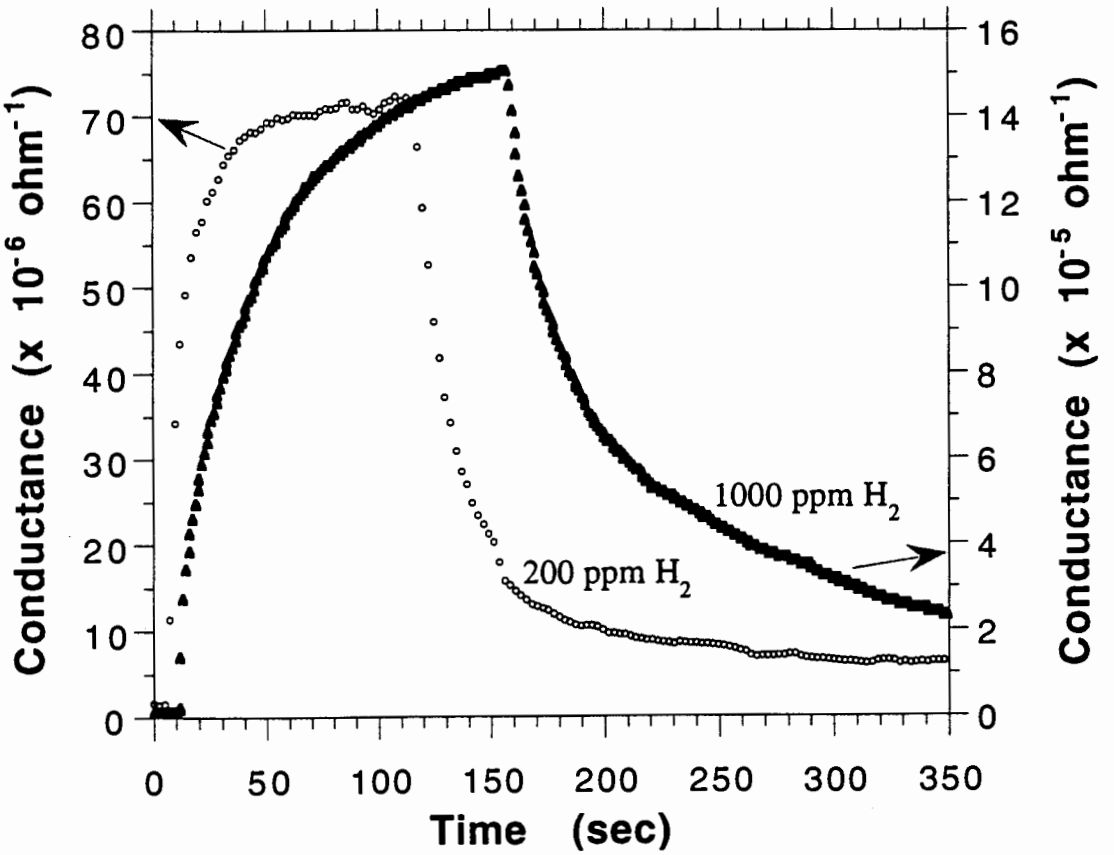

Figure 8.9 Conductance responses to 200 ppm and 1000 ppm H_2 respectively for Ag-added (50Å) SnO_2 sensor at 300 ^{0}C.

hydrogen diffusion into a deeper position from the SnO_2 surface if the H_2 gas partial pressure was high, thus slowing down the response time. For a small H_2 gas concentration, H_2 could be confined more to the free surface of the sensor. Therefore, the responses are fast since there is little or no diffused H_2 in the bulk of SnO_2.

8.2.3 Selectivity and stability

The Ag additives to SnO_2 thin film gas sensors only effectively improved the sensor performance (sensitivity and recovery) to H_2. There is no improvement to other gases such as CO and CH_4. To enhance the selectivity, the use of different metal additives or other methods may be tried. Unfortunately, no further concluding result on this aspect can be presented in this thesis. Stability is another major problem for semiconductor gas sensors from a point of view of commercial use. This investigation is also lacking in our work. Hopefully, this research can be continued in the future.

8.3 Models for surface silver added SnO_2 thin film gas sensors

In this section, we attempt to explain the sensing mechanism of surface silver additives onto SnO_2 thin film gas sensors.

SnO_2 was used as a gas sensor material to detect reducing gases such as H_2 since it is a n-type semiconductor with a wide band gap of 3.8 eV (Robertson 1984). Impurities and oxygen vacancies in SnO_2 usually act as donors to

provide additional electrons to the conduction band that can be trapped into localized surface states. In air, electrons are removed from the SnO_2 semiconductor conduction band, leading to a build-up of O^- species on the surface and a formation of a depletion layer near the surface. Consequently the SnO_2 becomes very resistive. This can be illustrated by the band model in Fig. 8.10(a). The band bending leads to a surface barrier arising at the semiconductor surface.

The addition of surface silver onto SnO_2 can promote the sensitivity. Silver clusters, consisting of Ag and Ag_2O on the surface, form a redox couple Ag^+/Ag^0 (Matsushima *et al* 1988) that acts as a surface acceptor. The Fermi energy of SnO_2 is pinned at the energy level of this redox couple, producing an electron-depleted space-charge region as shown in Fig. 8.10(b). This results in the band bending at the surface of the semiconductor and therefore causes a decrease in the surface conductance of the semiconductor. The shift of the Fermi energy was observed from the X-ray photoelectron spectrum (XPS) measurements by Matsushima and coworkers (1988). They made some observations on binding energy shifts for Pd (3 wt%) and Ag (1.5 wt%) impregnated into sintered SnO_2 powder, and claimed that binding energies of Sn $3d_{5/2}$ and O $1s_{1/2}$ shifted to lower energies by 0.5 to 0.7 eV compared to those of pure SnO_2. These shifts in binding energies are shown to reflect the shift of the Fermi energy of SnO_2.

When surface states of O_2/O^- and Ag^+/Ag^0 are present, the Schottky barrier ϕ_{sb} will be dependent on the barriers of eV_1 and eV_2 as shown in Fig. 8.10 (c). The eV_1 arises from the oxygen adsorbed on the SnO_2 surface and

eV_2 from the oxygen adsorbed on the surface of Ag cluster. However, only the larger of V_1 and V_2 will contribute significantly to ϕ_{sb}

$$\phi_{sb} = e\,\mathrm{Max.}(V_1,V_2) + \mu \qquad (8.2)$$

where μ is the energy difference between the conduction band in the bulk and the Fermi energy. The Schottky barrier must depend on the oxygen adsorption on SnO_2 and Ag cluster surfaces. The latter one is dominant and will control the surface barrier. The higher the concentration of adsorbed oxygen, the lower the Fermi energy, thus the higher the surface barrier.

The depletion layer thickness was estimated to be 1000 to 2000 Å (Madou and Morrison 1989), and the thickness of the SnO_2 thin films in our experiment was about 5000 Å or less, which is an appropriate thickness for high sensitivity as predicted by Eqn. (6.6).

When the sensors were exposed to H_2 , the reaction of H_2 with adsorbed oxygen ions O^- decreases the oxygen acceptor and electrons are restored into the conduction band of the semiconductor. The reaction can be written in a form of:

$$H_2 + O^- \longrightarrow H_2O + e^- \qquad (8.3)$$

As a result of the removal of oxygens, the Fermi level of SnO_2 would shift upward to be pinned at the level of metallic silver Ag^0, resulting in an increase in the surface conductivity. This reduction of Ag^+ to Ag^0 was also

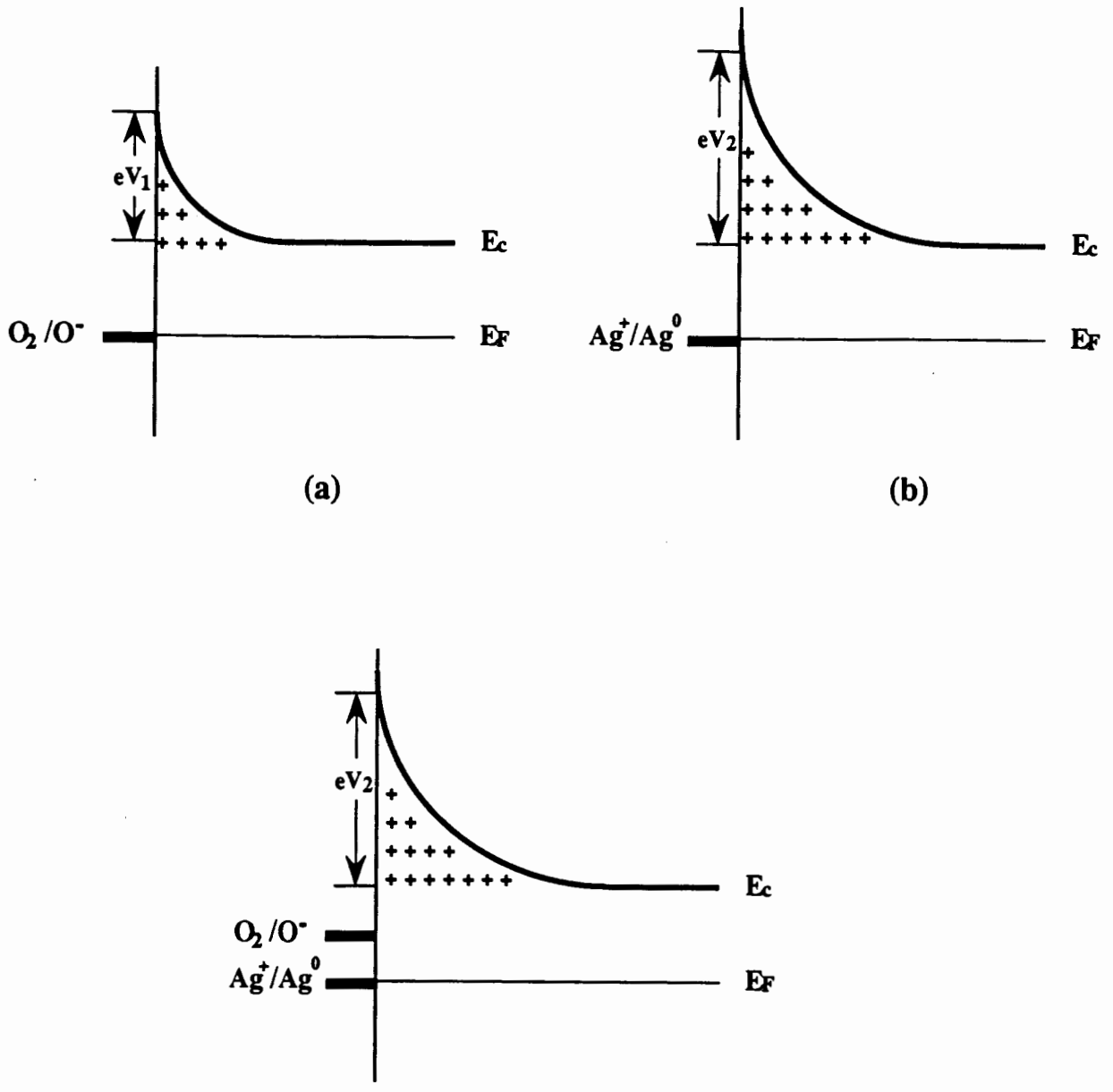

Figure 8.10 Band models showing surface barriers arising from (a) the negatively charged surface oxygen on the SnO_2 surface, (b) the redox couple Ag^+/Ag^0 caused by the adsorbed oxygen on the metal surface and (c) double surface states of O_2/O^- and Ag^+/Ag^0 assuming that the Ag^+/Ag^0 is dominant.

confirmed by XPS (Matsushima *et al* 1988). It was observed that the binding energy of Ag $3d_{5/2}$ was shifted up from 367.4 eV (Ag_2O) to 367.9 eV(Ag), indicating that the surface of Ag is reduced to the metallic state by the H_2 treatment.

On the basis of the discussion of this band model, the effect of surface Ag additives can be interpreted by electronic interaction between metal additives (Ag) and the semiconductor (SnO_2). An exchange between them by electron acceptors and donors from or to the semiconductor upon contact with air or H_2, causes a conductivity decrease or increase in the semiconductor. Silver cluster on the SnO_2 surface acts as catalyst to promote the sensitivity and to speed up the reaction. This can be understood simply by a process where the oxygen absorption on the catalyst removes electrons from the catalyst and the catalyst in turn removes the electrons from the nearby surface region of the semiconductor. The catalyst can also induce H_2 dissociation, thereby speeding up the reaction (Morrison 1987b). The role of additives can be further illustrated by Fig. 8.11. Figure 8.11(a) presents the Auger line scanning of Ag across a silver cluster as found before (refer to Fig. 8.2), from which we can draw a sketch illustrating how the silver metal additives may act as catalyst as shown in Fig. 8.11(b). The oxygens adsorbed on the surface region of the metal remove electrons from Ag. The formation of the redox couple Ag^+/Ag^0, which acts as a surface acceptor as discussed before, consumes the electrons from SnO_2. In the H_2 atmosphere the surface oxygens were removed from the surface and the Ag oxidation state is reduced to the metallic state, leading to electron restoration to the semiconductor.

It is of interest to see the effect of silver cluster size and distribution. This can be represented by three cases as illustrated in Fig. 8.12. In the case (a), there are only a few Ag clusters on the SnO_2 surface, thus only a small portion of semiconductor surface has a depleted region. In the case (c), the Ag clusters are so large and thick that the effect of adsorbates is unlikely to extend beyond a screening length below the surface of a metal and the inter-exchange of electrons between Ag and SnO_2 could not happen in the Ag bulk region. Only in case (b) one has a good dispersion of Ag catalyst such that the depleted regions at the surface of SnO_2 overlap and the influence of the catalyst can extend to the entire surface of the semiconductor. This good dispersion of Ag catalyst can be realized by evaporating a moderate thickness of Ag layer (40 to 60 Å), and the best performance of the sensitivity was achieved as shown in Fig. 8.6.

The role of catalyst in n-type semiconductor powder had been well described by Morrison (1987b). A main advantage of surface metal additives onto SnO_2 thin film gas sensors, over the metal additives to SnO_2 powder by mixing them, is that the additives are only present on the surface, therefore the reaction with gases could be restricted to the exposed surface and the grain boundary effect could be eliminated. Ag clusters dispersion on the SnO_2 surface probably has another application as a Schottky diode when an applied voltage is large enough to overcome the barrier between clusters. This would be another interesting subject not covered in this thesis.

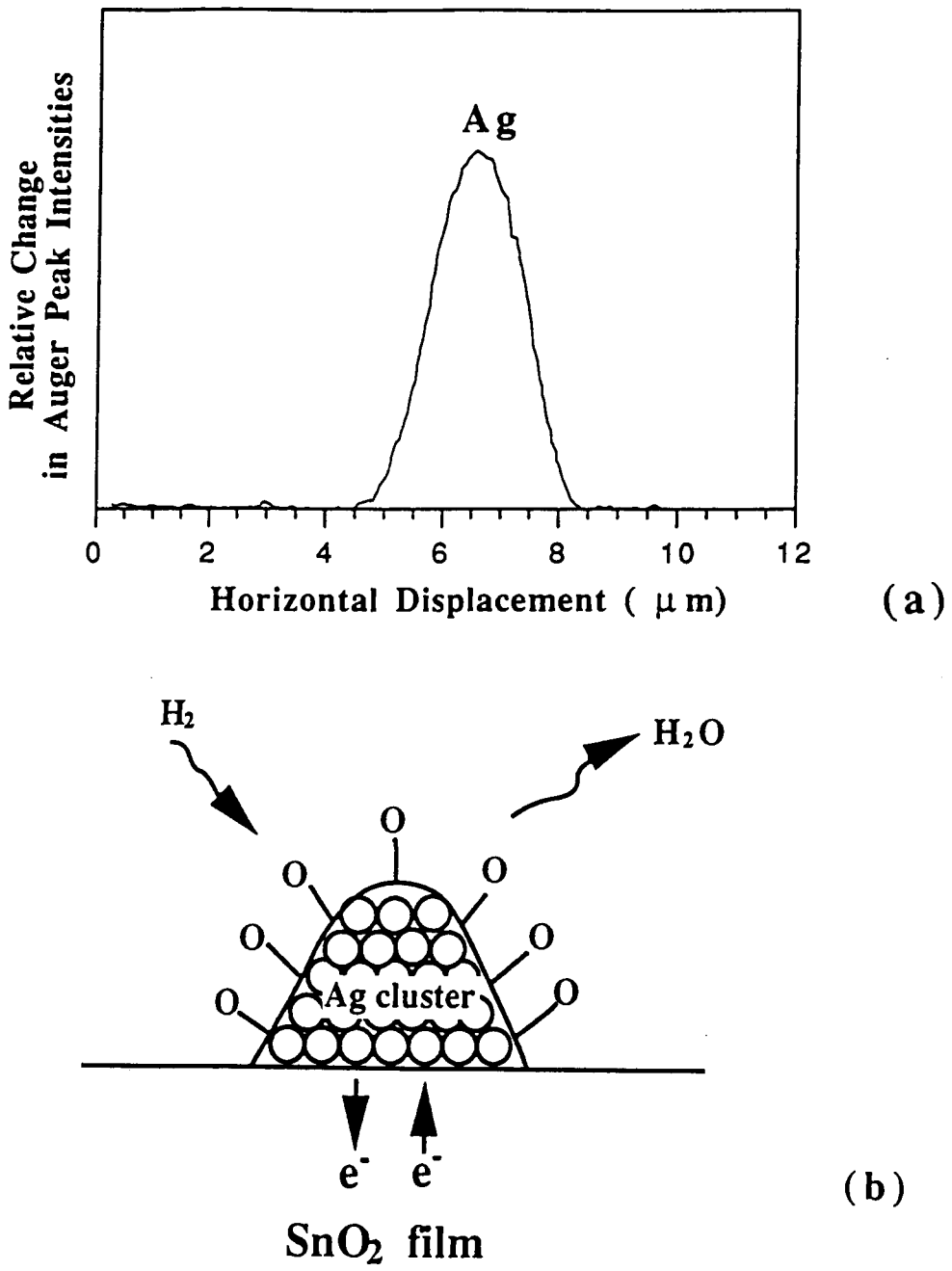

Figure 8.11 (a) Auger line scanning of Ag across a cluster, (b) a sketch illustrating how the Ag cluster acts as catalyst.

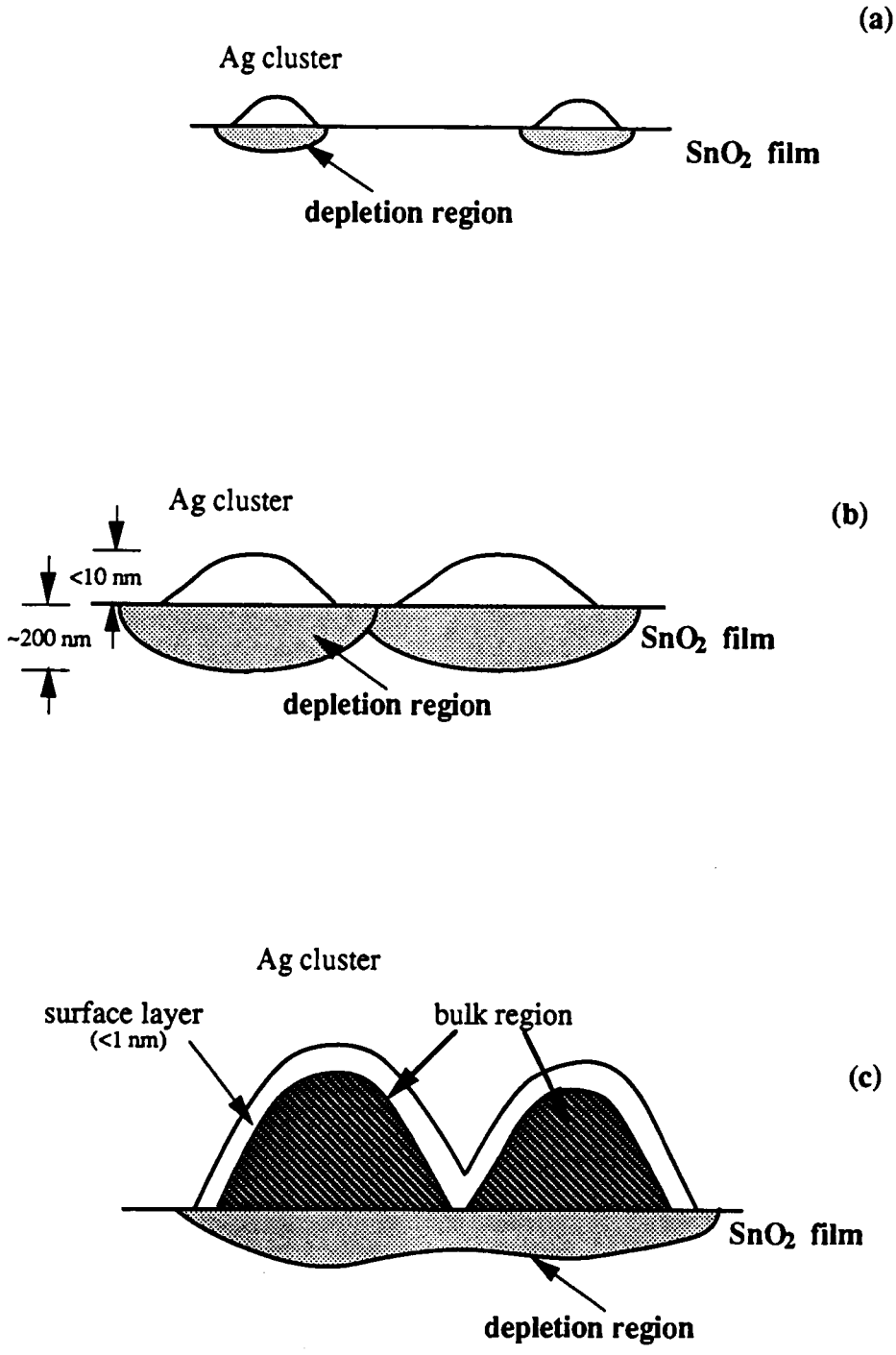

Figure 8.12 Sketches illustrating the effect of cluster size and distribution: (a) and (c) poor Ag catalysts. (b) The catalyst is realized by a good Ag clusters dispersion.

Finally, some additional experimental evidence will be presented to support partly our explanation above. Figure 8.13 shows the conductance versus the operating temperature for Ag-added (50Å) SnO_2 samples in air. One can see that the conductance decreases rapidly with increasing operating temperature up to 300 ^{0}C, indicating an increase in O^- concentration (i.e. more oxygens adsorbed on the surface) at a higher temperature, thereby more electrons extracted from the semiconductors. For oxide semiconductors, the oxygen plays an important role in the change of the surface conductance. To claim this, the sensor performance was examined under N_2 atmosphere. After the sensor element was heated to 300 ^{0}C, the N_2 was injected at a flow rate of 10 L/min.. Figure 8.14(a) shows the conductance response to 500 ppm H_2 in the mixture of H_2 with N_2 after introducing H_2. One can see that the conductance increase (i. e. sensitivity) is higher than that in the mixture of the H_2 with air as shown in Figure 8.14(b). This indicates that there would be still some oxygen adsorptions at the surface in the mixture of H_2 with air, while the oxygen absorption is absent in the mixture of H_2 with N_2. After H_2 flow was turned off, the conductance remained almost unchanged in the N_2 atmosphere. However, the conductance reduced rapidly as the N_2 flow was switched to air. It becomes clear that the change of conductance (decrease or increase) is caused by the adsorption and desorption of oxygen on the sensor surface. The conductance change depending on the oxygen partial pressure could be used as an oxygen sensor.

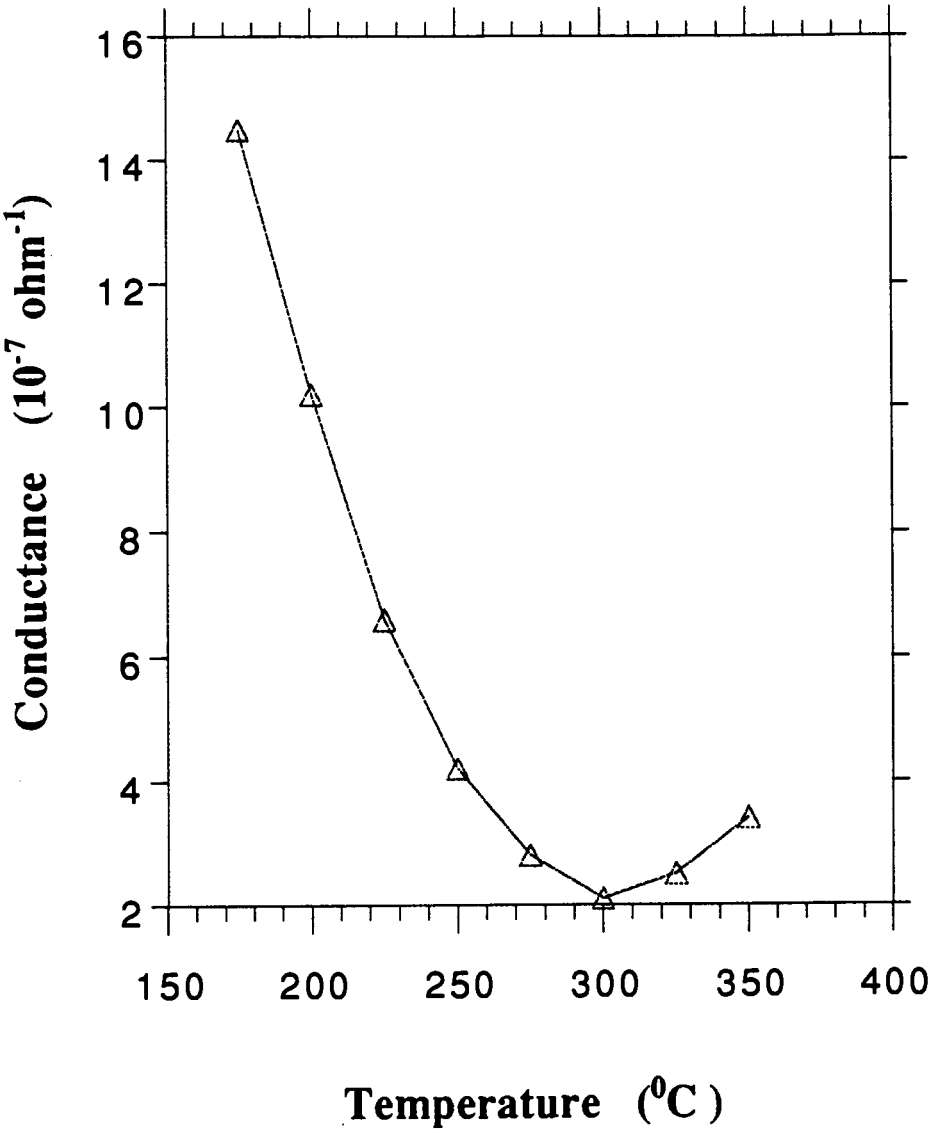

Figure 8.13 Conductance vs. the operating temperature for Ag-added (50Å) SnO_2 sample.

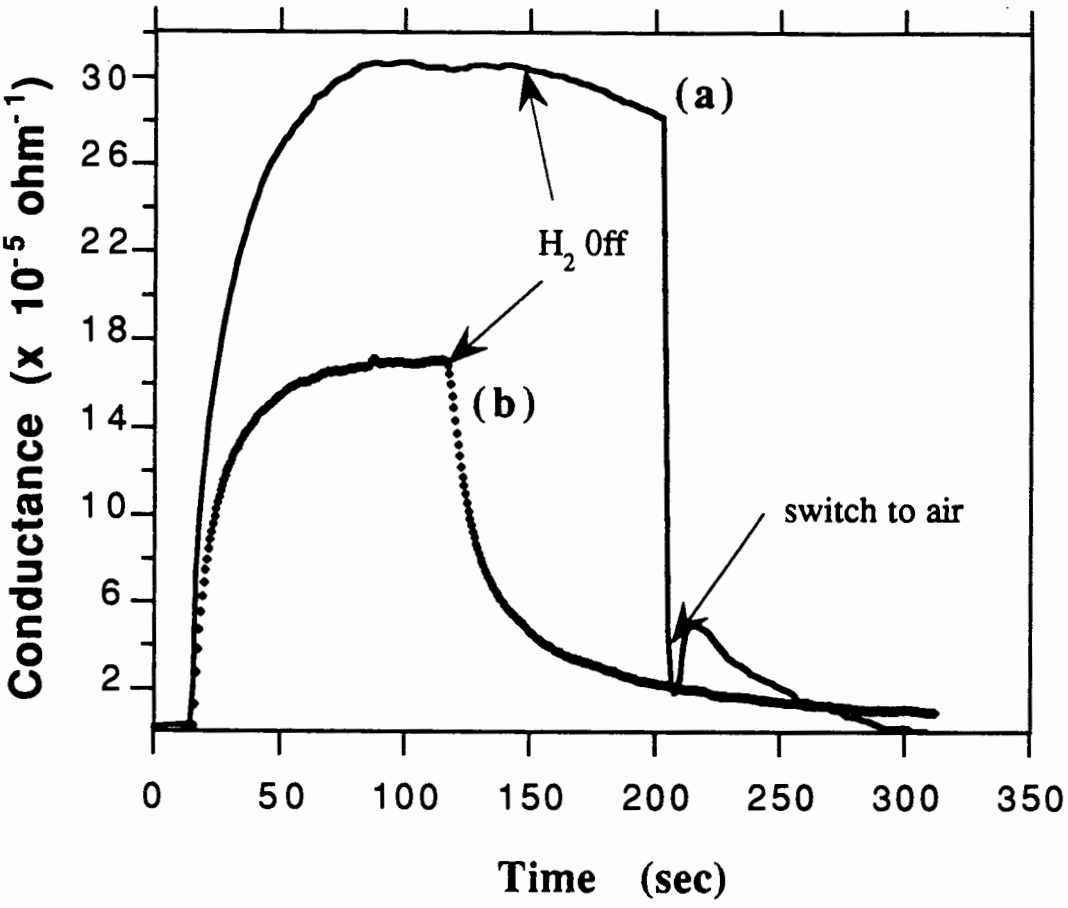

Figure 8.14 Conductance response to 500 ppm H_2 in (a) the mixture of H_2 with N_2, and (b) the mixture of H_2 with air.

Conclusion to Part II

The silver clusters acting as catalytic activators in SnO_2 gas sensors were investigated.

1. It was found that surface silver additives on SnO_2 thin film effectively improved the sensor performance to H_2. The sensitivity was increased by at least a factor of 10 and the sensor recovery time decreased after the surface silver addition onto the SnO_2 surface.

2. The sensitivity was found to be dependent on the operating temperature of the sensors and the amount of Ag additives that influences the cluster details. The experimental results showed that the best performance of sensors could be achieved by evaporating a Ag layer of 40 to 60 Å, and operating at temperatures around 300 ^{0}C.

3. The effect of electric interaction between metal additives (Ag) and semiconductor (SnO_2) was studied and models for the promotion role of these additives are suggested.

There is a potential of commercial use for our Ag-SnO_2 thin film gas sensors, which have high sensitivity, short response time and good selectivity to hydrogen. However, there are some problems, for example stability, reversibility and technical problems for large-scale manufacturing, that need to be investigated from a point of view of commercial use.

Bibliography

Advani, G. N. and Jordan, A. G. J. *Electron. Mater.* **9**, 29(1980).

Advani, G. N., Komem, Y., Hasenkopf, J. and Jordan, A. G. *Sensors and Actuators* **2**, 139(1981/82).

American Institute of Physics Handbook 2nd Edition (Mcgraw-Hill, New York, 1963)

Amitrano, C., Coniglio, A. and Liberto, F. di *Phys. Rev. Lett.* **57**, 1016(1986).

Argoul, F., Arneodo, A., Grasseau, G. and Swinney, H. L. *Phys. Rev. Lett.* **61**, 2558(1988).

Azad, A. M., Akbar, S. A., Mhasalkar, S. G., Birkefeld, L. D. and Goto, K. S. *J. Electrochem. Soc.* **139**, 3690(1992).

Ball, R. C. in *On Growth and Form: Fractal and Non-Fractal Patterns in Physics* edited by H. E. Stanley and N. Ostrowsky (Martinus Nijhoff, Dordrecht, 1986).

Ball, R. C., Brady, R. M., Rossi, G. and Thompson, B. R. *Phys. Rev. Lett.* **55**, 1406(1983).

Bensimon, D., Domany, E. and Aharony, A. *Phys. Rev. Lett.* **51**, 1394(1983).

Bergveil, P. *IEEE Trans. Biomed. Eng.* **BME-17(1)**, 70(1970).

Cafiero, R., Pietronero, L. and Vespignani, A. *Phys. Rev. Lett.* **70**, 3939(1993).

Cates, M. E. and Witten, T. A. *Phys. Rev. Lett.* **56**, 2497(1986).

Cheong, H. W., Choi, J. J., Kim, H. P., Kim, J. M., Kim, J. M. and Churn, G. S. *Sensors and Actuators B* **9**, 227(1992).

Chon, H. and Pajares, J. *J. Catal* **14**, 3257(1969).

Daccord, G., Nittmann, J., and Stanley, H. E. in *On Growth and Form: Fractal and Non-Fractal Patterns in Physics* edited by H. E. Stanley and N. Ostrowsky

(Martinus Nijhoff, Dordrecht, 1986a).

Daccord, G., Nittmann, J., and Stanley, H. E. *Phys. Rev. Lett.* **56**, 336(1986b).

Daniel, C. and Wood, F. S. *Fitting Equation to Data* (John Wiley & Sons, New York, 1980).

Das, D. and Banerjee, R. *Thin Solid Films* **147**, 321(1987).

Deutsher, G., Zallen, R. and Adler, J. *Pecolation, Structure and Processes*, **Vol. 5**. (Ann. of the Israel Physical Society, 1983).

Ding, J. R. and Liu, B. X. *J. Phys. A* **22**, L265 (1989a).

Ding, J. R. and Liu, B. X. *J. Mater. Res.*, **4**, 1296(1989b).

Eden, M. in *Proceedings of the Fourth Berkeley Symposium on Mathematical Statistics and Probability*, edited by F. Neyman (Univ. of California Press, Berkeley, 1961). Vol. IV, p. 233.

Elam, W. T., Wolf, S. A., Sprague, J., Gubser, D. U., Vechten, D. Van, Barz, Jr. G. L. and Meakin, P. *Phy. Rev. Lett.* **54**, 701(1985).

Fleury, V. *J. Mater. Res.* **6**, 1169(1991).

Fresart, E. D., Darville, J. and Gilles, J. M. *Surface science* **126,** 518(1983).

Halsey, T. C., Meakin, P. and Procaccia, I. *Phys. Rev. Lett.* **56**, 854(1986a).

Halsey, T. C., Jensen, M. H., Kadanoff, L. P., Procaccia, I. and Shraiman, B. I. *Phys. Rev. A* **33,** 1141(1986b).

Harkoma-Mattila, A., Rantala, T. S., Lantto, V. and Leppävuori, S. *Sensors and Actuators B* **6,** 248(1992).

Hidaka, Y., Suzuki, M., Murakami, T. and Inamura, T. *Thin Solid Films* **106,** 311(1983).

Huang, L. J., Ding, J. R. and Li, H. D. *J. Appl. Phys.* **63**, 1879(1988).

Gautheron, B., Labeau, M., Delabouglise, G. and Schmatz, U. *Sensors and Actuators*

B, **15-16**, 357(1993).

Geloven, P. V., Moons, J., Honore, M. and Roggen, J. *Sensors and Actuators* , **17**, 361(1989).

Grier, D. G., Kessler, D. A. and Sander, L. M. *Phys. Rev. Lett.* **59**, 2315(1987).

Islam, M. N. and Hakim, M. O. *J. Phys. Chem. Solid* **46**, 339(1985).

Janata, T. and Huber, R. J. *Solid State Chemical Sensors*, (Academic Press, Orlando, 1985).

Jullien, R. *J. Phys. A* **17**, L771(1984).

Jullien, R. and Botet, R. *Aggregation and Fractal Aggregates*, (World Scientific Publishing Co Pte Ltd., Singapore, 1987).

Kirner, U., Schierbaum, K. D. and Göpel, W. *Sensors and Actuators B* **1**, 103(1993).

Kohl, D. *Sensors and Actuators* **18**, 71(1989).

Kohl, D. *Sensors and Actuators B*, **1**, 158(1990).

Kolb, M., Botet, R. and Jullien, R. *Phys. Rev. Lett.* **51**, 1123(1983).

Langer, L. S. *Rev. Mod. Phys.* **52**, 1(1980).

Lantto, V. and Mizsei, J. *Sensors and Actuators B*, **5**, 21(1991).

Löw, H., Sulz, G., Lacher, M., Kühner, G., Uptmoor, G., Reiter, H. and Steiner, K. *Sensors and Actuators B*, **9**, 215(1992).

Madou, M. J. and Morrison, R. S. *Chemical Sensing with Solid State Devices* (Academic Press, Inc., San Diego, 1989).

Mandelbrot, B. B., and Evertsz, C. J. G. *Nature* **348**, 143(1990).

Martinelli, G. and Carotta, M. C. *Sensors and Actuators B*, **15-16**, 363(1993).

Matsushita, M., Sano, M., Hayakawa, Y., Honjo, H. and Sawada, Y. *Phys. Rev. Lett.* **53**, 286(1984).

Matsushita, M., Hayakawa, Y. and Sawada, Y. *Phys. Rev. A* **32**, 3814(1985).

Matsushima, S., Teraoka, Y., Miura, N. and Yamazoe, N. *Japanese Journal of Appl. Phys.* **27**, 1798(1988).

Matsuura, Y. and Takahata, K. *Sensors and Actuators B* **5**, 205(1991).

McAleer, J. F., Moseley, P. T., Norris, J. O. W., Williams, D. E. and Tofield, B. C. *J. Chem. Soc., Faraday Trans. I*, **83**, 1323(1987).

McAleer, J. F., Moseley, P. T., Norris, J. O. W., Williams, D. E. and Tofield, B. C. *J. Chem. Soc., Faraday Trans. I*, **84**, 441(1988).

Meakin, P. *Phys. Rev. Lett.* **51**, 1119(1983a).

Meakin, P. *Phys. Rev. A* **27**, 1495(1983b).

Meakin, P. and Wasserman, Z. *Physics Letters* **103A**, 337(1984).

Meakin, P. and Sander, L. M. *Phys. Rev. Lett.* **54**, 2053(1985).

Meakin, P. and Vicsek, T. *Phys. Rev. A* **32**, 685(1985).

Meakin, P. *Phys. Rev. A* **33**, 3371(1986a).

Meakin, P. *Phys. Rev. A* **33**, 4199(1986b).

Meakin, P. and Family, F. *Phys. Rev. A* **34**, 2558(1986).

Mirkin, L. I. *Handbook of X-ray Analysis of Polycrystalline Materials*, (Consultants Bureau, New York, 1964).

Morrison, S. R. *Sensors and Actuators* **2**, 329(1982).

Morrison, S. R. *Sensors and Actuators* **11**, 283(1987a).

Morrison, S. R. *Sensors and Actuators* **12**, 425(1987b).

Niemeyer, L., Pietronero, L. and Wiesmann, H. J. *Phys. Rev. Lett.* **52**, 1033(1984).

Nittmann, J., Daccord, G., and Stanley, H. E. *Nature* **314**, 141(1984).

Nuffield, E. W. *X-ray Diffraction Methods* (John Wiley and Sons, New York, 1966)

Ohnishi, H., Sasaki, H., Matsumoto, T. and Ippommatsu, M. *Sensors and Actuators B*

13-14, 677(1993).

Oyabu, T., Osawa, T. and Kurobe, T. *J. Appl. Phys* **53**, 7125(1982).

Plischke, M. and Rácz, Z. *Phys. Rev. Lett.* **53**, 415(1984).

Radnoczi, GY., Vicsék, T., Sander, L. M. and Grier, D. *Phys. Rev. A* **35**, 4012(1987).

Rácz, Z. and Plischke, M. *Phys. Rev. A* **31,** 985(1985).

Rácz, Z. and Vicsek, T. *Phys. Rev. Lett.* **51**, 2382(1983).

Robertson, J. *Phys. Rev. B* **30,** 3520(1984).

Sawada, Y., Dougherty, A. and Gollub, J. P. *Phys. Rev. Lett.* **56**, 1260(1986).

Sberveglieri, G., Groppelli, S. and Nelli, P. *Sensors and Actuators B* **4,** 457(1991).

Sberveglieri, G. *Sensors and Actuators B* **6,** 239(1992).

Sberveglieri, G., Nelli, P., Benussi, G. P., Depero, L. E., Zocchi, M., Rossetto, G. and Zanell, P. *Sensors and Actuators B* **15-16,** 334(1993a).

Sberveglieri, G., Faglia, G, Groppelli, S., Nelli, P., and Perego, C. *Sensors and Actuators B* **13-14,** 117(1993b).

Sears, W. and Colbow, K. *Appl. Phys. Lett.* **55**, 2165(1989).

Sempere, R., Bourret, D., Woignier, T., Phalippou, J. and Jullien, R. *Phys. Rev. Lett.* **71**, 3307(1993).

Sulz, G., Kühner, G., Reither, H., Uptmoor, G., Schweizer, W., Löw, H., Lacher, M. and Steiner, K. *Sensors and Actuators B* **15-16,** 390(1993).

Taguchi, N. *Gas Detecting Device*, **U.S. patent 3**, 631, 436 (1971).

Takayama, H. and Fujitsu, S. *Solid State Ionics* **35**, 411(1989).

Tamaki, J., Maekawa, T., Miura, N. and Yamazoe, N. *Sensors and Actuators B* **9,** 197(1992).

Tokuyama, M. and Kawasaki, K. *Physics Letters* **100A**, 337(1984).

Vold, M. *J. Colloid Science* **18**, 684(1963).

Vicsek, T. *Fractal Growth Phenomena* (world Scientific, Singapore, 1989).

Witten, T. A., and Sander, L. M. *Phys. Rev. Lett.* **47**, 1400(1981).

Witten, T. A., and Sander, L. M. *Phys. Rev. B.* **27**, 5686(1983).

Witten, T. A., and Meakin, P. *Phys. Rev. B.* **28**, 5632(1983).

Witten, T. A. in *On Growth and Form: Fractal and Non-Fractal Patterns in Physics* edited by H. E. Stanley and N. Ostrowsky (Martinus Nijhoff, Dordrecht, 1986).

Xu, C., Tamaki, J., Miura, N. and Yamazoe, N. *Sensors and Actuators B* **3**, 147(1991).

Yamozoe, N., Fuchigama, J., Kishkawa, M. and Seiyama, T. *Surface Sci.* **86,** 335(1979).

Yamazoe, N., Kurokawa, Y. and Seiyama, T. *Sensors and Actuators,* **4**, 283(1983).

Zhang, J., Wessel, S. A. and Colbow, K. *Thin Solid Films* **185**, 263(1990).

Zhang, J. and Colbow, K. *Appl. Phys. Lett.* **58**, 1013(1991).

Zhang, J. and Colbow, K. *J. Appl. Phys.* **71**, 2238(1992).

Zhang, J., Heinrich, B. and Colbow, K. *Surface Science* **286**, 327(1993a).

Zhang, J., Liu, D. and Colbow, K. *Physical Review B* **48**, 9130(1993b).

Zhang, J., Miremadi, B. K. and Colbow, K. *Journal of Materials Science Letters* **13**, 1048(1994).

Zhou, G., Wessel, S. A. and Colbow, K. *Phys. D: Appl. Phys.* **21**, 1802(1988).